



**PERFORMANCE AND EMISSION CHARACTERISTICS OF AN  
AUTOMOTIVE DIESEL ENGINE USING BIODIESEL FUEL  
WITH THE INFLUENCE OF AIR INTAKE VARIABLES**

**by**

**RIZALMAN MAMAT**

**A thesis submitted to  
The University of Birmingham  
for the degree of  
DOCTOR OF PHILOSOPHY**

**School of Mechanical Engineering  
The University of Birmingham  
November 2009**

UNIVERSITY OF  
BIRMINGHAM

**University of Birmingham Research Archive**

**e-theses repository**

This unpublished thesis/dissertation is copyright of the author and/or third parties. The intellectual property rights of the author or third parties in respect of this work are as defined by The Copyright Designs and Patents Act 1988 or as modified by any successor legislation.

Any use made of information contained in this thesis/dissertation must be in accordance with that legislation and must be properly acknowledged. Further distribution or reproduction in any format is prohibited without the permission of the copyright holder.

## **ABSTRACT**

The air induction system plays a major role by providing necessary air charge for combustion to take place in an engine cylinder. The pressure drop across the air intake manifold is known to have a significant effect on the indicated power of the internal combustion engine. Most car manufacturers locate the air grill at the front of a vehicle to enhance the volumetric efficiency. However due to wading performance, for a sport utility vehicle like a Land Rover Freelander the air grill is located at the side of the front tyre. The air speed at the grill side is high and creates negative pressure, thus reducing the volumetric efficiency. Therefore, a thorough study of the design of the air induction system (AIS) with negative pressure at the air grill is vital, in order to fully understand the flow behavior in this AIS. Moreover, when the engine is equipped with turbocharger, the performance of the air intake system is also affected by the exhaust parameter which depends on the combustions of fuel in the engine cylinder. The properties of biodiesel are slightly different in density, viscosity and cetane number. These parameters are potentially affecting the combustion in engine cylinder. Thus, the investigation of the effect of fuel on the air intake system is vital for the study of the diesel engine operating with biodiesel. The analysis of the combustion of biodiesel in a V6 diesel engine includes the ignition delay, rate of heat release, in-cylinder peak pressure as well as the exhaust emissions.

The study consists of 3 parts; (1) three-dimensional CFD analysis on the performance of the Land Rover Freelander AIS, (2) one-dimensional analysis of a V6 diesel engine with the effect of the AIS, (3) experimental study of a V6 diesel engine operating with RME and ULSD; The three-dimensional analyses on the performance

of a Freelander AIS have been conducted to study the effect of negative pressure on pressure-drop in the intake manifold. The results show that the magnitude of negative pressure gives significant effect not just to pressure drop but also to the flow behavior in the intake manifold. The steady flow tests on the actual intake manifold of a Freelander model have been conducted to validate the simulation outcome. The results show good agreement between experiment and simulation.

In order to improve understanding on the flow wave action on the intake manifold of a V6 diesel engine, one-dimensional engine simulations have been conducted using commercial Ricardo WAVE v7.2 software. The result shows good agreement between simulation and experiment. The simulation result shows a significant affect on the wave action as pressure drop increases from zero to 20% in the intake manifold.

The research continued further to investigate the effect of air induction parameters in the V6 diesel engine such as pressure drop and flow temperature on the performance and emissions of the engine. The effect of intake flow parameter to the engine when operated with RME has been studied and the comparisons have been made when ULSD is used as base fuel. The experimental results show that in general, the engine operating with RME produces lower power and higher bsfc due to low energy content of RME as compared to ULSD. The emissions of NO<sub>x</sub> are slightly higher, but lower CO and HC are produced. The pressure drop along the AIS has significantly affected the performance as well as emissions of the engine. The performance of the diesel engine drops significantly as the pressure drop increases and exhaust emissions increase considerably.

## ACKNOWLEDGEMENTS

I would like to express my gratitude and sincere thanks to my supervisor Professor Hongming Xu for his guidance, support and encouragement throughout my study. I also would like to thank my associate supervisor Professor Miroslaw Lech Wyszynski for his passions toward the remarkable end of my study.

I would also like to thank my sponsors:

- The Malaysia Government for the provision of my Ph.D. scholarship
- Jaguar Land Rover (JLR) for financial and technical support towards the research project,
  - Dr J. Qiao and Dr Steven Pierson (Jaguar Cars Limited) for their technical assistance
  - Dr Adrian Gaylard (Land Rover Gaydon) for the provision of the 3D geometry of the Land Rover air intake system
- Shell Global Solutions UK through Dr R. F. Cracknell for the supply of ULSD and RME test fuels;

I gratefully acknowledge Dr. Athanasios Tsolakis for his helpful discussion during this project. I would like to acknowledge Dr Mingshan Wei and Dr Xin Shi for long discussion and advice on developing the one-dimensional model. A special thank you goes to my colleagues Dr S. Chuepeng, Dr. A. F. Mahrous, Dr. K. Theinnoi, Mr Nik Rosli Abdullah, and friends in FPS group for their fruitful discussions, friendship and help.

Rizalman Mamat

November 2009

*I wish to dedicate this thesis...*

*To my parents*

*To my beloved wife and lovely kids: Nur Dania, Nur Najah and Haziq*

*To my brothers and sisters,*

*And friends*

# TABLE OF CONTENTS

## CHAPTER 1 INTRODUCTION

1.1	Background	24
1.1.1	Diesel Engine Technology	25
1.1.2	Alternative Fuels for Diesel Engines	28
1.1.3	Combustion in Diesel Engines	29
1.2	Objectives and Approaches	31
1.3	Thesis Outline	33

## CHAPTER 2 LITERATURE REVIEW

2.1	Air Intake System for Diesel Engines in a Vehicle	34
2.1.1	System Component and Development	37
2.1.2	Optimisation of AIS by Computational Fluid Dynamics	42
2.1.3	One-Dimensional Modelling of an Air Intake System	46
2.2	Biodiesel as an Alternative Fuel	
2.2.1	Biodiesel Production, Policies and Standardisation	47
2.2.2	Performance and Emissions of Biodiesel as Fuel in ICE	50
2.3	Exhaust Emissions from the Combustion of Biodiesel	
2.3.1	Oxides of Nitrogen	53
2.3.2	Carbon Monoxide	55
2.3.3	Unburned Hydrocarbons	56
2.3.4	Particulate Matter	57
2.4	Summary	58

## **CHAPTER 3 RESEARCH METHODOLOGY**

3.1	Setup of CFD Models	59
3.1.1	Governing Equations	60
3.1.2	Turbulence Model	64
3.1.3	Modelling Approach	67
3.1.4	Grid Generation	68
3.2	Experimental System and Techniques	
3.2.1	Steady Flow Test	72
3.2.1.1	Purpose of Steady Flow Testing	72
3.2.1.2	Design and Setup of Steady Flow Test Bench	73
3.2.2	The engine Performance Characteristic	80
3.2.3	Diesel Engine Test Setup	
3.2.3.1	Engine Test Bench	83
3.2.3.2	Engine Fuel System	87
3.2.3.3	Engine Cooling System	88
3.2.3.4	Exhaust Emissions Measurement	90
3.2.3.5	Data Acquisition System	91
3.3	Summary	96

## **CHAPTER 4 CFD MODELLING OF AIR INTAKE SYSTEM AND VALIDATION**

4.1	Introduction	97
4.2	Problem Definitions	97
4.3	Boundary Conditions	100
4.4	Result & Discussions	102
4.4.1	Simulation under Static Entry Flow	103
4.4.2	Tangential Velocity Magnitude	107
4.4.3	Grid Sensitivity Test	110
4.5	Summary	111

## **CHAPTER 5 ONE DIMENSIONAL MODELLING OF A V6 DIESEL ENGINE AND VALIDATION**

5.1	Introduction	112
5.2	Engine Model Setup	112
5.2.1	General Parameter of Diesel Engine	114
5.2.2	Heat Transfer and Combustion Model	116
5.2.3	Engine Valves, Injection Timing and Turbocharger Set-up	122
5.3	Simulation Results and Data Validation	
5.3.1	Simulation Result and Validation at Full Load Curve	124
5.3.2	Simulation Results with Variable Boost Pressure	128
5.4	Summary	135

**CHAPTER 6 ENGINE PERFORMANCE AND EMISSIONS WITH  
BIODIESEL**

6.1	Introduction	136
6.2	Engine Test Conditions	137
6.3	Engine Testing at Low Load and Part Load	138
6.4	Diesel Engine Operating with RME and ULSD	144
6.5	Effect of Fuel Temperatures	148
6.6	Effect of Multiple Injection	158
6.7	Summary	168

**CHAPTER 7 EFFECT OF AIR INTAKE VARIABLES TO THE ENGINES  
PERFORMANCE AND EMISSIONS**

7.1	Effect of Boost Pressure Drop	170
7.1.1	Engine Performance	173
7.1.2	Exhaust Gas Emissions	178
7.2	Effect of Charge Air Temperature	181
7.2.1	Engine performance	187
7.2.2	Exhaust Gas Emission	189
7.3	Summary	191

<b>CHAPTER 8</b>	<b>CONCLUSION AND RECOMMENDATIONS</b>	
8.1	Conclusion Remarks	194
8.1.1	Influence of Negative Pressure on Induction Grill	194
8.1.2	One-Dimensional Analysis of Air Induction System	194
8.1.3	Engine Performance and Emissions of a Diesel Engine Operating with ULSD and RME	195
8.1.4	The Effect of Intake Charge Pressure Drop and Temperature on Engine Performance	196
8.2	Recommendation for Future Work	198
8.2.1	The Modifications of Current Design of a Freelander Air Intake System	198
8.2.2	The Effect of EGR Rate and Exhaust Gas Temperature to the Intake Charge	198
8.2.3	Transient Operation on Diesel Engine Operating with ULSD and RME	199
	<b>REFERENCE</b>	200
	<b>APPENDIX</b>	215

## LIST OF ABBREVIATIONS

AIS	Air induction system
BMEP	Brake mean effective pressure [Bar]
bsfc	Brake specific fuel consumption [kg/kWh]
BSN	Bosch smoke number [BSN]
BV	Butterfly valve
CAD	Crank angle degree [degree]
CFD	Computational fluid dynamics
CO	Carbon monoxide
CO <sub>2</sub>	Carbon dioxide
COV	Coefficient of variation
COV <sub>IMEP</sub>	Coefficient of variation in IMEP
COV <sub>Pmax</sub>	Coefficient of variation in peak cylinder pressure
DI	Direct injection
EGR	Exhaust gas recirculation
EMS	Engine management system
EPSP	Exhaust port static pressure [Pa]
EU	European Union
FAME	Fatty acid methyl ester
GUI	Graphic user interface
HC	Hydrocarbon
HCCI	Homogeneous charge compression ignition
HCLD	Heated chemiluminescent detector
HCN	Hydrogen cyanide
HFID	Heated flame ionisation detector
IMEP	Indicated mean effective pressure [Bar]
IPSP	Intake port static pressure [Pa]
IWG	Inch water gauge [In]
JLR	Jaguar-Land Rover

LHV	Lower heating value [kJ/kg]
Ltd	Limited
MAIM	Metal intake manifold
MDA	Measure Data Analyzer
MFB	Mass fraction burn [%]
NDIR	Non-dispersive infrared
NEDC	New European Driving Cycle
NI	National Instrument
NH <sub>3</sub>	Ammonia
NO	Nitric oxide
NO <sub>2</sub>	Nitrogen dioxide
NO <sub>x</sub>	Nitrogen oxides
N <sub>2</sub> O	Nitrogen dioxide
NVH	Noise vibration and harness
PAH	Polycyclic aromatic hydrocarbon
PAIM	Plastic air intake manifold
PM	Particulate matter
	RME          Rapeseed methyl ester
RH	Relative humidity [%]
RME	Rapeseed ethyl ester
RoHR	Rate of heat release [J/CAD]
SI	Spark ignition
SOC	Start of combustion [CAD]
SOI	Start of injection [CAD]
THC	Total hydrocarbon
TDC	Top dead centre
ULSD	Ultra low sulphur diesel
VA	Virtual array
VGT	Variable geometry turbocharger
VPA	Valve plate angle [degree]

## LIST OF SYMBOL

D	Engine cylinder bore [m]
$d_f$	Diffusive fuel fraction
g	Gravity [ $m/s^2$ ]
$H_g$	Heat transfer coefficient [ $W/m^2k$ ]
K	Kelvin [K]
N	Engine speed [rpm]
$N_B$	Brake engine speed [rpm]
$O_2$	Oxygen
p	Pressure [Pa]
$P_b$	Engine brake power [W]
$P_{drop}$	Pressure drop [Pa]
$p_f$	Premixed fuel fraction
$P_{mot}$	Cylinder pressure at motored condition [Pa]
$P_r$	Reference pressure [Pa]
Q	Heat release [J]
$R_{swirl}$	Swirl ratio
t	Time [s]
T	Temperature [K]
$T_b$	Brake torque [Nm]
$t_f$	Tail fuel fraction
$T_r$	Reference temperature [K]
$u$	Local velocity at x-axis [ $m/s^2$ ]
$v$	Local velocity at y-axis [ $m/s^2$ ]
V	Volume [ $m^3$ ]
$v_c$	Characteristic velocity [ $m/s^2$ ]
$V_d$	Volume displacement [ $m^3$ ]
$v_m$	Mean piston speed [m/s]
$V_r$	Reference volume [ $m^3$ ]
$v_s$	Swirl velocity [m/s]

$w$	Local velocity at z-axis [m/s]
$\varepsilon$	Dissipation rate [ $\text{m}^2/\text{s}^3$ ]
$\mu$	Viscosity [Pa.s]
$\lambda$	Air excess ratio
$\tau$	Shear stress [Pa]
$\kappa$	Kinetic energy [ $\text{kg}\cdot\text{m}^2/\text{s}^2$ ]
$m_f$	Fuel mass flow rate [kg/s]
$\eta_{th}$	Engine thermal efficiency [%]
$\rho$	Density [kg/m <sup>3</sup> ]
$\gamma$	Ratio of specific heat
$\Delta\theta_{\text{delay}}$	Ignition delay [s]
$\theta_b$	Start of combustion [CAD]
$\Phi$	Equivalence ratio

## LIST OF FIGURES

- Figure 2.1** Schematic diagram of typical AIS system for diesel engine
- Figure 2.2** Intake duct system with porous material
- Figure 2.3** Example of variable intake manifold (a) Six cylinder variable intake manifold, DaimlerChrysler. (b) Four cylinder variable intake manifold, Opel. (c) Six cylinder variable intake manifold, Volkswagon. (d) Four cylinder variable intake manifold, Volkswagon.
- Figure 2.4** Optimisation of intake port by CFD
- Figure 2.5** The pressure level and streaklines of the airbox (Vita, 2002)
- Figure 2.6** Coefficient of pressure in the surface of Audi 100 II and Audi 100 III.
- Figure 2.7** Chemical reaction of triglyceride and methanol to produce biodiesel
- 
- Figure 3.1** Simulation flow chart
- Figure 3.2** Three dimensional geometry of the Freelander air intake system.
- Figure 3.3** Close view of Freelander intake grill
- Figure 3.4** Two different grid with y-y' axis marked on the cross section of the 'bridge'.
- Figure 3.5** Shows the velocity magnitude at Y-Y' axis for Grid 1 and Grid 2.
- 
- Figure 3.6** Commercial steady flow test bench (a) SuperFlow (Superflow 2008), (b) Cussons (Cussons 2008)
- Figure 3.7** Schematic diagram of steady flow test bench.
- Figure 3.8** Performance curve for SECOMAK pump model 587/2
- Figure 3.9** Photograph of the Freelander air intake grill.
- Figure 3.10** Pressure measurement locations on intake duct
- Figure 3.11** Incline manometer model Type 504 by Airflow Instrument Ltd.
- Figure 3.12** Photograph of the orifice plate by Roxspur Measurement & Instrumentation Ltd
- Figure 3.13** Photograph of steady flow test bench

- Figure 3.14** Typical  $p$ - $V$  diagram of a four-stroke cycle (Heywood 1988)
- Figure 3.15** Photograph of test engine
- Figure 3.16** Dynamometer and controller system
- Figure 3.17** Schematic diagram of fueling system on a V6 diesel engine
- Figure 3.18** Schematic diagram of a cooling system on a V6 diesel engine
- Figure 3.19** Exhaust gas analyzer, (a) AVL DiGAS 440 and  
(b) CEB200 exhaust gas analyzer
- Figure 3.20** Arrangement of a National Instrument DAQ Card, connector box and PC
- Figure 3.21** GUI of LabVIEW code for data display and record
- Figure 3.22** Schematic diagram of V6 diesel engine system
- Figure 3.23** AVL Piezo Amplifier
- Figure 3.24** GUI of LabVIEW 4 to analyse the in-cylinder pressure
- Figure 3.25** Main panel of INCA GUI to monitor the engine operation
- 
- Figure 4.1** Freelander travel under specific level of the water (Motortorque 2008).
- Figure 4.2** Pressure distributions on Freelander vehicle body
- Figure 4.3** Velocity vector of fluid flow around the vehicle body
- Figure 4.4** Pressure drop measured on five different locations at different mass flow-rate.
- Figure 4.5** Velocity vector on x-z plane inside the duct [m/s]
- Figure 4.6** Contour of static pressure on x-z plane inside the duct [Pa]
- Figure 4.7** Contour of static pressure on intake grill [Pa]
- Figure 4.8** Path lines color by particle ID
- Figure 4.9** Pressure drop measured and calculated at P2 against different mass flow rates.
- Figure 4.10** Contours of static pressure on (a) x-z plane inside the duct (b) grill surface
- Figure 4.11** Vectors of velocity on the grill side
- Figure 4.12** Path lines colored by particle ID.
- 
- Figure 5.1** Ricardo WAVE software graphic user interface panel

- Figure 5.2** Schematic diagram of the engine model.
- Figure 5.3** The preloaded component of engine component available from elements panel
- Figure 5.4** Valve lift profile for the V6 engine
- Figure 5.5** Valve lift profile in Ricardo WAVE software (a) intake valve lift profile, (b) exhaust valve lift profile
- Figure 5.6** Injection strategies for the V6 engine
- Figure 5.7** Compressor map of a VGT turbocharger (GT15)
- Figure 5.8** Power and torque curve
- Figure 5.9** Calibration of mass air flow and bsfc.
- Figure 5.10** Intake port static pressure responses as VPA altered.
- Figure 5.11** Breathing performance (a) Engine air flow; (b) Total volumetric of the engine under varies intake pressure
- Figure 5.12** Engine performances as a function of engine speed, (a) engine brake power, (b) engine brake torque
- Figure 5.13** Engine performances as a function of engine speed. (a) Brake thermal efficiency and (b) maximum of in-cylinder pressure
- Figure 5.14** Exhaust properties (a) Exhaust gas temperature and (b) exhaust port static pressure
- Figure 5.15** Engine fueling and pumping performance (a) bsfc (b) brake mean effective pressure
- Figure 6.1** The 16 test operating conditions from NEDC (Chuepeng 2008).
- Figure 6.2** Air excess ratio and fuel injection pressure against test mode
- Figure 6.3** Start of injection for pilot and main injection against test mode
- Figure 6.4** Brake specific fuel consumption and engine thermal efficiency against test mode
- Figure 6.5** In-cylinder pressure profile against crank angle degree
- Figure 6.6** Emission of NO<sub>x</sub> and a comparison with peak pressure as a functions of test mode.
- Figure 6.7** Carbon monoxide and total hydrocarbon against test mode.

- Figure 6.8** Cylinder pressure and rate of heat release for ULSD and RME at engine speed of 1550rpm, 67 Nm brake torque
- Figure 6.9** Ignition delay and peak pressure for ULSD and RME at engine speed of 1550rpm.
- Figure 6.10** Emissions of NO<sub>x</sub> and THC for ULSD and RME fuelling at engine speed of 1550rpm
- Figure 6.11** Emissions of particulate matter, engine running at 1550 rpm, 3.1 bar BMEP
- Figure 6.12** Response of injection pressure in the engine as a consequence of EGR mode and fuel temperature. E1 and E0 represent the EGR mode ON and OFF respectively
- Figure 6.13** In-cylinder pressure and rate of heat release for three different fuel temperatures.
- Figure 6.14** Maximum of in-cylinder pressure
- Figure 6.15** Close-up view of in-cylinder pressure during the main injection period.
- Figure 6.16** Close-up view of rate of heat release during premixed combustion.
- Figure 6.17** Brake specific fuel consumption
- Figure 6.18** Engine efficiency
- Figure 6.19** Emissions of NO<sub>x</sub>
- Figure 6.20** Emissions of CO in the exhaust gas as a function of fuel temperature
- Figure 6.21** Emissions of THC in the exhaust gas as a function of fuel temperature
- Figure 6.22** Manifold absolute pressures
- Figure 6.23** EGR controlled by the EMS
- Figure 6.24** Peak pressure and thermal efficiency at different modes of injection and EGR operation
- Figure 6.25** Brake specific fuel consumption at 1550 rpm, brake torque 67 Nm
- Figure 6.26** Cylinder pressure and rate of heat release at 1550 rpm, brake torque 67 Nm
- Figure 6.27** Mass fraction burn at 1550 rpm, brake torque 67 Nm
- Figure 6.28** Emissions of NO<sub>x</sub> at 1550 rpm, brake torque 67 Nm
- Figure 6.29** Emissions of unburned hydrocarbons at 1550 rpm, brake torque 67 Nm
- Figure 6.30** Emission of carbon monoxide at 1550 rpm, brake torque 67 Nm

- Figure 6.31** Emission of particulate matter at 1550 rpm, brake torque 67 Nm
- Figure 7.1** Air flow rate at engine speed of 1550rpm (a) low load, BMEP 3.1bar ,  
(b) part load, BMEP 4.7bar
- Figure 7.2** Fuel flow rate at engine speed of 1550rpm (a) low load, BMEP 3.1bar ,  
(b) part load, BMEP 4.7bar
- Figure 7.3** Cylinder pressure for ULSD and RME at different pressure drops at  
engine speed of 1550rpm (BMEP 4.7bar)
- Figure 7.4** Ignition delay as consequences of pressure drop and engine load at  
engine speed of 1550rpm; (a) low load, BMEP 3.1bar (b) part load,  
BMEP 4.7bar
- Figure 7.5** Brake specific fuel consumption at engine speed of 1550rpm; (a) low  
load, BMEP 3.1bar (b) part load, BMEP 4.7bar
- Figure 7.6** Efficiency of the engine at engine speed of 1550rpm; (a) low load,  
BMEP 3.1bar (b) part load, BMEP 4.7bar
- Figure 7.7** Exhaust emissions of NO<sub>x</sub> at engine speed of 1550rpm (a) low load,  
BMEP 3.1bar (b) part load, BMEP 4.7bar
- Figure 7.8** Emissions of carbon monoxide at engine speed of 1550rpm (a) low  
load, BMEP 3.1bar (b) part load, BMEP 4.7bar
- Figure 7.9** Emissions of total hydrocarbon at engine speed of 1550rpm; (a) low  
load, BMEP 3.1bar (b) part load, BMEP 4.7bar
- Figure 7.10** Fuel flow rate at engine speed of 1550rpm (a) low load, BMEP 3.1bar  
(b) part load, BMEP 4.7bar
- Figure 7.11** Air flow rate at engine speed of 1550rpm (a) low load, BMEP 3.1bar  
(b) part load, BMEP 4.7bar
- Figure 7.12** Engine excess air ratio at engine speed of 1550rpm (a) low load,  
BMEP 3.1bar (b) part load, BMEP 4.7bar

- Figure 7.13** Fuel injection pressure at engine speed of 1550rpm (a) low load, BMEP 3.1bar (b) part load, BMEP 4.7bar
- Figure 7.14** Brake specific fuel consumption at engine speed of 1550rpm (a) low load, BMEP 3.1bar (b) part load, BMEP 4.7bar
- Figure 7.15** Engine efficiency at engine speed of 1550rpm (a) low load, BMEP 3.1bar (b) part load, BMEP 4.7bar
- Figure 7.16** Exhaust emission of NO<sub>x</sub> at engine speed of 1550rpm (a) low load, BMEP 3.1bar (b) part load, BMEP 4.7bar
- Figure 7.17** Exhaust emission of CO at engine speed of 1550rpm (a) low load, BMEP 3.1bar (b) part load, BMEP 4.7bar
- Figure 7.18** Exhaust emission of THC at engine speed of 1550rpm (a) low load, BMEP 3.1bar (b) part load, BMEP 4.7bar

## LIST OF TABLES

<b>Table 3.1</b>	Specification of wind tunnel
<b>Table 3.2</b>	Specification of test engine
<b>Table 3.3</b>	Specification of dynamometer
<b>Table 3.4</b>	Fuel properties
<b>Table 4.1</b>	Boundary conditions for numerical analysis at different air speeds
<b>Table 4.2</b>	Experimental against predicted pressure drop at location P2.
<b>Table 4.3</b>	Simulation results of mass flow rate
<b>Table 5.1</b>	Detail parameter of a Lion V6 diesel engine
<b>Table 5.2</b>	Comparison of the test and simulation result
<b>Table 5.3</b>	Mass air flow and bsfc of a V6 diesel engine
<b>Table 5.4</b>	Valve plate angle and intake port static pressure
<b>Table 6.1</b>	Engine operating conditions
<b>Table 6.2</b>	Parameters of injection in different modes
<b>Table 7.1.</b>	Pressure drop in air intake systems
<b>Table 7.2.</b>	Boost temperature in air intake systems

## List of Publications

- 1. Performance and Emission Characteristics of High Performance Diesel Engine Operating with Biodiesel.**  
R. Mamat, H.M. Xu, M.L.Wyszynski (2008), Graduate School Poster & Networking Conference, 11 June 2008, The University of Birmingham, United Kingdom
- 2. CFD Analysis of Air Intake System with Negative Pressure on Intake Grill**  
R. Mamat, A.F.Mahrous, H.M. Xu, M.L.Wyszynski (2008), SAE International Powertrains, Fuels and Lubricants Congress, June 23-25, 2008, Shanghai, China. SAE 2008-01-1643
- 3. Effect of Exhaust Gas Temperature on Engine Performance and Emissions of a Conventional V6 Diesel Engine Operating on Biodiesel & Diesel Fuel with Exhaust Gas Recirculation (EGR)**  
R. Mamat, S. Chuepeng, H.M. Xu, M.L.Wyszynski (2008), United Kingdom-Malaysia Engineering Congress 2008, London, 14-15 July 2008
- 4. Optimising the Airflow of a Land Rover Air Intake System**  
R. Mamat, H.M. Xu, M.L.Wyszynski (2008), Universities Internal Combustion Engines Group Conference (UnICEG), Poster presentation, 17 December 2008, The University of Birmingham, United Kingdom
- 5. Effect of Air Intake Pressure Drop on Performance and Emissions of a Diesel Engine Operating with Biodiesel and Ultra Low Sulphur Diesel (ULSD)**  
R. Mamat, N.R.Abdullah, H.M. Xu, M.L.Wyszynski A.Tsolakis (2009), International Conference on Renewable Energy and Power Quality, 15-17 April 2009, Valencia, Spain

6. **Effect of Fuel Temperature on Combustion and Emissions of a Common Rail Diesel Engine**  
R. Mamat, N.R.Abdullah, H.M. Xu, M.L.Wyszynski, A.Tsolakis (2009) 2009 SAE International Powertrains, Fuels and Lubricants Meeting June 15-17, 2009 Florence, Italy, SAE Paper No. 2009-01-1896
7. **Effect of Exhaust Gas Recirculation (EGR) with Multiple Injections on Combustion Pattern in a Common Rail Diesel Engine**  
R. Mamat, N.R.Abdullah, H.M. Xu, M.L.Wyszynski, A.Tsolakis (2009), 12th EAEC European Automotive Congress 2009, 29th June - 1st July 2009, Bratislava, Slovak Republic.
8. **Optimization of High Injection Pressure and EGR on Engine Performance and Emissions using V6 Common Rail Diesel Engine,**  
N.R.Abdullah, R. Mamat, A.Tsolakis, M.L.Wyszynski, H.M. Xu (2009) 9th International Conference on Engines and Vehicles. September 13-18, 2009 Capri, Naples, Italy. SAE Paper No. 2009-24-0049
9. **Contributions of Injection Duration (dSOI) to the Engine Performance and Emissions in Multiple Injections V6 Diesel Engine Operating with a Variation of Injection Pressure**  
N.R.Abdullah, R. Mamat, A.Tsolakis, M.L.Wyszynski, H.M. Xu (2009), Journal of KONES Internal Combustion Engines, European Science Society of Powertrain and Transport Publication. (Journal Accepted)
10. **Influence of Boost Temperature on a Common Rail Diesel Engine Operating with Biodiesel**  
R. Mamat, N.R.Abdullah, H.M. Xu, M.L.Wyszynski, A.Tsolakis (2009) FISITA 2010 World Automotive Congress May 30 - June 4, 2010, Budapest, Hungary (Abstract submitted)

11. **Modelling of a V6 Diesel Engine Operating with Biodiesel in One-Dimensional Engine Simulation**

R. Mamat, N.R.Abdullah, Jun Zhang, H.M. Xu, M.L.Wyszynski, A.Tsolakis  
(2009) Prepared for Journal of Automobile Engineering

# **CHAPTER 1**

## **INTRODUCTION**

The first chapter of the thesis is devoted to the general overview of a diesel engine, in relation to the combustion and emissions. The chapter presents the operation of a diesel engine with alternative fuel, specifically biodiesel. It also discusses the air intake system and its evolution to meet the current demand on emission regulation without compromising on performance issues. At the end of the chapter, the objectives of the research and thesis outline are presented.

### **1.1 Background**

Automotive engines are one of the major sources of pollutant, which is harmful to living creatures and causes damage to the environment (Liu 1999; Hester et al. 2004). The transportation sector accounted for 21% of all CO<sub>2</sub> emissions worldwide in 2002 which is the major cause to the global warming issues. In recent years, many countries have applied stringent emission standards to automotive manufacturers. Therefore, modern diesel engines are equipped with many features such as EGR and common rail fuel injection system to control their emissions while maintaining or improving the performance of the engine. Furthermore, the future

generation of diesel engine should be able to work with alternative fuels such as biodiesel and alcohol due to limited sources of fossil diesel fuel, and environmental concern. Much research has been conducted on biodiesel as an alternative to the diesel engine fuels (Kawano et al. 2006; Chuepeng et al. 2007; Szybist et al. 2007; Tsolakis et al. 2007; Zheng et al. 2008).

### **1.1.1 Diesel Engine Technology**

The diesel engine was named after Dr Rudolf Diesel who in 1897 invented an engine with direct injection of liquid fuel into the combustion chamber. The engine was originally designed to work with peanut oil. The diesel engine is also known as a compression ignition (CI) engine due to its principles of cycles. The ignition of fuel in the combustion chamber occurs due to high temperature and pressure during the compression stroke. The diesel engine is not throttled the amount of fresh air enters the engine as Otto cycles is used to control the output power. Instead, the power is controlled by the amount of fuel injected into the cylinder. Thus designing a good air induction system (AIS) is vital to a diesel engine to achieve higher engine performance.

Diesel engine performance is well known to be limited by the formation of smoke, which forms if there is inadequate mixing of the fuel and air (Ferguson 2001). Therefore, much research has been conducted on optimisation of the AIS as well as the combustion chamber to improve the diesel mixing process. Many attempts have been conducted to improve emissions by new techniques and devices such as exhaust

gas recirculation system (EGR), after treatment technology, catalytic converter. Others have tried with alternative fuels such as biodiesel and alcohol.

EGR technology is one of the most promising techniques to reduce emissions especially NO<sub>x</sub>. A number of reports can be found in the literature (mainly experimental) dealing with the effects of EGR to reduce NO<sub>x</sub> in diesel engines and have proved the effectiveness of this technique (Ladommatos et al. 1998; Yang et al. 2002; Zheng et al. 2004; Kawano et al. 2007). There are three renowned explanations on how the EGR reduces the NO<sub>x</sub> emissions. The EGR increases the ignition delay, increases the heat capacity of the intake charge and dilutes the intake charge with inert gas component (Pierpont et al. 1995). The detailed explanation on this subject can be found in many books and technical papers (Heywood 1988; Abd-Alla 2002; Musculus 2004; Maiboom et al. 2008).

The injection system of diesel engines also evolved a step further to achieve higher engine performance and lower the exhaust gas emissions. One of the advanced fuel injection systems is known as common-rail fuel injection. The main advantage of common rail system is its ability to vary injection pressure and timing over broad scale (Kimberley 2004). The quality of combustion process in diesel engines is highly dependent on fuel injection parameters (Heywood 1988). The diesel fuel injections systems produce an heterogeneous spray process in the combustion chamber. Therefore, accurate control over fuel injection, and thus spray formation, is crucial for diesel engines to increase their performance and lower the emission level. The design of the common rail fuel injection system, with its flexible control of injection into multiple injections, allows the engine and the injection system to be synchronized to

achieve the optimum conditions. The common-rail system thus plays a major role in increasing specific power output, lowering fuel consumption and decreasing noise and exhaust emissions from diesel engines (Kimberley 2004). The use of multi injection in diesel combustion is practical to reduce NO<sub>x</sub> and has been proved by many groups especially by Reitz and his colleagues (Patterson et al. 1994; Montgomery et al. 1996). The extensive research on the Perkins Engine recently, also proved that the combination of EGR and high pressure fuel injection (up to 1600 bar) on a 1.0litre/cylinder engine has demonstrated the capability of achieving less than 3.0 g/kWh NO<sub>x</sub> and 0.08 g/kWh particulate without the need for exhaust after-treatment (Dennis et al. 1999).

The essential function of the engine air intake system is to provide sufficient air to be mixed with fuel in the engine combustion chamber. The fundamental design of the air intake system has not changed too much since when it was used in internal combustion engines. The system normally comprises of dirty duct, air box, air cleaner, clean duct, intake manifold plenum, and intake manifold runner.

Engine performance is sensitive to induction depression especially for Internal Combustion (IC) engines running without a turbocharger or supercharger. Turbocharger is widely used to increase the performance of the diesel engine. The engine operating without turbocharger suffers from a pressure drop of the air induction system. A positive pressure at the end of the grill would help to overcome such a drawback. Thus, most car manufacturers position the grill at the front of the vehicle to maximize the capability of the engine to consume more air. Furthermore, drawing air from the front of the vehicle can minimize the interior noise contribution

from the intake orifice. However, for those vehicles which have been designed to travel off-road, particularly in specific water levels, the air intake should be capable enough to cruise without sucking water into the engine. In the series of Range Rover vehicles, for instance, the grill intake currently points rearwards to the vehicle. Under wind tunnel conditions, aerodynamics tests have recorded a slightly negative depression in this area, a characteristic that can increase pressure drop on the air intake system.

The pressure drop across the air intake system is known to have a significant influence on the indicated power of the IC engine. The pressure drop is created due to the suction generated by the descending piston in the case of a naturally aspirated engine. The pressure drop along the intake system is very dependant on engine speed and load, the flow resistance of different elements in the system, the cross sectional area through which the fresh charge moves, and the charge density (EPA).

### **1.1.2 Alternative Fuels for Diesel Engines**

The exhaust emissions generally result from the combustion of fossil fuel in vehicle engines. Moreover, the mineral diesel fuel itself is toxic and may cause long term adverse effects to the aquatic environment. Experimental studies have found that the polycyclic aromatic hydrocarbons contained in diesel may induce skin cancer, as reported on gas oil safety data sheet by BP Oil UK Ltd (BP 1998). Therefore, research on new alternative fuels is very important to overcome these problems.

Biodiesel is one of the most important renewable energy resources, which is produced from vegetable oil or animal fat by transesterification of triacylglycerols, yielding monoalkyl esters of long-chain fatty acids with short-chain alcohols (Meng et al. 2008). The main benefit of biodiesel is that it is 'carbon neutral'. Although the engines running on biodiesel produce more CO<sub>2</sub> compared to conventional diesel fuels, if the analysis includes the carbon cycle, the use of biodiesel actually emits less CO<sub>2</sub> to the atmosphere. The biodiesel could be used on its own or blended with conventional fossil fuel without having to make any modification to the standard diesel engines because biodiesel has comparable properties to diesel (Agarwal 2007; Tsolakis et al. 2007).

The advantage of biodiesel has been reported by many researchers as renewable energy, non-toxic, biodegradable and sulphur free (Labeckas et al. 2006; Bozbas 2008). In addition, a mixture of biodiesel with standard diesel fuel improves the lubricating properties of the fuel and reduced cylinder friction (Nwafor 2004).

### **1.1.3 Combustion in Diesel Engines**

The combustion process in compression ignition (CI) engines is very complicated. Much research has been conducted to study the behaviour of the combustion process in an engine cylinder. In a CI engine, the combustion started just after a few crank angle degree of start of injection. The chemical reaction occurs in an engine cylinder which produce diffusion flame at the interface between fuel and

air. The heat release begins and increases as a rapid burning spreads through combustion chamber and decreases as the available oxygen is depleted.

The combustion process can be classified in two phases. Premixed combustion and mixing controlled combustion. The liquid fuel supplied to the engine is compressed into a finely atomized state, vaporized, and penetrates into the hot and highly compressed air in the combustion chamber. The combustion starts when the local temperature reaches or goes above the auto-ignition temperature. The time interval between the start of injection (SOI) and the start of combustion (SOC) is derived as ignition delay. This parameter plays an important role to the quality of combustion in a diesel engine.

The initial combustion of the fuel vapour-air mixture is derived as the premixed combustion phase. The remaining combustion process is called the mixing controlled combustion phase. In diesel combustion, the double peak shape of heat release rate appears as a result of two phase combustion occurred during combustion stroke. The first peak occurs during the premixed combustion. The heat release curve in the premixed combustion phase is relatively independent of engine load as the initial mixing is independent of engine injection duration. The second peak of the heat release curve resulted from the mixing controlled combustion phase. The magnitude and duration of the mixing controlled heat release is proportional to the duration of injection. The heat release curve is normally derived from the cylinder pressure data generally from -20 degree BTDC to 40 degree ATDC.

Cylinder pressure is one of the crucial parameters to be measured to gain deep understanding on quantitative information on the progress of combustion in the engine cylinder (Heywood 1988; Senatore et al. 2000). The assumptions made on the calculation of heat release rate are including quasi static (temperature & pressure), uniform gases in cylinder, with no dissociation of the chemical compounds present after combustion, cylinder engine is considered closed system and specific heat of the gaseous mixture are calculated as a function of temperature. The shape of the heat release rate which represents different behaviors of combustion varies with engine design, speed and load (Lilly 1984).

## **1.2 Objectives and Approaches**

The main objective of this research is to conduct a computational and experimental study of the effect of air induction systems and biodiesel to the performance and emission level of a diesel engine. The study is divided into two major categories where the study has been conducted on AIS on off-engine mode and with the engine respectively. The volumetric efficiency is a measure of the performance of the AIS. This dimensionless number is depending on many factors in a very complicated modern diesel engine. One of the major factors which reduce the volumetric efficiency is the pressure difference between in-cylinder pressure and intake orifice. This pressure difference is resulted from the aerodynamic force on the vehicle skin and its magnitude depends on the speed of the vehicle. The study has been conducted on this variable by CFD commercial code FLUENT and the computational models will be validated against experimental data. The experimental

works on the AIS have been conducted on a state-of-the-art in-house design steady flow test bench.

The fuel is known to have an affect to the performance of an air induction system as explain in detail by Heywood (Heywood 1988). The exhaust temperature and pressure is highly influenced by the combustion progress of fuels in the engine cylinder. These parameters are definitely affecting the volumetric efficiency of the engine especially when the engine is equipped with turbocharger. Therefore this study includes the effect of the AIS variable to the engine operating with biodiesel as compared to ULSD as a base fuel. Further analyses have been conducted on combustion such as rate of heat release and mass fraction burn. The effect of these variables on emission levels is also discussed as consequences of the combustion.

The second stage of the study is to artificially simulate the pressure drop on AIS on a diesel engine operating at low load and part load conditions. As an extension to the research, several variables that affected the AIS performance have been investigated. These variables include

- Effect of pressure drop
- Effect of air intake temperature
- Effect of EGR.

### **1.3 Thesis Outline**

This thesis is devoted to the study of the air intake flow conditions and their contributions and effect to the performance and emission of a diesel engine operating with fossil diesel and biodiesel. Therefore thesis topics are categorized as introduction to diesel AIS, Computational Fluid Dynamics (CFD), steady-flow test, combustion in a diesel engine, emission and biodiesel as an alternative fuel.

Following this first chapter, which is intended to review the general knowledge and problem statement of the entire subject in the study, Chapter 2 is intended to review the fundamental topics covered in the study through a literature survey. These include computational as well as empirical solutions to the study. The research methodology approach of AIS modelling and steady flow test are addressed in Chapter 3. This chapter discusses details on the steady flow test rig setup as well as the diesel engine setup. The 3D model is validated and discussed with steady flow test results in Chapter 4. Chapter 5 is concerned with the 1D modelling of a Lion V6 engine and the validation results with experimental works. Chapter 6 is concerned with the general overview of a diesel engine operation with biodiesel fuel. The results include the performance and emissions measure both on ULSD and biodiesel. Chapter 7 is dealing with the effect of inlet temperature and pressure as the main intake manifold variable on a diesel engine operating with ULSD and biodiesel. Chapter 7 is also concerned with the effect of EGR and its effect on the pressure and temperature on AIS. The main conclusions of the presented work together with recommendations for future investigations are covered in Chapter 8.

## **CHAPTER 2**

### **LITERATURE REVIEW**

This chapter presents an introduction to the air intake system and the development of the technology to increase the performance of the air intake system. This chapter also describes the optimisation of the air intake system by computational fluid dynamics. In addition, the chapter discusses fundamental studies on diesel combustion and emissions with the effect of air intake system parameter. The chapter also covers application of biodiesel as alternative fuel to modern diesel engines.

#### **2.1 Air Intake System for Diesel Engines**

The basic function of an AIS is to deliver fresh air to the engine cylinder. The design of an AIS comes in many different lengths, shapes & geometry. Typical materials used to construct an AIS are cast aluminium, plastic, rubber (silicone) or composite materials (fiberglass, carbon fiber or kevlar). The main intentions of AIS design is to provide the cylinder with fresh air as much as possible so that more fuel can be injected thus more power produced from the engine. The geometry of an AIS has a strong influence on the volumetric efficiency in IC engines (Heywood 1988;

Winterbone et al. 1999). Therefore, intake manifold design must be carefully engineered and tuned to provide the greatest efficiency. Modern design of an AIS for diesel engines consists of many components which are necessary for a variety of reasons. The most common components are EGR, turbocharger, intercooler, quarter-wave resonator, porous material duct and airbox. Several of these components will be discussed in detail in Chapter 2.1.2. Figure 2.1 shows the schematic diagram of an AIS for a diesel engine with a turbocharger and EGR system.

A well designed AIS increases the air flow velocity until it travels into the combustion chamber, while minimizing the turbulence and restriction of flow. The experiment is normally conducted on a steady flow test bench to provide a better understanding on the flow behaviour. Computer simulations have successfully been used as a good solution at the design stage to minimise the time and cost.

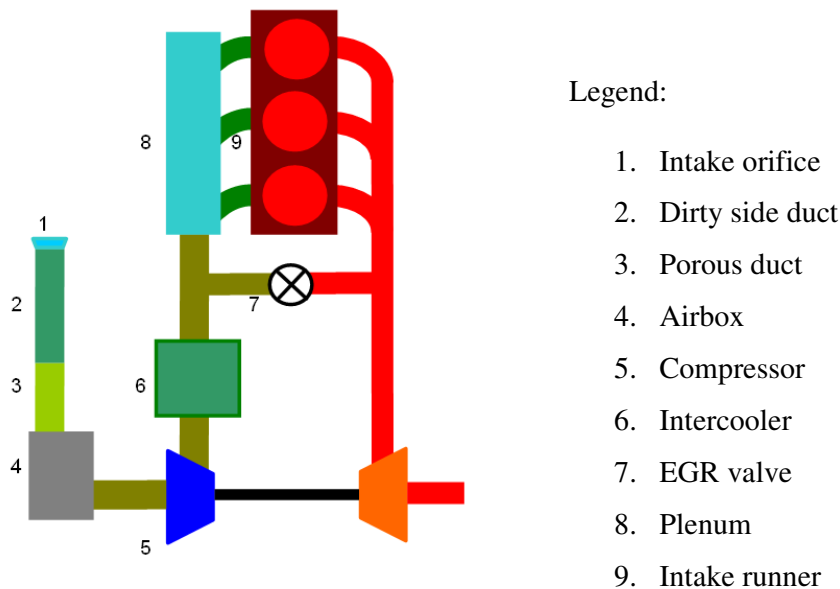


Figure 2.1 Schematic diagram of typical AIS system for diesel engine

Modern design of an AIS has to meet the customer requirements, higher efficiency and legislation. Criteria for a good AIS design can be summarized as follows;

- High volumetric efficiency
- Low noise level (good NVH)
- Light weight design
- Low cost of material and production
- High thermal insulation.

Therefore, much research is conducted on designing new systems of intake manifold with the new strategies to maximise the performance of the vehicles air intake system. In general, the potential strategies used in designing an AIS are as follows;

- Improve internal surface roughness of AIS to reduce air resistance
- Increase the diameter of intake manifold
- Reduce sharp corner, thus providing straight flow
- Tuning the length of intake manifold to provide optimum air flow base on engine speed
- Choose the right place for intake orifice to get clean air (without dust), cooler air and high pressure spot.

### **2.1.1 System Component and Development**

The designer faces a challenge to design a good AIS based on many factors, not only just on performance, but also in terms of production practicality, cost effectiveness, material selection and limited space in the engine compartment. Recently, a plastic air intake manifold (PAIM) has been adopted into almost all modern ICE engines (Tanaka et al. 2007). The advantages of the PAIM are light mass weight, low cost, high thermal-insulation efficiency. PAIM, which has a complex design for stability and production reasons, often has a better characteristic in the low frequency band (Paffrath et al. 1999). Recent studies have shown that the PAIM also reduces air pressure loss compared with a metal air intake manifold (Tanaka et al. 2007). This is because the surface roughness of a PAIM is much better than a MAIM. The production nature of the MAIM through sand casting, resulted in the poor surface finish.

However, a PAIM also has disadvantages such as low burst pressure, higher noise and vibration under certain engine speed and conditions. Recently, research has been conducted to improve the properties of a PAIM by the used of CAE (Tanaka et al. 2007). With regard to NVH, a plastic intake manifold is considered somewhat negative since it is less rigid and less dense than an aluminium one (Lee 1998).

Much research activity has been conducted to improve the NVH behaviour of the PAIM (Lee 1998; Siavoshani et al. 2001; Song et al. 2005). Most used CAE successfully to understand the behaviour of the PAIM under specific engine load and speed. Many AIS today include a silencer to minimize the noise entering the vehicle cabin. However, silencers impede air flow and create turbulence which reduces

engine power. One of the successful methods to improve NVH of a PAIM is by using porous materials as an intake duct. Porous material such as polyester fibre is used as the intake manifold in order to reduce air resonance in the air intake duct (Hirose et al. 2002; Kitahara et al. 2005). High frequency component in the intake manifold is reduced by the air escaping through the duct wall (Hirose et al. 2002). As a comparison, the decrease in noise is the same or less than the effect of the intake manifold resonator. Figure 2.2 shows the intake manifold with porous material.



Figure 2.2 Intake duct system with porous material (Kitahara et al. 2005).

Helmholtz resonators which are also known as quarter-wave resonators are frequently used as acoustic silencers in automotive air intake systems. The Helmholtz resonator consists of a short tube which connects to a main duct on one side and is closed on the other end. This configuration leads to large acoustic attenuation at frequencies where the length of the side branch is one quarter of the acoustic wavelength (Radavich et al. 2001). Much research has been conducted recently, by experimental as well as numerical calculation, in this topic to improve the AIS noise (Athavale et al. 1999; Radavich et al. 2001; Bozza et al. 2004).

The firing order of the engine and the valve timing lead to a transient pressure excitation at the runner outlets of an air intake manifold for an internal combustion engine. The resulting pressure waves in the intake port have a significant effect on volumetric efficiency. This natural air overcharge occurs at specific engine speed that corresponds to a perfect timing between the intake valve closing and the maximum pressure at the intake valve. Many attempts have been made to improve cylinder filling by making greater effect of kinetic energy and pressure waves. Experiments by Smith and Morisson in 1962 have proved that the different length of the manifold pipe gives a significant effect on cylinder filling (Smith 1971). The standard intake manifold has its geometry optimized for high speed power, or low speed, depending on the normal drive of the car. Variable intake manifolds introduce one or two more stages to deal with different engine speeds by changing their geometry.

The variable intake manifold system is also known as variable length intake manifold or resonance intake manifold. However, it is usually named by the manufacturer under their own trade mark such as Porsche's VarioRam, Mitsubishi's Cyclone, Volvo V-VIS and Mazda's VICS. Generally, a variable intake manifold employs two intake manifolds with different length to serve each cylinder. However, recently the variable intake manifold is designed to enhance the performance of AIS at all engine speed. The intake manifold with extra length causes greater drop below atmospheric pressure in cylinder pressure, followed by an increased rate of pressure recovery (Smith 1971). This resulted in the higher final pressure which gives better cylinder filling, thus improves torque output. The effect is obvious at low to mid range of crank angle speed, whereas at high speed, there is insufficient time for ram

effect to occur. Figure 2.3 shows several designs of variable intake manifold manufactured by Pierburg GmbH for different car makers.

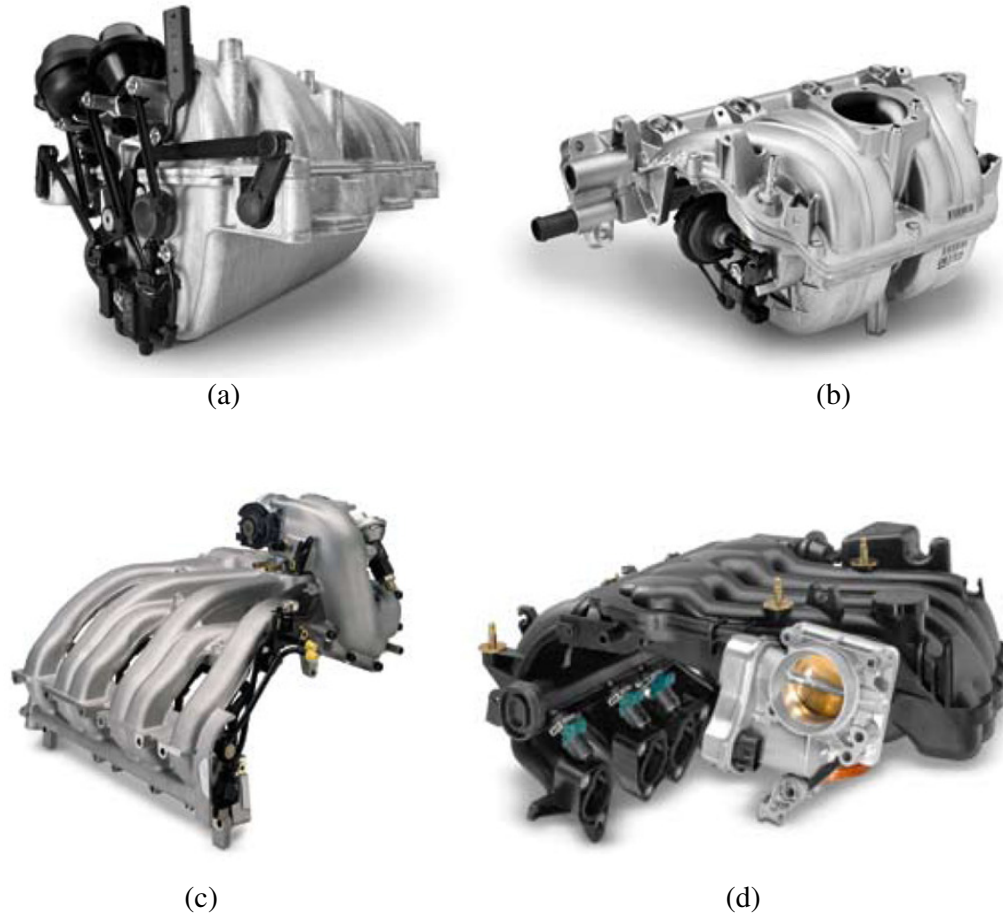


Figure 2.3 Example of variable intake manifold (Pierburg 2008). (a) Six cylinder variable intake manifold, DaimlerChrysler. (b) Four cylinder variable intake manifold, Opel. (c) Six cylinder variable intake manifold, Volkswagon. (d) Four cylinder variable intake manifold, Volkswagon.

A well designed AIS uses a heat isolator to segregate the intake manifold from the rest of the engine compartment, providing cooler air from the front or side of the engine bay. Carbon fibre is often used for the piping instead of metal, reducing weight and insulating the cool air from the engine heat. Carbon fibre and other

advanced composites (such as Kevlar) are expensive, and can be more aesthetic rather than functional. Mathew and his colleagues have investigated the use of Nylon 6,6 glass reinforced composite material for an AIS. The study includes the evaluations of this composite material in terms of the intake manifolds material key requirements such as thermal, heat aging, fatigue, impact, creep, stress and chemical resistance including multi fuels (Mathew et al. 1999). He suggests that nylon glass reinforced composite material is suitable for intake manifold applications as it has good properties such as strength and toughness, and excellent retention of properties after heat aging (Mathew et al. 1999). While another study by Chao has shown that nylon composite also has good NVH characteristic (Chao et al. 1999). Due to many advantages of composite material, it has become more and more popular choice among AIS designers. In the high-volume (Original Equipment Manufacturer) OEM market, injection molded composite intake manifolds have been growing steadily in application for the past 20 years (Agnew et al. 2004).

Much research has been conducted to improve the intake port geometry in cylinder heads. This is due to the fact that the intake port and inlet valve area is the smallest flow passageway on an AIS where the biggest pressure drop occurs. The port design determines the volumetric efficiency and in-cylinder charge motion of the engine which influences the thermodynamic properties directly related to the power output, emissions, fuel consumption and NVH properties (Gaikwad et al. 2008). Much research has been published on investigating the intake port geometry especially on how its influence the swirl and tumble flow behaviour in an in-cylinder engine (Kawashima et al. 1998; O'Connor et al. 1998; Li et al. 2000; Bevan et al.

2004). The swirl and tumble motion in the engine cylinder has a significant effect on mixture formation and combustion for DI diesel engines (Heywood 1988). As a result, the geometry, combination and orientation of two intake ports have important influences upon the flow interference, and therefore upon swirl ratio and flow coefficient of the intake system (Li et al. 2000). Figure 2.4 shows an example of how CFD can be utilised to optimise the intake port geometry.

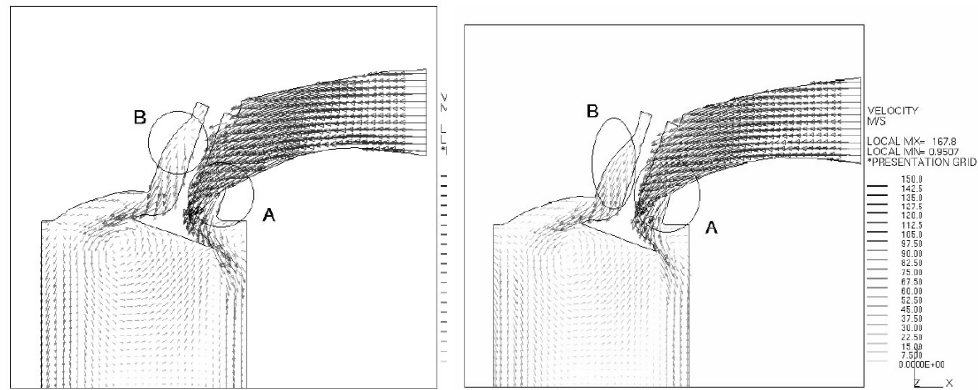


Figure 2.4 Optimisation of intake port by CFD (Kobayashi et al. 1999).

### 2.1.2 Optimisation of AIS by Computational Fluid Dynamics

The first generation of computational fluid dynamic (CFD) solutions appeared in the 1950s stimulated by the simultaneous advent of high performance computer systems. During this period of time, most of the CFD packages were used to solve the problems of high speed, high temperature re-entry body problems such as ballistic missiles (Wendt 1992). Nowadays, CFD solutions have been widely used from designing a very complicated space ship to the development of a swim suit, thanks to the rapid growth of the supercomputer. There are many commercial CFD codes such

as FLUENT, CFX and Star-CD. These commercial codes have made as easy as possible to use to minimize the time in solving fluid flow problems.

A huge amount of research has been conducted to optimize the AIS by completely manipulating the capability of modern day CFD. The analysis is normally conducted by separated components. For example, the computational analysis of 3D geometry of the intake port, intake manifold runner, intake plenum, airbox with air-filter as well as air duct system from the dirty side to the clean side of an AIS. Figure 2.5 shows the pressure levels and streaklines of the airbox of a race car. The simulation result clearly shows the pressure distribution on the air box and runner as well as the path line of the fluid flow. This is extremely important for the designer of the AIS to optimise the flow rate of the air for specific engine speed and load.

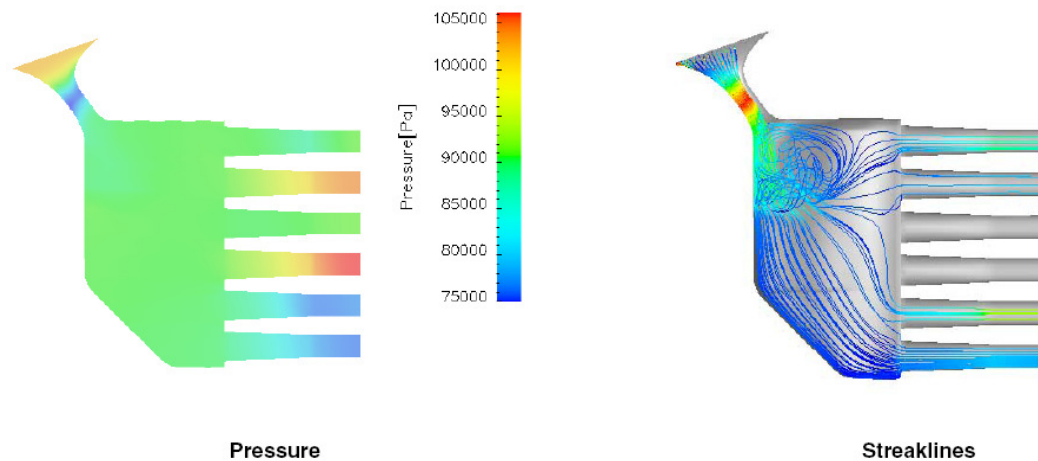


Figure 2.5 The pressure level and streaklines of the airbox (Vita, 2002)

None of the research appearing in the literature is related to the effect of negative pressure in the air intake grill on the AIS. For that reason, this research is

intended to study the effect of static pressure due to aerodynamic force on the vehicle surfaces to the performance of the AIS. This is one of the resistance factors on an AIS that have been studied by numerical analysis in this thesis. The cross flow velocity magnitude and vector are consequences of the magnitude of ambient air velocity flow. This numerical analysis is simulating the vehicle travel on the road at specified speed.

The AIS of a Freelander consists of an intake grill, intake orifice, dirty side duct, porous duct, airbox with air filter, clean side duct and quarter-wave resonator. The CFD analysis has been conducted in two stages. First, the simulation only focuses on the grill, intake orifice and dirty side duct. This is to simplify the initial simulation process. Thus, any unexpected error that occurs can be treated instantaneously. Secondly, the simulation is for the whole AIS so that the flow behaviour over the inside duct can be visualized qualitatively.

A number of studies on vehicle aerodynamics reported in the literature have shown that the pressure gradient on the surface of the vehicles varies according to the specific location of the vehicle surface (Bayraktar et al. 2006; Tsubokura et al. 2008; Zhu et al. 2008). Typically, the highest pressure occurred at the front of the vehicle. This position is believed to be the best location to place the intake orifice in terms of maximum volumetric efficiency. It is well known that the positive pressure at the intake orifice will provide an extra boost effect on the AIS. However, the main disadvantage of this position for off-road vehicles is that the wading performance is reduced. Figure 2.6 shows the typical pressure coefficient on the surface of a vehicle

(Audi 100 and Audi 100 II). It clearly shows that the maximum pressure occurred at the front of the vehicle

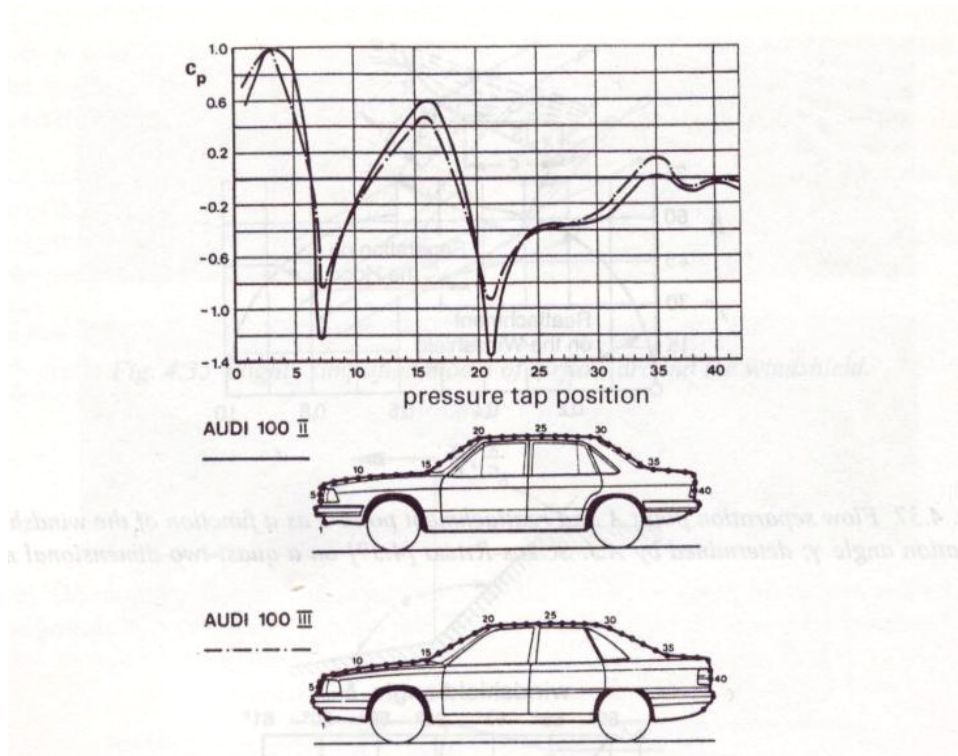


Figure 2.6 Coefficient of pressure in the surface of Audi 100 II and Audi 100 III. (Hucho, 1998)

The result from the simulations of the vehicle body clearly shows that the highest pressure was measured on the front of the vehicle. However, due to several factors, the designer has chosen to locate the intake orifice on the surface side of the vehicle near the top of the side fender. The static pressure in this position has a lower than atmospheric pressure level. As this pressure gradient depends on the velocity of the ambient air, therefore the volumetric efficiency also depends on ambient air speed.

### 2.1.3 One-dimensional Modelling of an Air Intake System

The application of computer simulation techniques to improve internal combustion engines has been rapidly expanding over the last decade. These techniques offer reliable predictions on the effect of engine parameters on engine performance. Moreover, the computational simulation presents information on physical quantities that are quite difficult to measure. One-dimensional (1D) modelling of engine performance and gas dynamic is widely used in automotive industries to reduce development lead-time and risk while improving the quality of the engines (Venugopalan et al. 2005; Alcini et al. 2006; Inagaki et al. 2008). There is a lot of available software on the market which offers 1D solutions such as Ricardo WAVE, AVL Boost and GT Power. All of this software offers a wide range of advanced tools to help to improve the speed, accuracy and quality of simulation. Many of the engine parameters such as intake and exhaust manifold, valves, injector, compression ratio, and engine geometry can be altered to determine their effects on engine performance. The Ricardo WAVE engine model like many other one-dimensional software is a time-dependent simulation of in cylinder processes where the solutions are based on the equations of mass and energy. The software provides fully integrated time-dependent fluid dynamic and thermodynamic calculations using a one-dimensional formulation.

Many research reports have been published which have successfully used the software to optimise the engines. Chen and his colleagues have used the 1D simulation code to develop a comprehensive model for the liquid fuel spray (Chen et al. 2004). The fuel spray model consists of droplet dynamics and evaporation, spray-wall impingement, wall film dynamics and evaporation in one-dimensional gas flow

calculation. The result from the simulation was validated with measurement data, including the single droplet evaporation, spray tip penetration and engine transient operations. Gilkes and his colleagues have used the Ricardo WAVE software to analyse the transient performance of a turbocharged diesel engine (Gilkes et al. 2008). The engine was equipped with the two point air injection system. The effect of the system was carefully studied on transient performance of the engine. The simulation results have been compared with experimental works in terms of engine performance, compressor performance and emission output of the engine. The model has shown that the two point injection system significantly improved both the engine performance and emission level. Bai and his colleagues have been working on 1D simulation on a diesel engine (Bai et al. 2008). The research was intended to study the effects of compression ratio, fuel supply advance angle and valve timing system on performance of a diesel engine. The simulation results were compared with experimental data which show good agreements between experiment and simulation.

## **2.2 Biodiesel as an Alternative Fuel**

### **2.2.1 Biodiesel Production, Policies and Standardisation**

Biodiesels are available alternative fuels which have a promising future as a substitute for conventional diesel. In general, the production of biodiesel is normally based upon locally available sources. Suitable feedstocks include soybean, sunflower, cottonseed, rapeseed, palm oil, jatropha seed, tallow (animal fat) or even waste



countries contributed 4.89 million tons in the same year, where Germany leads the production followed by France and Italy. Germany produced 2.662 million tons of biodiesel which contributed about 42% of world total biodiesel production in 2006 (Board 2006). Currently, biodiesel is the main biofuel produced and consumed in the EU (EBB 2008). Biodiesel accounted for nearly 80% of EU biofuel production (Balat et al. 2008). There are 185 fully operational biodiesel plants currently available through out Europe, while many others are under constructions (Board 2006). In EU countries, taxes normally make up 50% or more to the retail price of diesel. However, the European Parliament has adopted a 90% tax exemption for biodiesel in 1994 to promote the public used of biodiesel (Balat et al. 2008).

The biofuel directive set an indicative target of 5.75 % replacement of conventional transport fossil fuels with biofuels by December 2010 (Transport 2004). In 2006 The European Parliament and the Council of the European Union encouraged the public to use biodiesel as an alternative especially for the transport sector. This is due to the fact that the transportation sector accounted for 21% of all CO<sub>2</sub> emissions worldwide in 2002. Currently, 95% of all energy for the transportation sector comes from fossil fuel (Kreith et al. 2007). The use of biodiesel in the transport sector may not be just to reduce the emissions but also to shrink the dependence upon imported energy and influence the fuel market for transport and hence to secure the energy supply for Europe.

Biodiesel is normally characterized by its properties of density, viscosity, low heating value, cetane number, cloud and pour points, characteristics of distillation, and

flash and combustion points. Pure RME or blends with ULSD may reduce the calorific value of the fuel thus may lead to reduced engine power and increased fuel consumption (Rakopoulos et al. 2006). The cetane numbers of RME and ULSD are about the same but the volatility of RME is slightly higher for RME which may affect the ignition delay and increase the amount of fuel for rapid combustion and boost the combustion temperature, thus producing higher NO<sub>x</sub> levels (Labeckas et al. 2006).

### **2.2.2 Performance and Emissions of Biodiesel as Fuel in ICE**

The future generation of diesel engines must also be able to work with alternative fuels such as biodiesel and alcohol blends due to shortage of fossil diesel and environmental concerns. The performance of biodiesel is slightly lower than that of diesel fuel, when the similar quantity of air and fuel is introduced into the cylinder (Senatore et al. 2000). There is almost no difference between the performance of RME and ULSD when the comparison is made on a similar relative equivalence ratio (Senatore et al. 2000). Much research has been conducted on a diesel engine operating with biodiesel as an alternative to the diesel fuel (Kawano et al. 2006; Chuepeng et al. 2007; Szybist et al. 2007; Tsolakis et al. 2007; Zheng et al. 2008; Tompkins et al. 2009; Yoon et al. 2009). Most of the researchers have agreed that biodiesel fuel could be used on its own or blended with conventional fossil fuel without having to make any modification to the standard diesel engine because biodiesel has properties similar to mineral diesel (Agarwal 2007; Tsolakis et al. 2007). Although the energy density of biodiesel is lower than that of diesel fuel, there is almost no difference between the performance of RME and ULSD fuelled engines if

the comparison is made for similar relative air/fuel ratios ( $\lambda$ ) used in the engines (Senatore et al. 2000).

A research conducted by Labeckas and Slavinskas on a four cylinder diesel engine operated with RME and fuel blend with mineral diesel. The engine was natural aspirated, water cooled with toroidal type compression-ignition combustion chamber in the piston heads. The test was conducted at five different engine speeds which were 1400rpm, 1600rpm, 1800rpm, 2000rpm and 2200rpm. They conclude that the diesel engine operating with RME consumed more fuel and low thermal efficiency relative to the diesel fuel (Labeckas et al. 2006). The diesel engine is normally equipped with turbocharger to enhance its capability to allow more air entrain the engine cylinder. The turbocharger in general is a pump driven by the energy of the exhaust gas flow. The exhaust gas flow through the turbine rotates the turbine, which is in turn used to drive the compressor. The pressure in a compressor is controlled by the waste gate to ensure that the pressure in the cylinder is not too high.

Alton et al. (Altõn et al. 2001) have conducted a study on a single cylinder diesel engine operating with various types of vegetable oil and their methyl esters. They worked with biodiesel fuels from different sources such as raw sunflower oil, raw cottonseed oil, raw soybean oil and their methyl esters, refined corn oil, distilled opium poppy oil and refined rapeseed oil. The results demonstrated that all fuels performed well on a single cylinder diesel engine with just 18% variations on maximum engine power and 10% variations of maximum engine torque.

The experimental work conducted on a diesel engine have proved that the combustion of biodiesel affect the volumetric efficiency of the AIS. This is due to the exhaust temperature of a diesel engine is highly related to the combustion event in engine cylinder and the type of fuel used in the engines. On the other hand, the volumetric efficiency is affected by the exhaust temperature (Balusamy et al. 2007).

Hasimoglu has conducted experimental work on a four cylinder turbo charged diesel engine operating with biodiesel and mineral diesel. He concluded that the volumetric efficiency of the engine was improved when the engine operated with biodiesel. The combustions of biodiesel emitted less heat due to lower of LCV and therefore lower exhaust gas temperature as compared to mineral diesel. Hence less heat transferred into the engine parts like intake manifold (Hasimoglu et al. 2008). This resulted to increase the volumetric efficiency of the air intake system. Kandasamy et. al have conducted a research on a single cylinder diesel engine operating with biodiesel and mineral diesel (Kandasamy et al. 2008). They concluded that the variation of volumetric efficiency is highly related to the exhaust temperature. The volumetric efficiency of the engine operating with biodiesel is lower due to the lower of exhaust gas temperature. The low-retained exhaust gas resulted to decrease the temperature of the air intake and vice versa.

### **2.3 Exhaust Emissions from the Combustion of Diesel and Biodiesel Fuel**

Transport for many years has had a significant effect upon air pollution since the inception of the internal combustion engine and especially after major commercialisation. The exhaust emissions generally result from the combustion of

fossil fuel in vehicle engines. Diesel fossil fuel is toxic and may cause long term adverse effects to the aquatic environment. In diesel engines, the pollutant formation processes are strongly dependent on the fuel distribution and how that distribution changes with time due to mixing (Heywood 1988). In general, previous results show that diesel engines fuelled with biodiesel emit a lower amount of unburned hydrocarbon (HC), particulate matter (PM) and carbon monoxide (CO) as compared to fossil diesel whereas NO<sub>x</sub> emissions are slightly increased (Senatore et al. 2000; Lapuerta et al. 2002; Labeckas et al. 2006; Horn et al. 2007; Szybist et al. 2007). Demirbas in his report suggested that the combustion of biodiesel alone provides over a 90% reduction in total unburned hydrocarbons (HC) and a 75-90% reduction in polycyclic aromatic hydrocarbons (PAHs) (Demirbas 2007). The results from previous experiments on biodiesel and their blends with ULSD in a single cylinder engine show that an increased proportion of biodiesel blend resulted in higher NO<sub>x</sub>, reduced smoke and increased brake specific fuel consumption (Chuepeng et al. 2007).

### **2.3.1 Oxides of Nitrogen**

The major pathway of NO<sub>x</sub> formation is thermal NO<sub>x</sub>, fuel NO<sub>x</sub> and prompt NO<sub>x</sub> (Heywood 1988; Kutz 2006). Thermal NO<sub>x</sub> refers to NO<sub>x</sub> produced during high temperature oxidation of the diatomic nitrogen found in combustion air and simply derived via the well-known Zeldovich mechanism (Baukal 2001). The formation rate is principally a function of temperature and the exposure period of nitrogen at that temperature (Horn et al. 2007; Keating 2007). The fuel NO<sub>x</sub> formed when the

combustion of fuel which contains organo-nitrogen compounds occur. During combustion, the nitrogen bound in the fuel is released as a free radical and eventually forms free  $N_2$ , or NO. High quality gaseous fuel has no organically bound nitrogen which produces an ignorable amount of NO<sub>x</sub> through this process. Conversely, fuel NO<sub>x</sub> is vital to revision for residual fuel oil, coal or waste fuel used that may contain a considerable amount of organically bound nitrogen (Baukal 2001).

The prompt NO<sub>x</sub> is attributed to the reaction of atmospheric nitrogen,  $N_2$ , with radicals such as C, CH, and  $CH_2$  fragments derived from fuel. The reaction took place in the earlier stage of combustion and produced fixed species of nitrogen such as nitrogen monohydride (NH), hydrogen cyanide (HCN), dihydrogen cyanide ( $H_2CN$ ) and cyano radical ( $CN^-$ ) which can oxidize to NO. Prompt NO<sub>x</sub> is commonly important in the low temperature combustion process.

NO<sub>x</sub> formed by the combustion of fuel in an internal combustion engine typically consists of nitric oxide (NO) and nitrogen dioxide (NO<sub>2</sub>) where the nitric oxide is dominant with a small amount of NO<sub>2</sub> (Heywood 1988). The formation of NO<sub>x</sub> is mostly from nitrogen in the air but some liquid fuels contain nitrogen such as  $NH_3$ , NC and HCN thus contributes higher potential on producing more NO<sub>x</sub> (Ganesan 2003). It is well known that this emission gas was highly dependent on post-combustion gas temperature, duration of gas exposure to this high temperature combustion and the species in post-combustion gases which are highly related to equivalent ratio,  $\phi$  (Keating 2007).

The higher NO<sub>x</sub> emissions for biodiesel as compared to ULSD can be related to the advance of injection timing which automatically occurs in engine cylinder with pump-in-line fuel systems to obtain higher volumetric delivery per stroke (Labeckas et al. 2006). Previous research has revealed that the NO<sub>x</sub> emissions as a function of the timing at which the maximum heat release rates and the maximum cylinder temperature occurred where the later the maximum heat release or maximum temperature occurs, the lower the NO<sub>x</sub> will be (Szybist et al. 2007). This fact is inline with the NO<sub>x</sub> formation process in that the earlier the maximum temperature is achieved, the longer the conditions are conducive for NO<sub>x</sub> formation (Szybist et al. 2007).

### **2.3.2 Carbon Monoxide**

Carbon monoxide (CO) emissions from IC engines are primarily controlled by the fuel/air equivalence ratio (Heywood 1988). The CO concentration in the exhaust tail pipe increases steadily with increasing equivalence ratio. Since CO emissions are closely related to fuel rich combustion, therefore, spark ignition engines produce a significant amount of CO emission compared with diesel engines. The diesel engine is often operating well on the lean side of stoichiometric ratio especially at low load. The concentration of CO for diesel engines encountered the range from just a few part per million at low load to around 3000ppm at high loads (Lilly 1984). Lower volumetric efficiency of air intake system resulted to increase the emission of CO in the exhaust gas. This is due to the incomplete combustion in engine cylinder.

### **2.3.3 Unburned hydrocarbons**

Hydrocarbons (HC) are grouped into categories based on their chemical structure such as paraffin (alkanes), olefins (alkenes), acetylenes (alkynes), or cyclic hydrocarbons (Bohac et al. 2001). Hydrocarbon emissions are the consequence of incomplete combustion of the hydrocarbon fuel. The compression ignition engine produces less HC as compared to SI engines due to its operation with an overall fuel-lean equivalence ratio (Ganesan 2003). The combustion of diesel fuel in compression ignition engines involved complex heterogeneous processes. Although the combustion of diesel fuel takes place in fuel-lean conditions, incomplete combustion still occurred. Due to non-homogeneity of the fuel mixture, some local spots in the combustion chamber will be too lean to completely combust (Ganesan 2003). The amount of unburned HC resulting from this overlean regions is dependent on the amount of fuel injected during the ignition delay, the mixing rate with air during this period, and the extent to which prevailing cylinder conditions are conducive to autoignition (Heywood 1988). HC emissions are also reported as sensitive to engine temperature where these emissions decrease as the engine temperature increase (Heywood 1988). Fuel also has an effect on HC emissions where the fuel with lower end boiling point produces higher HC (Lilly 1984). CI engines also produce HC emissions from wall deposit absorption, oil film absorption and crevice volume (Ganesan 2003).

#### **2.3.4 Particulate matter**

Particulate matter is defined as any material other than water, in the exhaust of an internal combustion engine which can be filtered after dilution with ambient air (Lilly 1984). Most of the PM is generated from incomplete combustion of diesel fuel but some comes from lubricating oil components which vaporize and then react during combustion (Heywood 1988). The individual structure of PM is principally clusters of many small spheres or spherules of carbon. The PM emissions consist of absorbed and condensed high molecular weight organic compounds which include unburned hydrocarbons, oxygenated hydrocarbons (ketones, esters, ethers, organic acids) and polynuclear aromatic hydrocarbons (Heywood 1988).

The combustion of biodiesel produces less PM as compared to fossil diesel. The reductions of PM could be explained by the increase in oxygen content in the fuel which contributes to complete fuel oxidation even in locally fuel rich zones, and by the lower final boiling point which guarantees a complete evaporation of the liquid fuel (Lapuerta et al. 2002).

## 2.4 Summary

In the presented chapter, the general evolution of an AIS is discussed. The improvement of an AIS is not just to increase the engine performance, but also helpful to improve combustion quality in order to meet the requirement of emission legislation. The AIS of Land Rover vehicles is designed to fulfil the requirement of wading performances. Therefore, the intake grill is located at the side of the vehicle. There is no research available in the literature on this particular air induction grill, especially the effect of negative pressure on the induction grill surface. Therefore, a further investigation into this phenomenon has been carried out within the presented thesis. Some researchers have successfully used a steady flow test rig to improve the AIS but some researchers used simulation software such as Ricardo WAVE and Fluent to investigate the flow behaviour on the AIS.

From the literature review, it is found that the experimental work on a diesel engine is very important to study the effect of fuel specifically RME on to the performance of air induction system. This is very significant for the new design of diesel engine which equipped with modern technologies such as VGT turbocharger, EGR system and common-rail fuel injection system. The combustion of biodiesel in engine cylinder produces a lower of exhaust temperature resulted to alter the performance of air induction system.

## **CHAPTER 3**

### **RESEARCH METHODOLOGY**

This chapter is mainly concerned with both simulation and experimental solution approach to investigate the performance characteristic of an AIS. The first half of the chapter deals with the set-up of the boundary conditions of the geometry of the AIS provided by Jaguar Land Rover, solver selection and post-processing techniques to predict the flow behaviour of the AIS. The second half of the chapter deals with the experimental set-up for the steady flow test and engine test with biodiesel fuel. The selection of apparatus and measuring devices used in the test rig are discussed in detail.

#### **3.1 Setup of CFD Models**

Computational fluid dynamic is a numerical tool for simulating the complicated fluid flow, heat transfer and chemical reactions in any fluid flow domain. The first generation of CFD solutions appeared in the 1950s stimulated by the simultaneous advent of high performance computer systems. Recently, this tool has been widely used in all flow problems due to many factors. One obvious reason is the dramatic increase in computer power that is available at affordable cost. In fact, the

results of modelling can be viewed quickly and easily compared to the time and cost required by the experimental work. There are many commercial CFD codes such as FLUENT, CFX and Star-CD. These commercial codes have been made as easy as possible to minimize the time and cost of simulation work.

### 3.1.1 Governing Equations

The substantial derivative is mathematical notation that is important to derive the governing equation in fluid dynamics. The substantial derivative operator in vector notation can be summarized as follows;

$$\frac{D}{Dt} = \frac{\partial}{\partial t} + \text{div}\vec{V} \quad (3.1)$$

Where,

$$\text{div}\vec{V} = \frac{\partial u}{\partial x} + \frac{\partial v}{\partial y} + \frac{\partial w}{\partial z} \quad (3.2)$$

$D/Dt$  is the substantial derivative which is physically the time rate of change following a moving fluid element. The symbol of  $u$ ,  $v$  and  $w$  is the velocity in the direction of axis  $x$ ,  $y$  and  $z$  respectively.  $\partial/\partial t$  is called the local derivative, which is physically the time rate of change at a fixed point. The term  $\text{div}\vec{V}$  is called the convective derivative, which is physically the time of change due to the movement of the fluid element from one location to another in the flow field where the flow properties are spatially different. This particle derivative will be used in the rest of the chapter to present the Navier-Stoke equations in conservative form.

The conservation of fluid mass in a control volume is derived as the continuity equation. According to the continuity equation, the rate of increase of fluid mass within a control volume is equal to the net rate of flow of mass into the control volume (Douglas 1995). The equation of continuity can be expressed in the Cartesian tensor conservative form as:

$$\frac{\partial \rho}{\partial t} + \text{div}(\rho \vec{V}) = 0 \quad (3.3)$$

$\rho$  is the density and  $\vec{V}$  is the vector velocity of the fluid. Equation (3.3) is the unsteady, three-dimensional mass conservation or continuity equation at a point in a compressible fluid. The first term describes the rate of change in time of the density. The second term describes the net flow of mass out of the element across its boundaries and is called the convective term (Versteeg et al. 1995). To simplify the simulation process, the simulation for an AIS is simulate under incompressible fluid flow where the divergence of the velocity is assumed to be zero, the density of air is constant and equation (3.3) becomes

$$\text{div} \vec{V} = 0 \quad (3.4)$$

or in complete Cartesian tensor form,

$$\frac{\partial u}{\partial x} + \frac{\partial v}{\partial y} + \frac{\partial w}{\partial z} = 0 \quad (3.5)$$

The second law describes the dynamics of fluid flow results in the momentum equations. This equation is derived by applying Newton's second law of motion to the fluid control volume. Newton's second law states that the rate of change of

momentum of a fluid particle equals the sum of the forces on the particle. For Newtonian fluid, this equation is known as Navier-Stoke equation

$$\rho \frac{Du}{Dt} = \frac{\partial(-p + \tau_{xx})}{\partial x} + \frac{\partial \tau_{yx}}{\partial y} + \frac{\partial \tau_{zx}}{\partial z} + S_{Mx} \quad (3.6)$$

$$\rho \frac{Dv}{Dt} = \frac{\partial \tau_{xy}}{\partial x} + \frac{\partial(-p + \tau_{yy})}{\partial y} + \frac{\partial \tau_{zy}}{\partial z} + S_{My} \quad (3.7)$$

$$\rho \frac{Dw}{Dt} = \frac{\partial \tau_{xz}}{\partial x} + \frac{\partial \tau_{yz}}{\partial y} + \frac{\partial(-p + \tau_{zz})}{\partial z} + S_{Mz} \quad (3.8)$$

The right hand side terms of equations 3.6, 3.7 and 3.8 describe the rate of increase of x, y and z-momentum per unit volume of fluid particle respectively. The first, second and third terms describe the effect of surface forces which are pressure and viscous forces. The source terms  $S_{Mx}$ ,  $S_{My}$  and  $S_{Mz}$  in equation 3.6, 3.7 and 3.8 include contributions due to body forces. The examples of body forces include gravity, centrifugal, electromagnetic and coriolis force. The simulation of an AIS is only consider gravity forces as describe above, therefore

$$S_{Mx} = 0 \quad (3.9)$$

$$S_{My} = 0 \quad (3.10)$$

$$S_{Mz} = -\rho g \quad (3.11)$$

The energy equation, which is derived from the first law of thermodynamics states that the rate of change of energy of a fluid particle is equal to the rate of heat

addition to the fluid particle plus the rate of work done on the particle, is given in its most short form as follows:

$$\rho \frac{DE}{Dt} = -div(p\vec{V}) + \left[ \begin{array}{l} \frac{\partial(u\tau_{xx})}{\partial x} + \frac{\partial(u\tau_{yx})}{\partial y} + \frac{\partial(u\tau_{zx})}{\partial z} + \\ \frac{\partial(v\tau_{xy})}{\partial x} + \frac{\partial(v\tau_{yy})}{\partial y} + \frac{\partial(v\tau_{zy})}{\partial z} + \\ \frac{\partial(w\tau_{xz})}{\partial x} + \frac{\partial(w\tau_{yz})}{\partial y} + \frac{\partial(w\tau_{zz})}{\partial z} \end{array} \right] + div\vec{q} + S_E \quad (3.12)$$

Where

$$-div\vec{q} = -\frac{\partial q_x}{\partial x} - \frac{\partial q_y}{\partial y} - \frac{\partial q_z}{\partial z} \quad (3.13)$$

and

$$q_x = -k \frac{\partial T}{\partial x} \quad (3.14)$$

$$q_y = -k \frac{\partial T}{\partial y} \quad (3.15)$$

$$q_z = -k \frac{\partial T}{\partial z} \quad (3.16)$$

The term on the left hand side of equation (3.12) describes the rate of increase of energy of a fluid particle per unit volume. The first term on the right hand side of equation (3.12) describes the total rate of work done on the fluid particle by surface stress. The  $-div\vec{q}$  physically means the rate of heat addition to the fluid particle due to

heat conduction. The final form of equation (3.12),  $S_E$  defines a potential energy changes as a source term.

### **3.1.2 Turbulence Model**

Virtually all flows of practical engineering interest are turbulent (Wilcox 1994). Turbulent flows are extremely complex where the flows characterized by the fluctuating of velocity fields. The fluctuations of the velocity field mix transported quantities such as momentum, energy, and species concentration. As a consequence these transported quantities fluctuate simultaneously. Turbulent flow is a fluid behaviour of chaotic, stochastic property changes. This includes low momentum diffusion, high momentum convection, and rapid deviation of pressure and velocity in space and time. The interaction is very complex because it is rotational, fully three dimensional and time dependent.

Turbulence modelling is the area of physical modelling where a simpler mathematical model than the full time dependent Navier-Stokes Equations is used to forecast the effects of turbulence. There are various mathematical models available nowadays to solve the turbulent flow. However, there is no single turbulence model collectively accepted for all turbulence flow problems. The choice of turbulence model will depend on considerations such as the physics encompassed in the flow, the established practice for a specific class of problem, the level of accuracy required, the available computational resources, and the amount of time available for the simulation (Fluent 2005). Therefore, understanding on the specific turbulence problems such as

capabilities and limitations of the various options is essential to certify that the turbulence model chosen is the best.

The simulation works on the AIS have been conducted on standard turbulence k- $\epsilon$  code on FLUENT 6.2. The software runs on The University of Birmingham servers. The computations have been carried out using only one processor of a single node of a 6-node HP J-Class load sharing server. Each node has a minimum of 8 GB RAM and 2 CPUs which are PA-RISC chips running at 750 MHz. The J-Class server is a J6700 model connected via a fibre optics channel to a virtual array (VA) storage subsystem. The VA is mounted via a clustered NAS 9000 (MS Windows based) system (Mahrous 2008).

The k- $\epsilon$  model is widely used to solve turbulence flow problems. The model is developed by two additional transport-equations to represent the turbulence properties of the flow. The model is proved to solve the free shear layer flows with relatively small pressure gradient. The model is good for wall-bounded and internal flow especially when the mean pressure gradient is small. The accuracy of the calculation made by k- $\epsilon$  model is well accepted. The flow inside the modern AIS is complex and mostly turbulent at all engine speeds as well as for all manifold design and geometry. It involves a complicated combination of small-scale and large-scale flow structures such as turbulent shear layers, jets, and boundary layers. The standard k- $\epsilon$  code by FLUENT is successfully used by many researcher to visualize the flow characteristic of different kind of AIS (Safari et al. 2003; Devi et al. 2004; Ling et al. 2006; Siqueira et al. 2006).

The optimisation of an AIS of a turbo charge inter-cooled diesel engine have been conducted by Devi et al by using k-ε model (Devi et al. 2004). The good visualization of air flow on the AIS provided the opportunity for the designer to improve the standard shape of the AIS. The standard AIS have been improved by modifying the sharp corner on several parts of the air intake manifold and resulted in lowering the pressure drop of the AIS. Ling and Tun (2006) have successfully used the turbulence k-ε model to visualize the unsteady flow of a non symmetrical intake manifold (Ling et al. 2006). The research is focused on the effect of the venturi and the bell mouths shape at the entrance of the manifold runners. Joshi and his colleagues worked with the standard k-ε turbulence model by FLUENT to reduce pressure drop on an AIS. The results show the good correlation between numerical and experimental (Joshi et al. 2008). Safari (2003) has effectively used standard the k-ε model on 3D CFD analysis to optimise the intake manifold (Safari et al. 2003). The simulations have been conducted on unsteady and steady state conditions. The steady state simulations are compared with flow bench rig data for validation. It is proved that the standard k-ε turbulence model gives a good agreement between simulation and experiment results from steady flow test bench. Therefore, the standard k-ε model is the good turbulence model to simulate the AIS due to it simplicity and robustness whilst still providing good results.

The turbulent kinetic energy,  $k$ , and its dissipation rate,  $\varepsilon$ , are calculated from the following transport equations (Versteeg et al. 1995):

$$\rho \frac{Dk}{Dt} = \frac{\partial}{\partial x_i} \left[ \left( \mu + \frac{\mu_t}{\sigma_k} \right) \frac{\partial k}{\partial x_i} \right] + G_k + G_b - \rho \varepsilon - Y_M \quad (3.17)$$

$$\rho \frac{D\varepsilon}{Dt} = \frac{\partial}{\partial x_i} \left[ \left( \mu + \frac{\mu_t}{\sigma_\varepsilon} \right) \frac{\partial \varepsilon}{\partial x_i} \right] + C_{1\varepsilon} \frac{\varepsilon}{k} (G_k + C_{3\varepsilon} G_b) - C_{2\varepsilon} \rho \frac{\varepsilon^2}{k} \quad (3.18)$$

The model constants  $C_{1\varepsilon}$ ,  $C_{2\varepsilon}$ ,  $C_\mu$ ,  $\sigma_k$  and  $\sigma_\varepsilon$  have the following default values:

$$C_{1\varepsilon} = 1.44, \quad C_{2\varepsilon} = 1.92, \quad C_\mu = 0.09, \quad \sigma_k = 1.0, \quad \sigma_\varepsilon = 1.3$$

These default values have been determined from experiments for fundamental turbulent shear flows and they work fairly well for a wide range of wall-bounded and free shear flows (Fluent 2005).

### 3.1.3 Modelling Approach

The geometry of the air intake system of a Land Rover Freelander was used in the modeling approach. The simulation was carried out using the finite volume commercial CFD code FLUENT, release 6.3. In order to have a better relation between pressure and velocity, the SIMPLE algorithm was chosen for the whole series of simulations. The SIMPLE algorithm, which stands for Semi-Implicit Method for Pressure-Linked Equation, is widely accepted as the most relevant algorithm for such case study (Ganesan et al. 2004). The algorithm uses a relationship between velocity and pressure corrections to enforce mass conservation and to obtain the pressure field (Fluent 2005). The method is illustrated by considering the two-dimensional laminar steady flow equations in Cartesian coordinates (Douglas 1995). Convergence of solutions is judged by monitoring the normalized residuals. In the current study the simulation stops right after a convergence factor of  $10^{-3}$  is achieved for residual source

of all variables. Figure 3.2 shows the simulation flow chart for the numerical analysis using Fluent 6.3

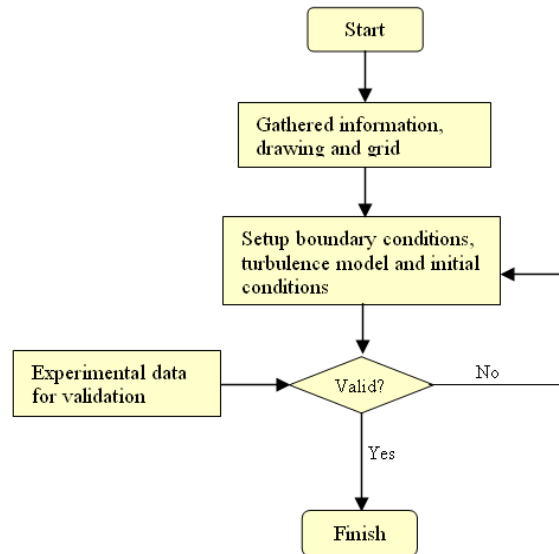


Figure 3.1 Simulation flow chart

### 3.1.4 Grid Generations

The geometry of the air intake system of the Freelander was used to computationally study the flow behavior. Figure 3.2 shows the geometry model of the intake manifold of the Freelander. The 3D geometry and mesh files were prepared by Land Rover where it was kept as simple as possible to minimize the simulation errors. In order to reduce simulation time, the geometry was prepared in a separate CAD package and then imported to the pre-processor environment for meshing. Most of the trivial geometry details that are not important from a fluid flow point of view such as blends, small fillets, stiffener and steps have been ignored.

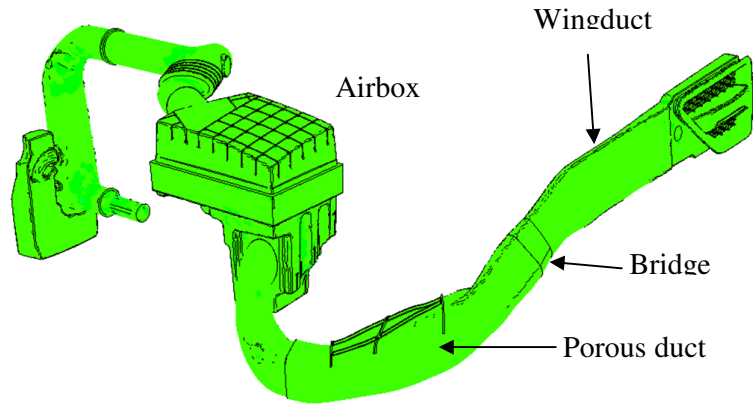


Figure 3.2 Three dimensional geometry of the Freelander air intake system.

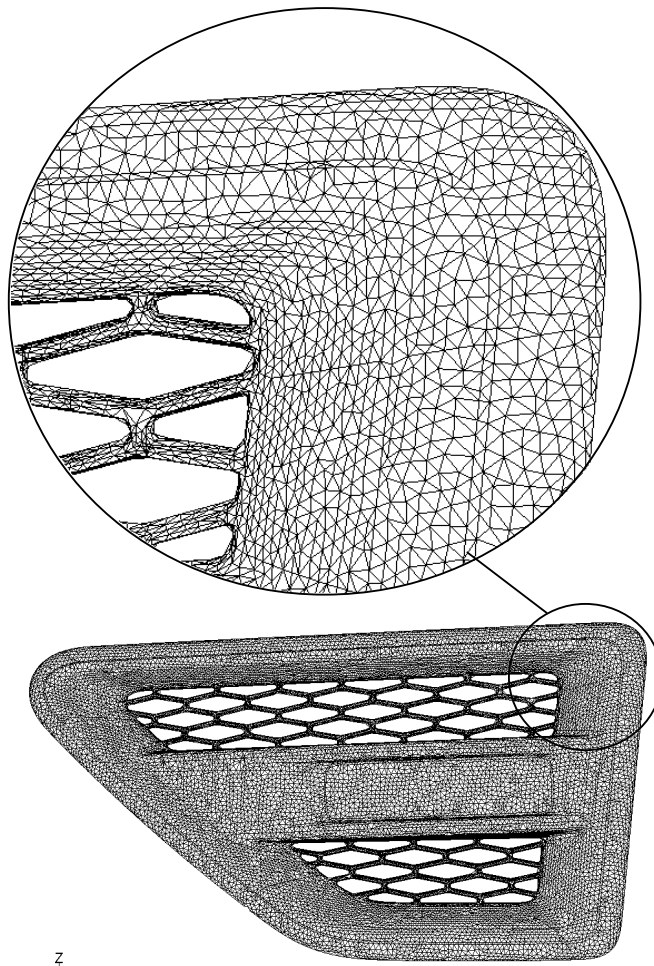


Figure 3.3 Close view of Freelander intake grill

The mesh was generated using the Tet-hybrid scheme and comprised more tetrahedral mesh elements than hexahedral, pyramid and wedges elements. The mesh size is known to influence the accuracy of the results, and consists of 2,234,099 fine cells. The grid sizes are non-uniform and a fine mesh was applied in critical regions of the domain where large gradients in flow were expected. Likewise coarser grids were applied to regions where the variations are relatively very small. Figure 3.3 shows the closed-up view of air intake grill. It is clearly seen that the grid is generated by tetrahedral mesh elements with the smaller grid at critical corners.

In order to assess high accuracy of the model, two different grids named as Grid 1 and Grid 2 were generated to simulate the velocity profile in the air intake system. The Grid 1 and Grid 2 are consists of 1,563,869 cells and 2,234,099 cells respectively.

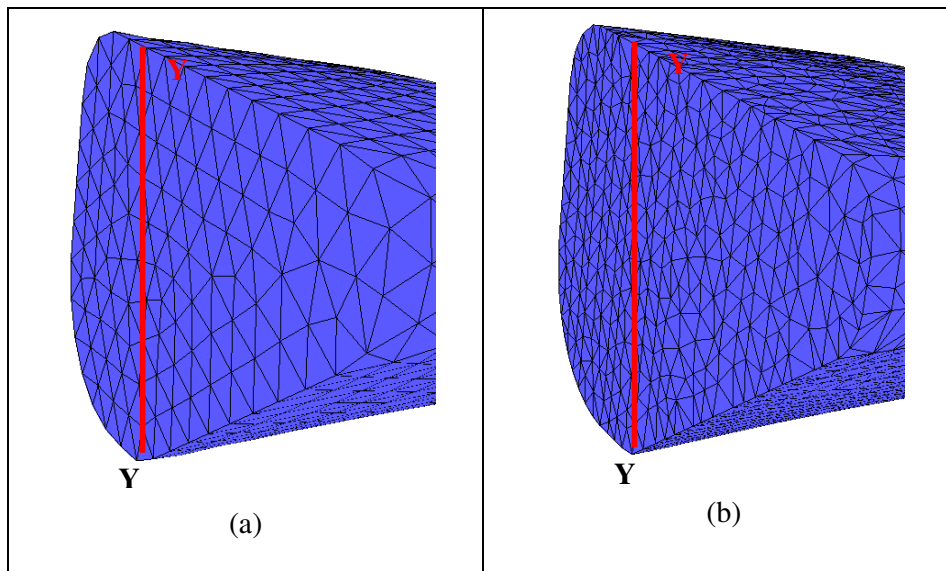


Figure 3.4(a) and 3.4(b) Two different grid with y-y' axis marked on the cross section of the 'bridge'.

The velocity magnitude is measured at the bridge between wingduct and porous duct as depicted in Figure 3.2. The cross-section on the bridge area marked as Y-Y' axis is generated in the model to compare the velocity magnitude in this axis. Figure 3.4(a) and 3.4(b) show the different of the grid size between Grid 1 and Grid 2. Figure 3.5 shows the velocity profiles of the air flow in the Y-Y' axis. The result shows that the velocity profile on the Grid 2 is smoother and produces a better effect on the wall surface. Figure 3.5 also shows that the maximum velocity of the Grid 1 is 9.5% higher than the Grid 2. The significant different between both velocity profiles are clearly seen in the region of 5 mm from the wall surface. From the above results, Grid 2 was chosen to be used for the rest of the simulation study.

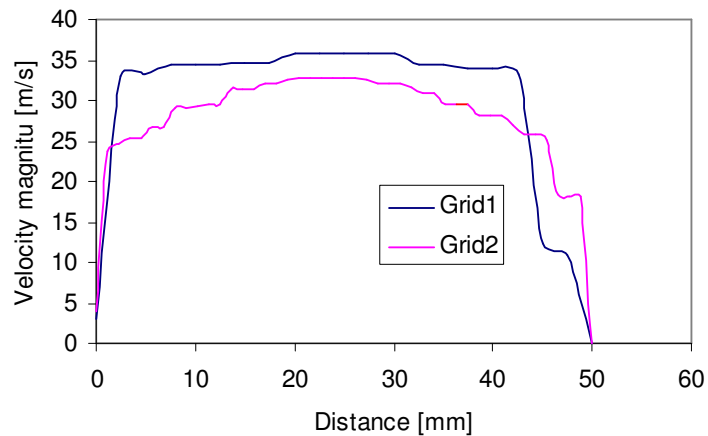


Figure 3.5 shows the velocity magnitude at Y-Y' axis for Grid 1 and Grid 2.

## **3.2 Experimental System and Techniques**

The experimental works cover both steady flow test and V6 diesel engine test. The experiment was designed to study the effect of the AIS geometry and its related properties to engine performance under steady state conditions. The engine is used to operate with biodiesel fuel and the comparison has been made with the performance of the air intake system when the engine operated with ULSD.

### **3.2.1 Steady Flow Test Rig**

#### **3.2.1.1 Purpose of Steady Flow Testing**

Steady flow testing is widely used all over the world by car manufacturers to improve the quality of flow through components such as the intake system and the cylinder-head. The theory, along with the application, is derived by AVL and Ricardo where the discussion detail and comparison between these two approaches can be found in the literature (Xu 2001). Much of the attention is focused on increasing volumetric efficiency for achieving high torque and power. Figure 3.6 shows the commercially available steady flow test bench by SuperFlow and Cussons. The SF-1020 can be operated at 65 IWG with the maximum flow of 1700 m<sup>3</sup>/h whereas; the Cussons model P7305/SP can be operated at 61 IWG with 720 m<sup>3</sup>/h of maximum flow rate. Essentially it consists of a centrifugal fan, pressure box, air filter, valves, pipes and measurement devices such as a swirl meter, flow meter, thermometer and manometer. Advanced measurement apparatus such as PIV could be used to improve understanding on air flow properties such as velocity vector and magnitude.

Measurements of pressure drop along the air intake system could be performed by the use of a standard test bed. These measurements are carried out on complete air intake system together with the cylinder head and ports. This is particularly important for direct injection engines where the port is shaped to generate the required degree of swirl within the cylinder (Lilly 1984). However for the purpose of the current study, where the research is focused on the pressure drop at the intake duct and grill, it is not compulsory to test the intake duct with a cylinder head.

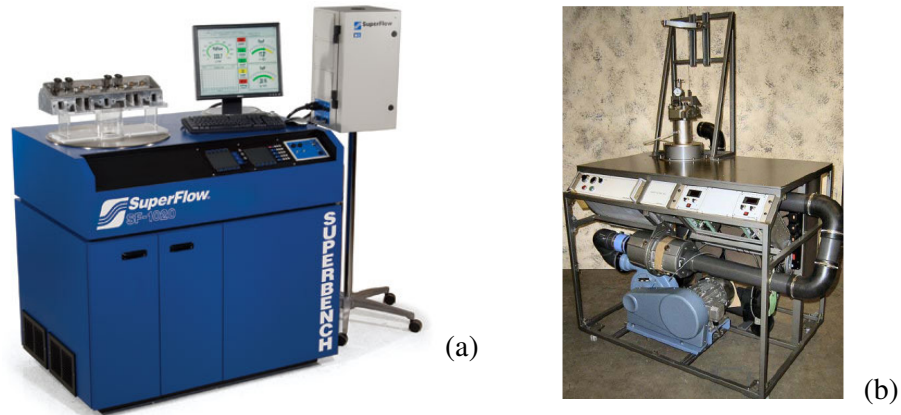


Figure 3.6 Commercial steady flow test bench (a) SuperFlow (Superflow 2008), (b) Cussons (Cussons 2008)

### 3.2.1.2 Design and Setup of Steady Flow Test Bench

The steady flow test bench used in this study was designed, fabricated and tested in the Thermo-Fluid Laboratory at Birmingham University. Two commercial standard steady flow test benches have been used as the bench mark; SF-1020 by SuperFlow Ltd and P7305/SP by Cussons Ltd. The specification details of SF-1020

and P7305/SP can be found from Appendix A. These two standard steady flow benches have been used extensively in the development of air intake manifolds throughout the world. Figure 3.7 shows the schematic diagram of the steady flow bench designed in the laboratory. The pressure is recorded at 4 different locations which are at test plenum (P1), before an orifice plate (P2), after an orifice plate (P3) and in the plenum chamber (P4). The temperature is measured at test plenum (T1) and plenum chamber (T4).

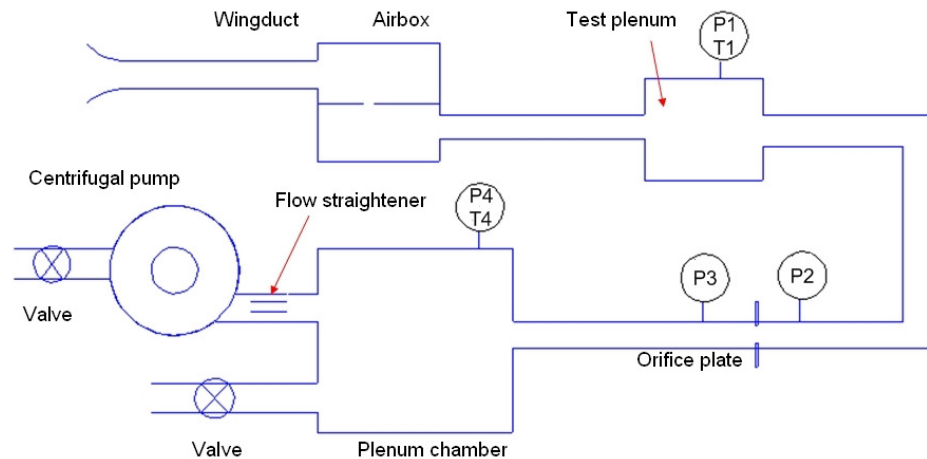


Figure 3.7 Steady flow test bench.

The centrifugal vacuum pump is used in the test rig to generate a high pressure difference in the plenum chamber of the test bench. The vacuum pump standard model 587/2 was supplied by SECOMAK Ltd in Hertfordshire. The pump was operated on 400 Volts, 3-phase 50Hz electrical sources with the power rating of 5.5 kW. The vacuum pump is originally supplied with inlet silencer. However, the inlet silencer was removed to simplify the fabrication of the test rig.

The pump generated 90 dB noise levels during the operation when measured 1 m from the pump. Figure 3.8 shows the performance curve for the standard vacuum pump model 587/2 as provided by the manufacturer. It shows that the pump could possibly deliver a maximum volume rate of around 1500m<sup>3</sup>/h at 29 inch water gauge (IWG). The maximum pressure of around 40 IWG can be achieved at 500 m<sup>3</sup>/h of volume flow rate.

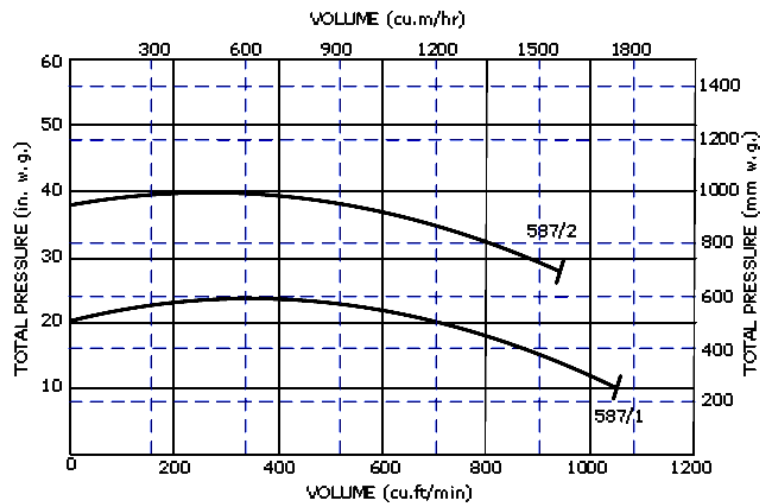


Figure 3.8 Performance curve for SECOMAK pump model 587/2

The pressure drop across the intake duct was controlled by a three-inch butterfly valve. The valve is attached between two flanges in the plenum chamber. This plenum chamber is created from an empty lubricant oil drum. The drum which has 50 litre of volume is used to eliminate swirl flow and pressure pulse generated from the centrifugal pump.

A flow straightener was used to ensure that the flow was uniform before passing through the vacuum pump. This is extremely important to make sure that the pulsation and rotation of fluid in the pump blades does not affect the flow uniformity

upstream of the pump. The flow straightener was produced from the 3 inch thick commercial aluminium honeycomb. It is located between the centrifugal pump and the plenum chamber as clearly shown by the schematic diagram of the test bench in Figure 3.7.

This experiment is intended to study the effect of negative flow at the intake grill due to the cross flow in the surface of the intake grill. This condition occurs during the standard operations of the AIS under normal driving conditions at a specific vehicle speed. Therefore, the intake grill was fixed into the test section of a wind tunnel in the Thermo-Fluid Laboratory to simulate the cross flow in the intake grill. The outlet of the AIS was fitted to the steady flow test bench. The experiments were conducted over the whole air intake system. Figure 3.9 shows the air intake grill which was attached into the test section of wind tunnel. The test section of the wind tunnel and the specification details are as depicted in Table 3.1.



Figure 3.9 Photograph of the Freelander air intake grill.

Table 3.1 Specification of wind tunnel

Specification	Details
Test section	147x147x600 mm
Turbine power rating (each)	11 kW
Contraction area ratio	3 : 1
Flow straightener device	Aluminum honeycomb 3mm thickness, 3 mm cell size.
Wind speed	32.6 m/s (single turbine) 48.5 m/s (duo turbine)

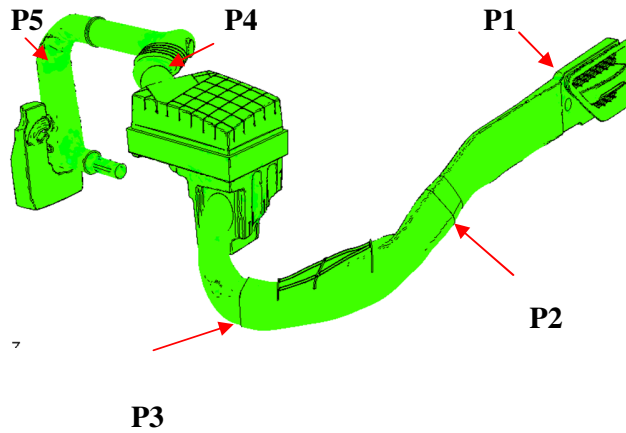


Figure 3.10 Pressure measurement locations on intake duct

Measurements of pressure drop are taken at five different locations as shown in Figure 3.10. The vacuum pump was used to generate pressure drop on the intake duct and the mass flow rate was carefully controlled by the valve. Steady flow tests are conducted in steady state conditions where the air flow rate and pressure drop is constant. Therefore, the measurement of pressure drop and temperature are taken with a standard manometer U-tube and glass thermometer respectively. The manometer U-tube was supplied by Airflow Instrument Ltd model Type SJ-39 with the maximum

pressure reading of up to 10kPa (40.1 IWG). The pressure drop between up-stream and down-stream of the orifice plate was measured with an incline manometer by Airflow Instruments Ltd. The standard incline manometer model Type 504 was chosen due to the requirement of an accurate reading on the pressure difference of the orifice plate. This manometer is very sensitive to small pressure differences with a scale length of 250 mm, covering the range from 0 to 500 Pascal. Figure 3.11 shows the photograph of the incline manometer by Airflow Instruments Ltd.



Figure 3.11 Incline manometer model Type 504 by Airflow Instrument Ltd.

The standard orifice plate was supplied by Roxspur Measurement and Control Ltd with all technical specifications such as physical dimensions and flow coefficient provided by the manufacturer. The orifice plate was sited between two BS10 flanges as recommended by the manufacturer. Figure 3.12 shows the photograph of the orifice plate before the installation. The orifice plate was made of carbon steel material with a three inch nominal diameter as equal to the overall galvanized pipe diameter which was used in the test bench.



Figure 3.12 Photograph of the orifice plate by Roxspur Measurement & Instrumentation Ltd

When the construction of the steady flow bench was completed, the test bench was operated and tested for one hour without any test sample to comply with the safety regulations in the Thermo-Fluid Laboratory. Figure 3.13 shows a complete assembly of the steady flow test bench.



Figure 3.13 Photograph of steady flow test bench

### 3.2.2 The Engine Performance Characteristic

The performances of diesel engines are governed by a number of engine parameters such as engine geometry, air charging etc. The engine torque as an output parameter from the engine is normally measured with a dynamometer. The engine brake power  $P_b$  (W) is calculated later by the formula given in Equation 3.19.

$$P_b = 2\pi NT_b \quad (3.19)$$

where  $N$  is the engine speed in revolution per second,  $T_b$  is the brake torque measure by dynamometer in N.m.

The in-cylinder pressure data measured from the experimental work is used to calculate the work transfer from the gas to the piston. The in-cylinder pressure and corresponding cylinder volume throughout the engine cycle is normally plotted on  $p$ - $V$  diagram as shown in Figure 3.14

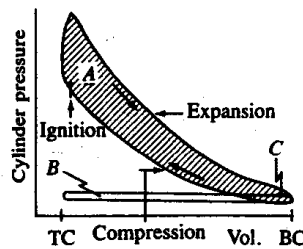


Figure 3.14 Typical  $p$ - $V$  diagram of a four-stroke cycle (Heywood 1988).

The indicated work per cycle is obtained by integrating around the curve on a  $p$ - $V$  diagram and can be expressed as in Equation 3.20.

$$W = \oint pdV \quad (3.20)$$

Mean effective pressure is widely used to measure relative engine performance which can be obtained by dividing the work done per cycle by the cylinder volume displaced per cycle (Heywood 1988). The calculation of IMEP from the experimental works can be expressed by Equation 3.21:

$$\text{IMEP} = \frac{\text{Indicated work per cycle}}{\text{Displaced volume}} = \frac{\oint p dV}{V_d} \quad (3.21)$$

where  $p$  is cylinder pressure and  $V$  is equivalent cylinder volume at in-cylinder pressure,  $p$ .

The in-cylinder pressure against crank the angle degree over the compression and expansion strokes of the engine cycle is very useful to obtain quantitative information on the progress of combustion (Heywood 1988). The progress of combustion analysis is conducted on LabVIEW based software which was originally developed by Professor Wyszynski. The code was extensively used by many researchers previously for the combustion analysis on single cylinder as well as multi cylinder engines (Chuepeng et al. 2007; Tsolakis et al. 2007; Chuepeng 2008). The LabVIEW code required in-cylinder pressure and the consecutive cylinder volume. The in-cylinder pressure data is recorded in the engine cylinder by the National Instrument data acquisition card as a text file. The file is transformed later to an Excel file before it will be used by LabVIEW code. The output parameters include in-cylinder peak pressure ( $P_{\max}$ ), indicated mean effective pressure (IMEP), coefficient of variation (COV) of  $P_{\max}$ , and COV of IMEP.

The in-cylinder pressure is finally used to analyse the detail of heat release rate and mass fraction burn. The heat release rate  $dQ/d\theta$  is calculated using the equation (Heywood 1988).

$$\frac{dQ}{d\theta} = \frac{\gamma}{\gamma-1} p \frac{dV}{d\theta} + \frac{1}{\gamma-1} V \frac{dp}{d\theta} \quad (3.22)$$

where  $\gamma$  is the ratio of specific heats which are calculated from the actual  $p$ - $V$  diagram ( $c_p/c_v$ ),  $V$  is the instantaneous volume of the engine cylinder and  $p$  is the instantaneous cylinder pressure. The brake specific fuel consumption (bsfc, in g/kWh) is the mass fuel flow rate per unit power output of the engine. The calculation of bsfc is given by Equation 3.23:

$$\text{bsfc} = \frac{\dot{m}_f}{P_b} \quad (3.23)$$

The thermal efficiency is a dimensionless number to measure the performance of the engines. The engine thermal efficiency  $\eta_{th}$  is given by:

$$\eta_{th} (\%) = \frac{P_b}{\dot{m}_f (\text{LHV})} \times 100 \quad (3.24)$$

where  $\dot{m}_f$  is the fuel mass flow rate per cycle,  $P_b$  is the brake power.

The volumetric efficiency is a parameter used to measure the effectiveness of an engine's induction system. It is defined as the ratio of the actual volume flow rate of air into the intake system divided by the rate which volume is displaced by the piston (Heywood 1988).

$$\eta_v = \frac{2\dot{m}_a}{\rho_{a,i}V_dN} \quad (3.25)$$

Where,  $\dot{m}_a$  is air mass flow rate (kg/s),  $\rho_{a,i}$  is the air density (kg/m<sup>3</sup>)  $V_d$  is displacement volume of the engine (m<sup>3</sup>) and  $N$  is the engine speed (revolution per second). Equivalently, the volumetric efficiency can also be defined as the ratio of the actual mass flow per cycle to the mass calculated from the product of the swept volume and an arbitrary reference density (Smith et al. 1999).

Most modern diesel engines are equipped with EGR systems where the fraction of the engine exhaust gases is recycled to the intake to dilute the fresh air mixture for control of NOx emissions (Heywood 1988). The volumetric percentage of the EGR rate are calculated by

$$\text{EGR (vol. \%)} = \frac{\dot{V}_{a,i} - \dot{V}_m}{\dot{V}_{a,i}} \times 100 \quad (3.26)$$

where  $\dot{V}_{a,i}$  is the measured intake air flow rates and  $\dot{V}_m$  is the mass flow rate measure of the mixture between fresh air and exhaust gas.

## 3.2.2 Diesel Engine Test Setup

### 3.2.2.1 Engine Test Bench

The experimental work was performed on a Jaguar V6 diesel engine to investigate the contributions of AIS onto the engine performance and emission when it

is used to operate with biodiesel and mineral diesel. The engine was water-cooled, direct injection and equipped with twin variable geometry turbine (VGT) turbochargers and an exhaust gas recirculation (EGR) system. Details of the engine are described in Table 3.2. Figure 3.15 shows the photograph of the test engine used in this study.

Table 3.2 Specification of test engine

Engine Specification	Details
Type	V6 Twin Turbo
Engine firing order	1 4 2 5 3 6
Injection System	Common rail
Devices	Cooled EGR
Bore x Stroke	81.0mm x 88.0mm
Displacement	2721 cc
Compression ratio	17.3
Injector type	Piezo actuator injector
Injection cone angle	156°
Injection nozzle hole	6
Injector nozzle diameter	0.1 mm
Fuel injection pressure (Max @4000rpm)	1600 bar
Maximum of injection pressure @4000rpm	1600 bar
Maximum power @4000rpm	150.6 kW
Maximum torque @1900rpm	435 Nm



Figure 3.15 Photograph of test engine

The engine operating conditions are based on the NEDC (New European Driving Cycle). The experiment was conducted under a controlled environment. Air temperature was controlled between 23°C and 27°C and the relative humidity was measured by a RH sensor and recorded by a Windows based PC. Air inlet temperature and atmospheric pressure were measured and calculated to comply with the test validity as explained in Directive 1999/96/EC, 2000 (2000).

An eddy-current dynamometer model W230 with series S2000 control system was used to load the engine. The universal joint prop-shaft was used to transfer the energy from the engine to the dynamometer. The specification details of the dynamometer unit is listed in Table 3.3

Table 3.3 Specifications of dynamometer

Manufacturer	DSG Ltd
Model	W230
Maximum speed	7500 rpm
Rated torque	750 Nm
Power	230 kW
Moment of inertia	0.53 kgm <sup>2</sup>
Weight	480 kg

The dynamometer was controlled by a standard dynamometer controller. The controller is located in the control room where the temperature was controlled at room temperature. Tap water was used to cool down the temperature of dynamometer when it was operated. A standard three inch cooper tube was connected to the dynamometer to supply sufficient water flow. Figure 3.16 shows the closed-up picture of the dynamometer and the controller.



Figure 3.16 Dynamometer and controller system

### 3.2.3.2 Engine Fuel System

The test engine consists of two stainless steel fuel tanks for RME and ULSD which hold 25 litres and 15 litres of fuel respectively. Down below the tank, the OEM 5 $\mu$ m fuel filter was installed to prevent any particles from entering the fuel pump. The parallel fuel pump (Bosch model 260301501) was installed between the fuel filter and the engine fuel pump to provide the engine with constant head pressure. The surplus fuel returned from the fuel pump was connected to the fuel line where the water cooled heat exchanger was installed to control the fuel temperature. The flow rate of the cooling water on the heat exchanger was controlled by the solenoid valve. The fueling system was designed in such a way that the fuel temperature and pressure head are easily controlled to isolate the effect of this parameter on engine performance. Figure 3.17 shows the schematic diagram of the fuel line system of a V6 diesel engine.

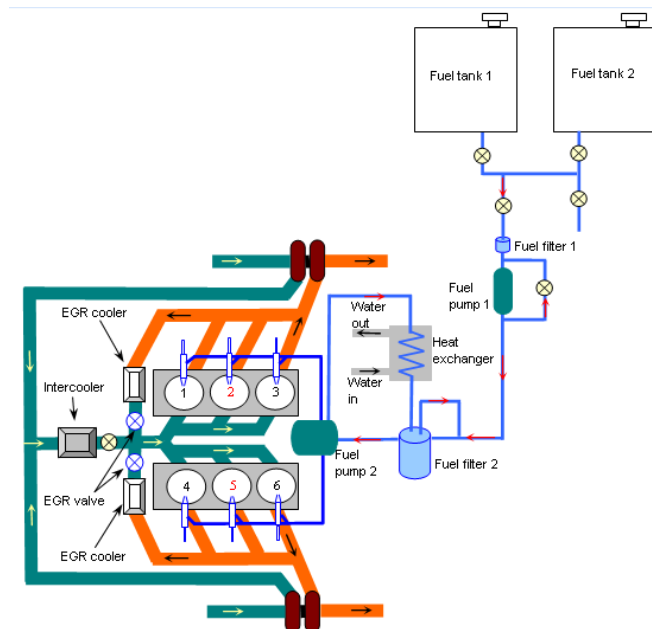


Figure 3.17 Schematic diagram of fueling system on a V6 diesel engine

The diesel engine was operated with certified ULSD and RME. The fuel was supplied by Shell Global UK Ltd. The details of the fuel properties given by the manufacturer are summarized in Table 3.4. The main differences in comparing RME with ULSD are (i) an increase in cetane number by 1.5%, (ii) an increase in density by 6.8%, (iii) an increase in viscosity by nearly 81%, (iv) a decrease in lower calorific value (LCV) by 8.7% and (v) a large decrease in sulfur content by 89.1%.

Table 3.4 Fuel properties

Properties	ULSD	RME
Cetane number	53.9	54.7
Density at 15°C [kg/m <sup>3</sup> ]	827.1	883.7
Viscosity at 40°C [cSt]	2.467	4.478
50% distillation	264	335
90% distillation	329	342
LCV [MJ/kg]	42.7	39.0
Sulfur [mg/kg]	46	5
Molecular mass (equivalent)	209	296
C (% wt.)	86.5	77.2
H (% wt.)	13.5	12.0
O (% wt.)	-	10.8

### 3.2.3.3 Engine Cooling System

The water from water taps was used as a cooling liquid on a V6 diesel engine cooling system. There were three heat exchangers in total used for the cooling purpose. A counter-flow heat exchanger manufactured by EJ Bowman Ltd was used as an engine cooler (HE1). The engine temperature was controlled by the thermostat

valve (TV) as depicted in Figure 3.18. The thermostat valve temperature setting was pre-set by the manufacturer at 86°C. The water flow rate was controlled by a manual butterfly valve to ensure that the mass flow rate was suitable for the engine when it was operated at any specific engine speed and load.

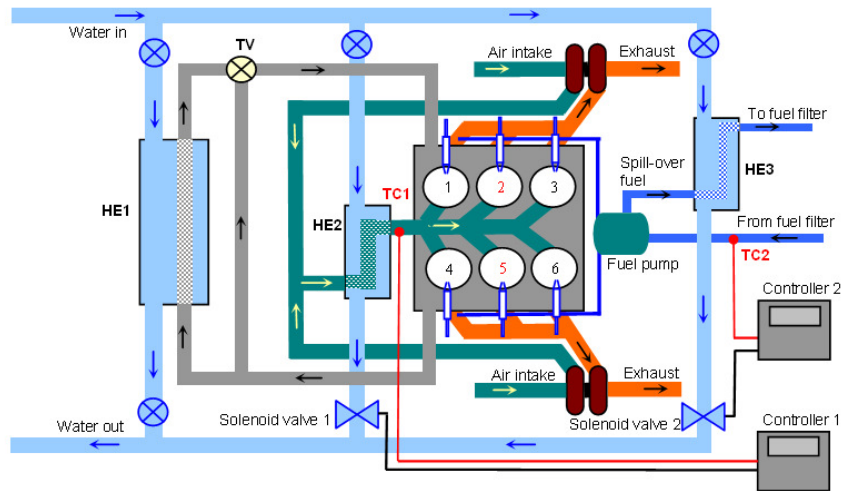


Figure 3.18 Schematic diagram of a cooling system on a V6 diesel engine

The smaller heat exchanger (HE2) was used to cool down boost air temperature on the intake manifold. This heat exchanger was located between the compressor and the intake manifold bank as clearly depicted in Figure 3.18. The boost air temperature was measured by a thermocouple (TC1) and used as a feedback to control the mass flow rate of water. The temperature controller (controller 1) was used to regulate the solenoid valve which controls the mass flow rate of the cooling water. The controller model ATR400-12BC was supplied by Pixsys Ltd. The specifications of Pixsys temperature controller was listed in Appendix B.

Another heat exchanger (HE3) was used to cool down the fuel temperature. When the engine is operated especially at high engine load, the temperature of spill-

over fuel rises significantly. Therefore, the fuel line temperature needs to be controlled. A similar technique was used to control the fuel temperature where the Pixsys temperature controller (controller 2) was used to regulate the solenoid valve (solenoid valve 2). Figure 3.18 also shows the circuit diagrams of the temperature controller for boost air temperature and fuel temperature.

### **3.2.3.4 Exhaust Emissions Measurement**

The exhaust gas emissions were measured mainly by an AVL DiGAS 440 gas analyzer. The emission gases measured included CO, THC, NO, CO<sub>2</sub> and O<sub>2</sub>. Moreover, the unit was also capable of measuring lambda from exhaust gases. The result was often compared with the result measured with the AVL CEB200 analyzer for calibration purposes. The emission parameters measured in AVL CEB200 include carbon monoxide and carbon dioxide by non-dispersive infrared method (NDIR), total unburned hydrocarbon by heated flame ionization detector (HFID) and nitrogen oxides by heated chemiluminescent detector (HCLD).

The exhaust gas was sampled at 30cm downstream of the turbine exit and connected to the gas analyzer (AVL DiGAS 440) by a stainless steel tube. The results of emission data, was displayed on the analyzers screen in real time basis for quick review. The results were also recorded in Excel file format on a Windows based PC in a control room. The standard Bosch smoke meter was used to measure the PM from the exhaust duct. The smoke was captured by the standard filter paper in a smoke meter when the foot-pedal was released. The smoke measurement was made

manually by putting the light on the sample paper and the reading was displayed by the dial gauge. The smoke meter measured the relative quantity of light reflected by the paper due to particulate collected on paper. Figure 3.19 shows the AVL DiGAS 440 analyzer and AVL CEB200 used throughout this study. The specification detail of the exhaust analyzers is attached in Appendix C.

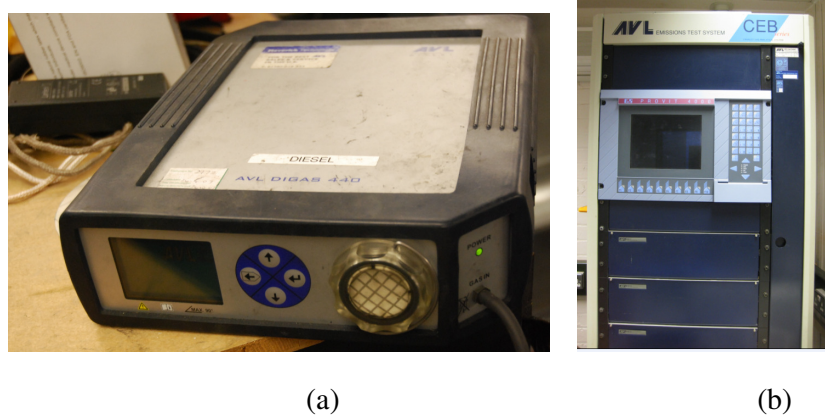


Figure 3.19 Exhaust gas analyzer, (a) AVL DiGAS 440 and  
(b) CEB200 exhaust gas analyzer

### 3.2.3.5 Data Acquisition System

The instrumentation of a Jaguar V6 diesel engine in the FPS Laboratory was mainly equipped with a National Instrument data acquisition system and LabVIEW software. The temperature was measured on 24 different locations on various engine components such as the exhaust duct, intake manifold and EGR. The temperature was measured by a k-type thermocouple which was connected to a 32-channel NI connector box. Figure 3.20 shows the arrangement of the data acquisition system of the test engine. The measurement was displayed in a LabVIEW GUI and could be

recorded as an Excel file format. Figure 3.21 shows the LabVIEW GUI used to display and recorded the data.

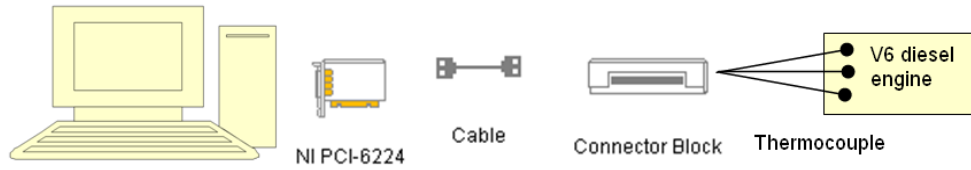


Figure 3.20 Arrangement of a NI DAQ Card, connector box and PC

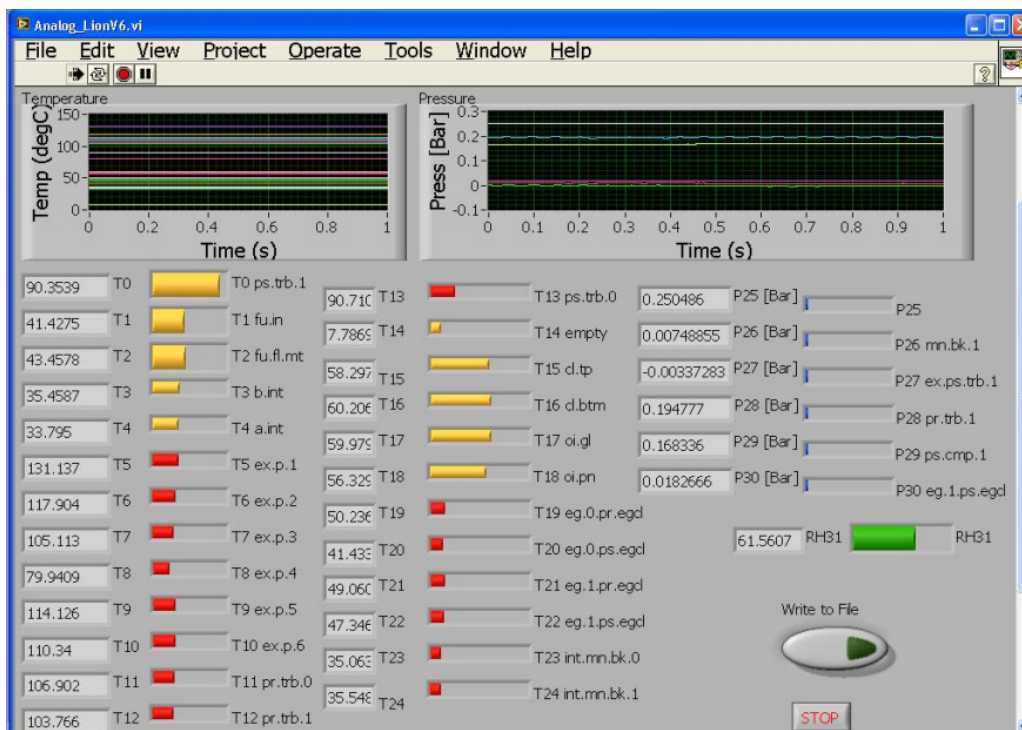


Figure 3.21 GUI of LabVIEW code for data display and record

The pressure on the intake manifold and the exhaust manifold was measured by a pressure transducer. The signal was wired to the 32-channel NI connector box. A relative humidity (RH) sensor by Honeywell (model HIH4000) was used to measure the relative humidity of the ambient air. The RH sensor was situated next to the

intake grill. The NI connector box was wired to the NI PCI-6224 DAQ card on a Windows based PC in a control room.

The in-cylinder pressure was measured in cylinder number 2 and 5 respectively. The Piezo glow plug high pressure transducer which supplied by AVL (Model AVL GU13G) was used to accurately measure the in-cylinder pressure history. The pressure transducer was wired to an AVL Piezo Amplifier 3066A03 at crankshaft positions recorded by an encoder. The pressure was measured in two cylinders, named cylinder 2 and 5 as depicted on Figure 3.22. The data was recorded for 100 engine cycles so that the average result could be calculated. The piezo sensor used has sensitivity of 15pc/bar. Both of the data (pressure and crank angle degree) were recorded through a National Instrument data acquisition system NI PCI-6023E installed in a Windows XP based PC. Figure 3.23 shows the AVL piezo amplifier for high a pressure transducer.

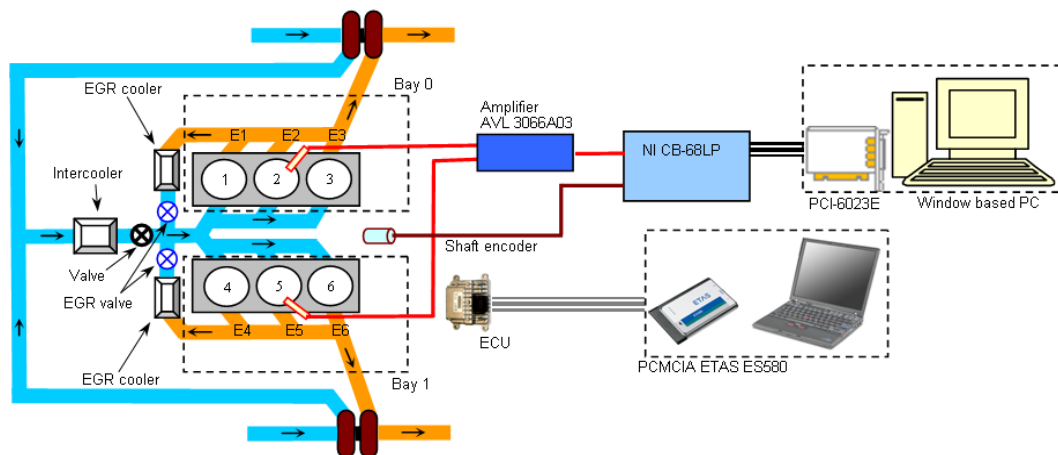


Figure 3.22 Schematic diagram of V6 diesel engine system



Figure 3.23 AVL Piezo Amplifier

An off-line steady state analysis based on in-cylinder pressure was carried out by the in-house LabVIEW code and the analysis included peak pressure, indicated power, coefficient of variation and indicated mean effective pressure (IMEP). The data was recorded 100 cycles to access a higher accuracy. Furthermore, the analysis of mass fraction burn, rate of heat release, brake specific fuel consumption (bsfc), thermal efficiency and ignition delay has been performed to evaluate the overall performance of the combustion. Figure 3.24 shows the GUI of LabVIEW 4 code used to read and analyse the data from in-cylinder pressure. The code was initially developed by Professor Wyszynski and it is successfully used by many researchers in the Future Power System (FPS) group.

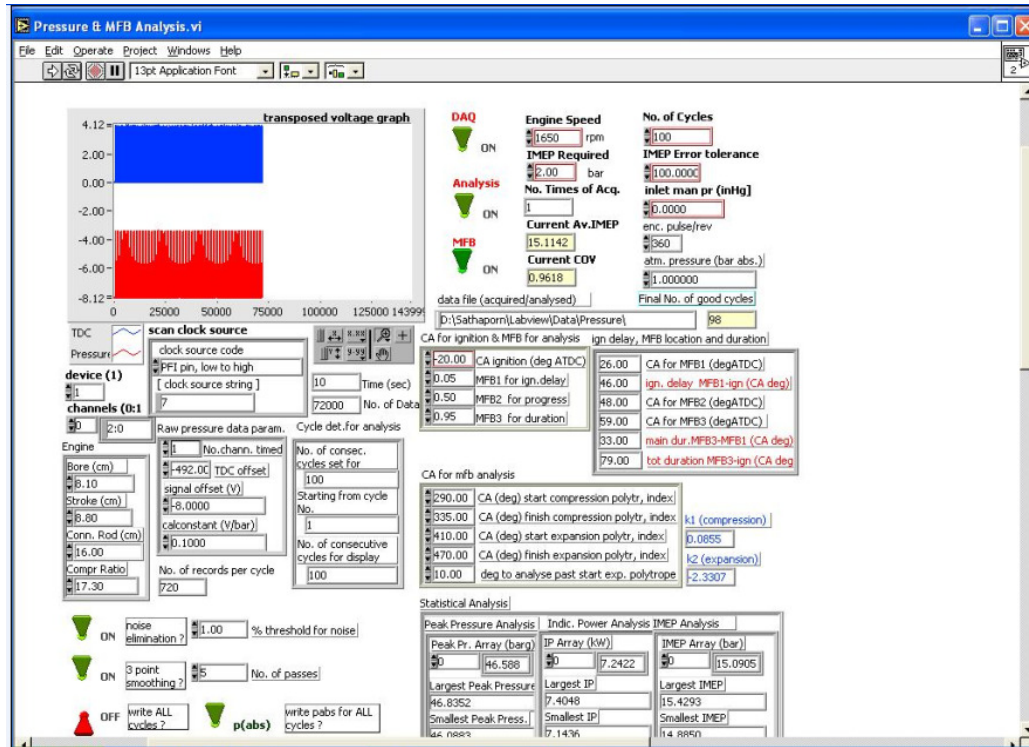


Figure 3.24 GUI of LabVIEW 4 to analyse the in-cylinder pressure

The engine data param was controlled by an ETAS unit, which was originally used by Jaguar for the development and calibration of the engine. It was operated with the boost air temperature and fuel temperature kept constant at 35°C. The EGR rate suitable for specific engine operating conditions was controlled by the Engine Management System (EMS) and the data was recorded by INCA software in a portable computer, together with other parameters from the EMS such as start of injection, fuel injection rate, boost air pressure, engine speed and EGR set-point. INCA is the universal software from the ETAS control unit. Moreover, INCA enables acquisition and recording of EMS signals along with additional related vehicle data. Figure 3.25 shows the GUI of INCA software used to monitor and alter the engine calibration.

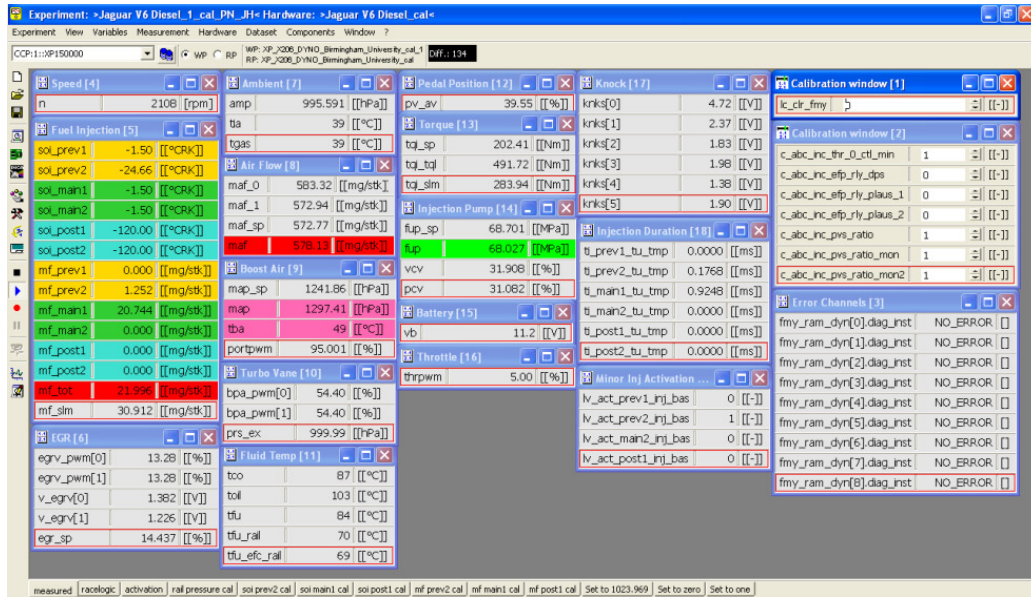


Figure 3.25 Main panel of INCA GUI to monitor the engine operation

### 3.3 Summary

In the presented chapter, the research methodology is discussed in detail. The research is separated into 4 categories, three dimensional simulation, one dimensional simulation, steady flow testing on the intake manifold and experimental works on a V6 diesel engine operating with RME and ULSD. The three dimensional simulation was conducted on 3D geometry of an AIS of a Land Rover using Fluent v6.3. The one dimensional simulation was conducted on a V6 diesel engine where the Ricardo WAVE software was used to analyse the wave action on the air intake manifold and the effect shown on engine performance. The steady flow test bench was designed, fabricated and tested in the laboratory. The experimental work was conducted on a V6 diesel engine operating with biodiesel to investigate the effect of air intake variables on the engines performance and emission.

## **CHAPTER 4**

# **CFD MODELLING OF AIR INTAKE SYSTEM AND VALIDATION**

### **4.1 Introduction**

The objective of the air intake modelling is to predict and analyze the flow through the intake system where the intake grill is positioned behind the front wheel arch of the vehicle. In most of the vehicles used today, the grill of the air intake is located at the front side to acquire the benefit of ram effect. In some cases, however, the grill is located behind the vehicle to improve wading performance. The study was focused on different flow speeds and vectors on the grill at high load operation where the air speed at the grill side is high and creates negative pressure. The CFD results are validated against experimental data of the steady flow test bench.

### **4.2 Problem Definitions**

Engine performance is sensitive to induction depression especially for Internal Combustion (IC) engines running without a turbocharger or supercharger. Most engine intake systems consist of dirty duct, air box, air cleaner, clean duct, intake

manifold plenum, and intake manifold runner. The typical length of the intake system can be up to one metre. The air path through this manifold presents a pressure drop challenge to the designer of an air induction system. A positive pressure at the end of the grill would help to overcome such a drawback. Thus, most car manufacturers position the grill at the front of the vehicle to maximise the capability of the engine to consume more air. Furthermore, drawing air from the front of the vehicle can minimise the interior noise contribution from the intake orifice. However, for those vehicles which have been designed to travel off-road, particularly for certain flood water level, the air intake should be able to allow the vehicle to cruise without sucking water into the engine. For the series of Range Rover vehicles, for instance, the grill intake currently points rearwards to the vehicle. Figure 4.1 shows the current model of 4x4 Freelander manufactured by Land Rover.



Figure 4.1 Freelander travel under specific level of the water (Motortorque 2008).

Under wind tunnel conditions, aerodynamic tests have recorded a slight negative depression in this area, a characteristic that can increase pressure drop on an air intake system. Figure 4.2 shows the static pressure on the vehicle body. The simulation is conducted on a Freelander model at ambient air speed of 100 km/h. The

simulation results of the vehicle body are fully developed and running at Jaguar Land Rover Research Center, Warwick. It clearly shows that the pressure distributions vary through the vehicle body. The positive pressure is clearly seen on the front of the vehicle. Meanwhile at the area of the air intake grill, the pressure is clearly negative. The negative pressure is developed at this region due to higher speed of air flow through the surface thus reducing the pressure.

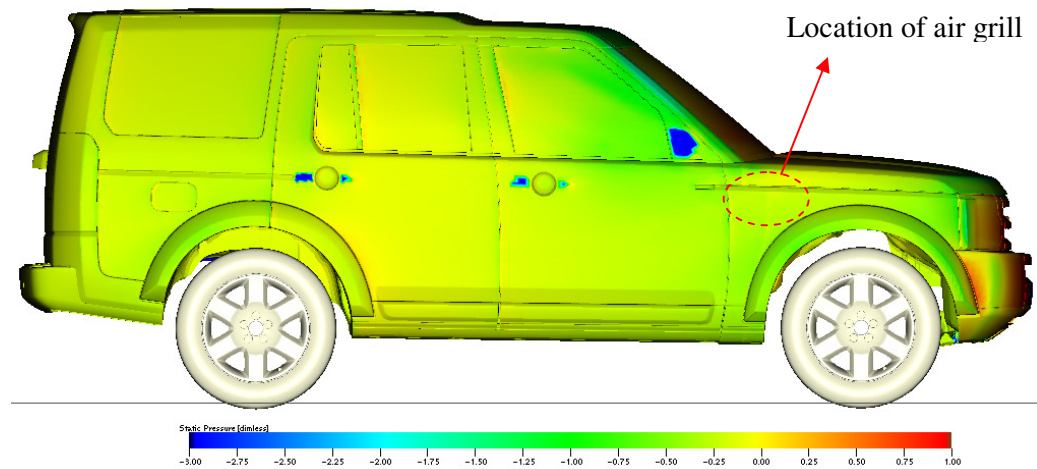


Figure 4.2 Pressure distributions on Freelande vehicle body  
(Source: Jaguar Cars Ltd)

Figure 4.3 shows the static pressure together with velocity vector over the vehicle surface. It clearly shows that the flow path in the intake grill region is about 30 degrees down the horizontal line relative to the ambient air flow directions. The pressure drop across the air intake system is known to have a significant influence on the indicated power of the IC engine. The pressure drop is created due to the suction generated by the descending piston in the case of a natural aspirated engine. The

pressure drop along the intake system is very dependant on engine speed and load, the flow resistance of different elements in the system, the cross sectional area through which the fresh charge moves, and the charge density (Heywood 1988).

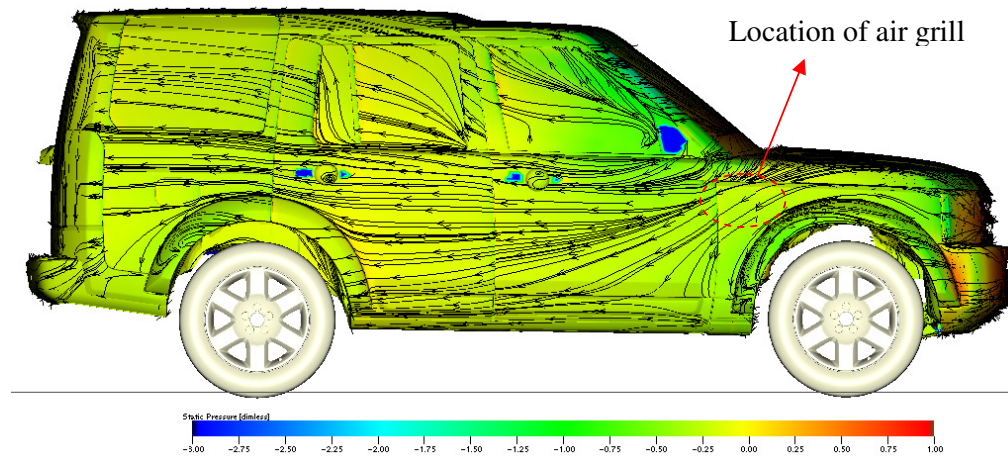


Figure 4.3 Velocity vector of fluid flow around the vehicle body

(Source: Jaguar Cars Ltd)

### 4.3 Boundary Conditions

The success of CFD simulations strongly depends on the chosen boundary conditions (Ganesan et al. 2004). Consequently, proper boundary conditions have to be carefully specified to minimise error. A velocity inlet boundary condition was used at the inlet where the simulation variables correlate well with static pressure at the grill surface. A pressure outlet boundary condition was used to define the static pressure at the outlet of the air intake duct. The static pressure term is used since the flow is subsonic. A no slip wall boundary was used to define a fluid-solid interface where viscous flow is considered.

The air filter in the airbox is modelled as a porous media. The porous media model offered by FLUENT have covered a wide variety of problems, including flows through packed beds, fibrous mat, perforated plates, flow distributors, and tube banks. In this approach, porous media are modelled by the addition of a momentum source term to the standard fluid flow equations. This momentum sink contributes to the pressure gradient in the porous cell zone, creating a pressure drop that is proportional to the fluid velocity (or velocity squared) in the cell (Fluent 2005). For the simplicity of the analysis, the viscous resistance and inertial resistance are estimated as  $420 \times 10^{10}$  and 120 respectively. These values are considered appropriate to this numerical analysis as the focus of the study is not on the filter itself but more on the flow behaviour of the air intake system due to the geometrical properties of the intake grill. Porosity of the filter is assumed to be uniform.

The simulations were ran under two different entry conditions. First phase: static air at the grill entry. Second phase: imposed tangential velocity at the grill entry. Under static conditions, the simulation was conducted for different mass flow rates to visualize the pressure drop across the intake grill and duct. The mass flow rates were 0.29, 0.3, 0.34 and 0.37 kg/s and are consistent with the experimental measurements. These mass flow rates were chosen to study the effect of high Reynolds number flows on the air intake system.

The second phase of simulations was to study the effect of tangential velocity at the grill side. The simulation was conducted with different air speeds at the grill side as depicted in Table 4.1. The outlet pressure was fixed at -62.58 Pa for all the simulations and representative of the pressure drop across the intake system at high engine speeds (>4000rpm). The assumptions have been made based on specifications

of a 2.2 litre Freelander diesel engine. Other parameter such as fluid density, viscosity, ambient pressure and inlet flow direction were kept consistent between simulations.

Table 4.1 Boundary conditions for numerical analysis at different air speeds

Mode	Pressure drop [Pa]	Tangential velocity [m/s]
1	-62.58	15
2	-62.58	20
3	-62.58	25
4	-62.58	30

A comparison between results of four different tangential velocities has been conducted in order to visualize the flow behavior on the intake manifold. It should be elucidated that the velocity direction across the grill is parallel to the grill surface as the air speed crosses the grill in the same way as when vehicles are running on the road.

#### 4.4 Result and Discussion

Figure 4.4 shows experimental results of pressure drops at 5 different locations on the whole air intake system at different mass flow rates. It is found that the static pressure drop gradually decreases from the intake grill to the end of the intake duct.

The pressure drop is directly related to the mass flow rate, where the higher mass flow rate shows a high pressure drop at every location on the air duct.

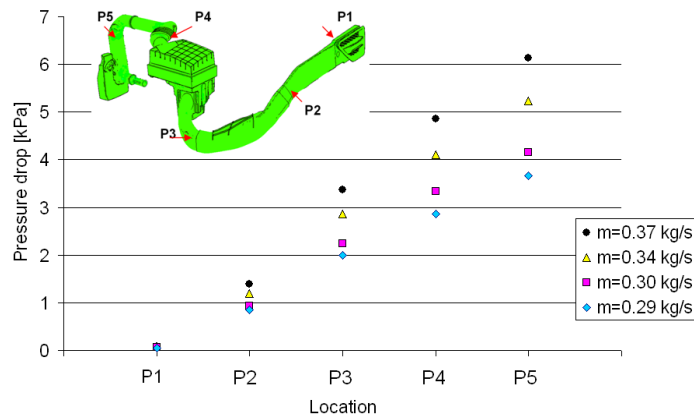


Figure 4.4 Pressure drop measured on five different locations at different mass flow-rate.

#### 4.4.1 Simulations under Static Entry Flow

The flow field was analyzed in the grill side of the intake system. Figure 4.5 shows velocity vectors at a mid plane section along the wingduct. The data is for a mass flow rate of 0.29 kg/s and gives a pressure drop of -1kPa. It is clearly seen that the velocity magnitude is non uniform across the grill area. Downstream of the grill, the air velocity becomes more uniform velocity up to the end of the wingduct.

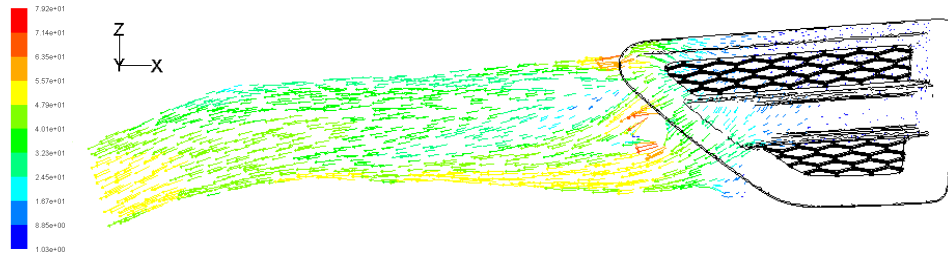


Figure 4.5 Velocity vector on x-z plane inside the duct [m/s]

Figure 4.6 shows the contours of static pressure at the middle plane section along the wingduct. It can be seen that the static pressure changes dramatically through the grill area. Downstream of the grill the pressure remains almost constant as the air flows along the wingduct. The static pressure is found to be a maximum at the stagnation point where there is a circular boss (wingduct mounting point) immediately downstream of the grill. Figure 4.7 show static pressure on the surface of the wingduct. This data also clearly showed a significant pressure drop across the intake grill. The result is in agreement with previous research on the AIS. Siqueira in his research report suggests that the AIS is supposed to increase the cross section area of the inlet duct to reduce the pressure drop on the inlet (Siqueira et al. 2006).

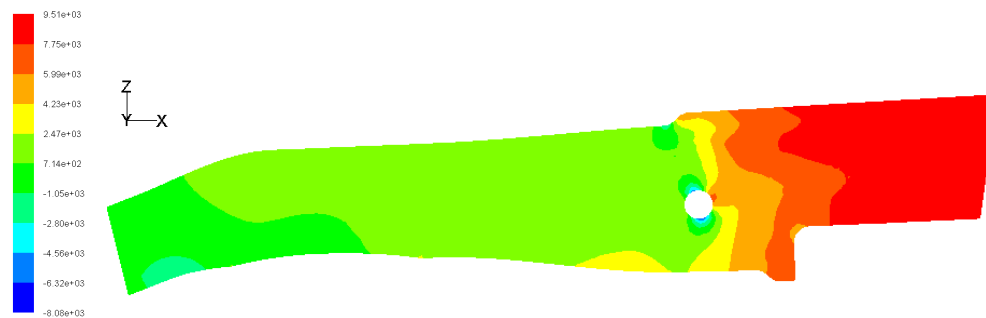


Figure 4.6 Contour of static pressure on x-z plane inside the duct [Pa]

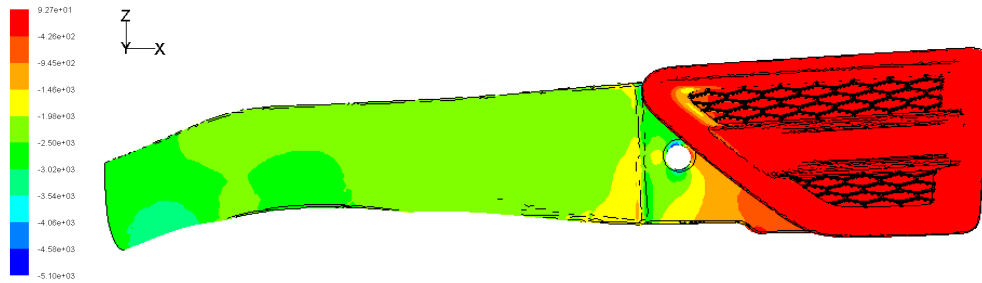
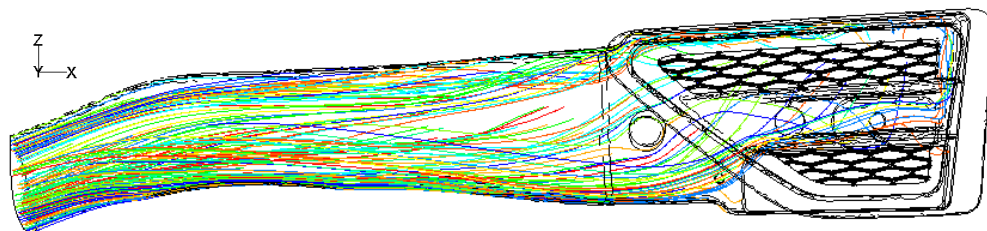
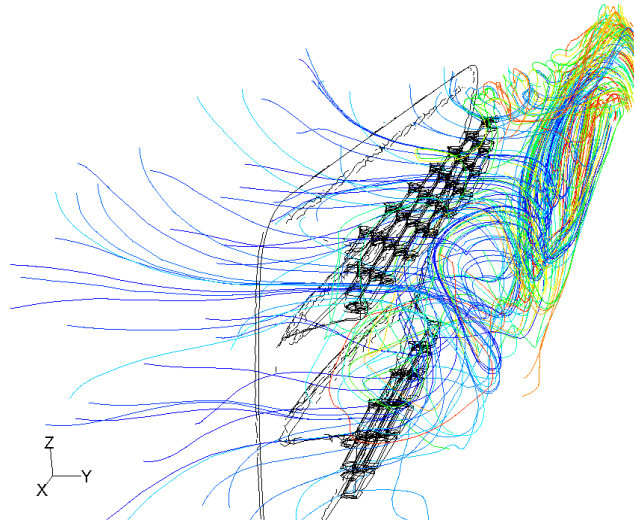


Figure 4.7 Contour of static pressure on intake grill [Pa]

Figures 4.8a and 4.8b show the flow path (coloured by particle ID) through the grill and wing duct. It is observed that after entering the grill the flow impacts the rear wall, causing a region of reticulating flow. A small spiral flow is generated at the end corner of the grill through the wingduct. The flow can be seen to be visually stable at the end of the wingduct. The flow pattern is found to be interrelated with the velocity profile and static pressure discussed earlier. Please note that these simulations were run with an initial air speed equal to zero and at ambient pressure. Thus, the flow path can be seen to be random and enters the grill from all directions (Figure 4.8b).



(a)



(b)

Figure 4.8 Path lines color by particle ID

A comparison between numerical analysis and experimental data for pressure drops at four different mass flow rates are presented in Table 4.2 and Figure 4.9. It is found that both sets of results are quite close and the deviation is of the order 7.3 to 2.0%. It is clearly seen that the pressure drop is proportional to the mass flow rates through the wingduct.

Table 4.2 Experimental against predicted pressure drop at location P2.

Mass flow rate [kg/s]	Experimental [Pa]	Numerical [Pa]	Error [%]
0.37	1393.0	1326.74	4.8
0.34	1191.0	1122.71	5.7
0.30	932.7	863.97	7.3
0.29	844.4	827.93	2.0

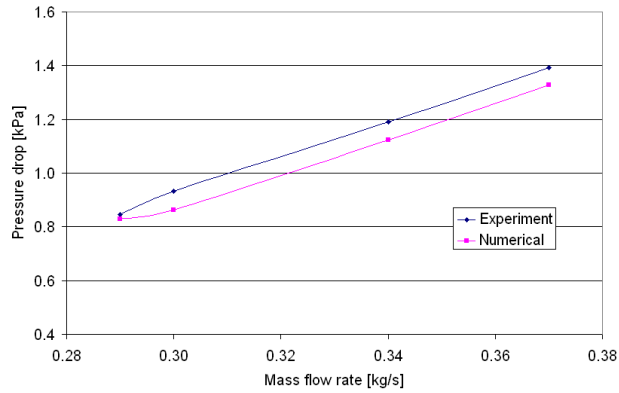
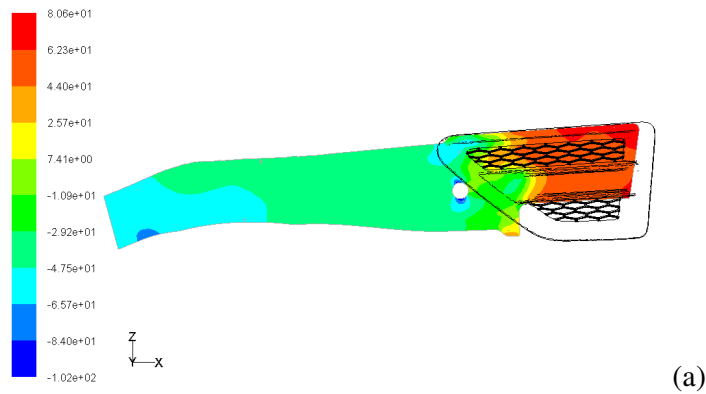


Figure 4.9 Pressure drop measured and calculated at P2 against different mass flow rates.

#### 4.4.2 Tangential Velocity Magnitude

In this section, the discussion is focused on the cases where the air velocity is parallel to the intake grill, and representative of the vehicle moving at specific speed. For these cases, it is found that the static pressure changes gradually along the wing duct from the grill area to the end of the wingduct. This is one major difference between these simulations and the simulations run drawing static air.



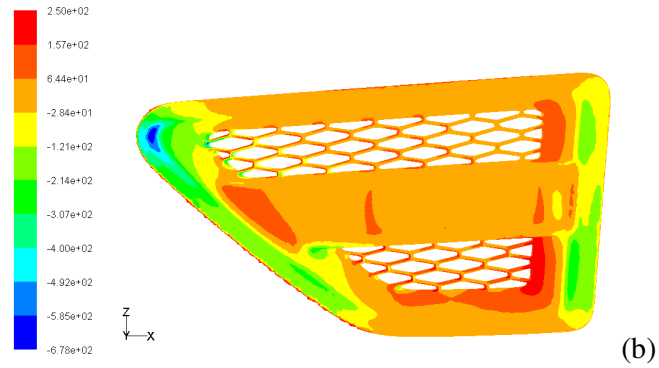
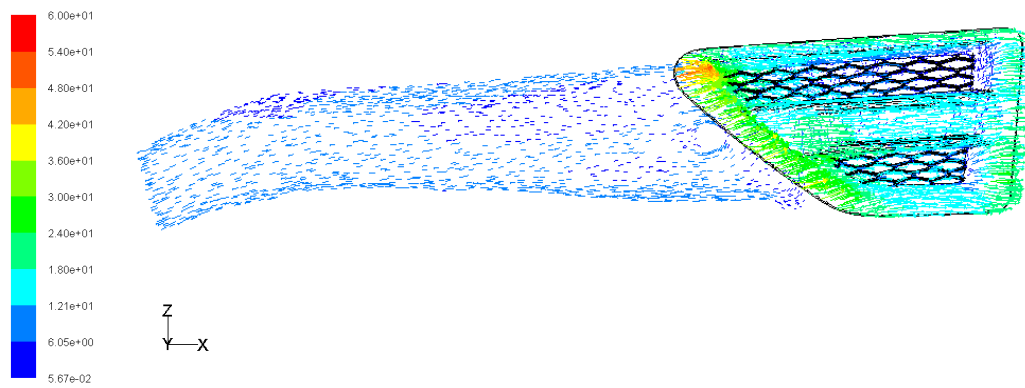


Figure 4.10 Contours of static pressure on (a) x-z plane inside the duct [Pa] (b) grill surface [Pa]

Figure 4.10b shows the negative pressure distribution at the grill surface due to the air velocity across the grill. The top left side of the grill shows a region of very low pressure due to the curvature of the grill and hence resultant high air velocity in that region. It can be seen that the pressure on the left side of the grill is reasonably uniform, except in the bottom left region where it shows relatively high pressure



(a)

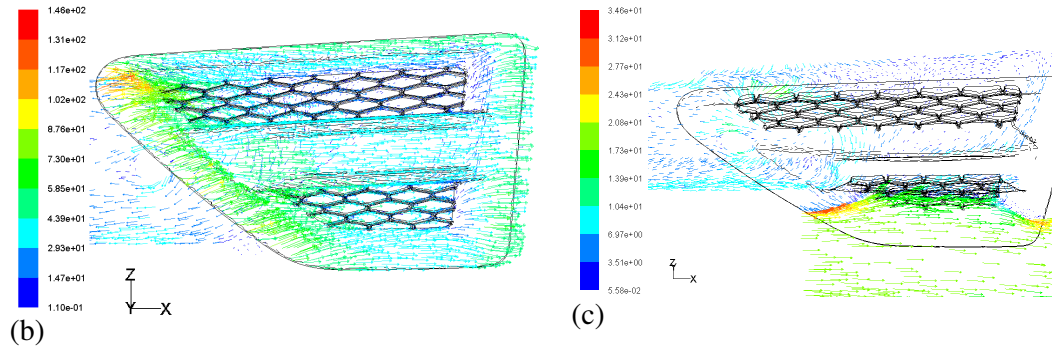


Figure 4.11 Vectors of velocity on the wingduct (a) x-z plane inside the duct (b) grill surface (c) x-y plane in the grill

Figure 4.11 shows the velocity vector on the grill and wingduct. The velocity profiles on the grill and wingduct section can be seen to differ slightly compared with the simulations conducted on phase 1 where static air applied to the initial velocity at the grill entry. The pressure decreases and thus generates less pressure drop between the outer grill area and the end of the wingduct due to the increase of air velocity on the grill side.

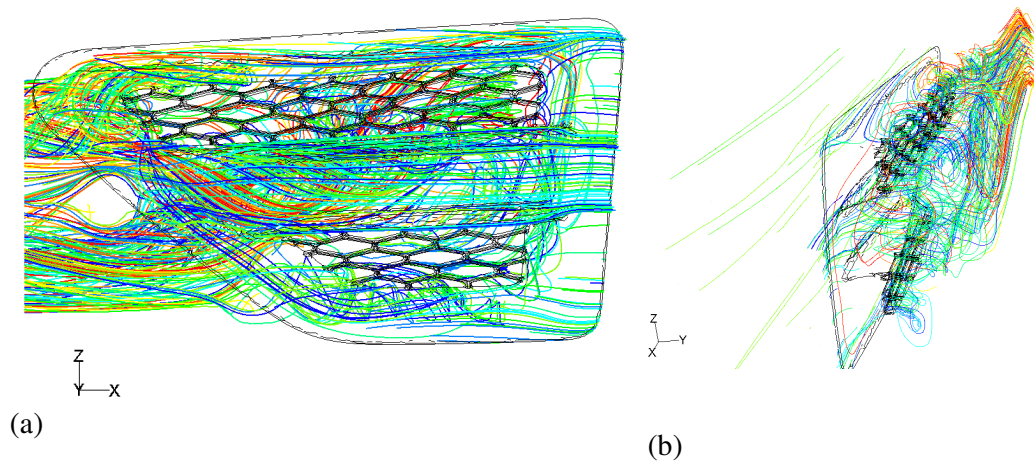


Figure 4.12 Path lines colored by particle ID. (a) inside the grill area (b) isometric view in wingduct area

Comparing Figures 4.12 and 4.8 shows the air flow through the grill to be more turbulent than the case with the static entry condition. It has been found that the mass flow rate is affected by the tangential velocity at the grill entry. In general the higher the tangential velocity, the lower the predicted mass flow rate. The mass flow rate reduces with tangential velocity due to lower static pressure at the grill inlet thus reducing the chance of mass air sucked into the intake duct. The lowest mass flow rate is seen for a tangential velocity at 25m/s due to high turbulent at the grill entry and reverse flow occurs at the outlet of the intake duct. In general, higher velocity on the grill surface possibly reduced the mass flow rate sucked to the engine.

Table 4.3 Simulation results of mass flow rate

Mode	Pressure drop [Pa]	Tangential velocity [m/s]	Mass flow rate [kg/s]
1	-62.58	15	0.0540
2	-62.58	20	0.0491
3	-62.58	25	0.0283
4	-62.58	30	0.0392

## 4.5 Summary

The flow behavior of a vehicle intake system was investigated through simulation work on an air intake system. The simulation result was validated with steady flow test. The main conclusions are:

1. The computed pressured drop is in a fair agreement with the experimental results for the case with static air at the grill entry. Thus, the development of the intake grill to achieve high volumetric efficiency can be performed using CFD rather than using trial and error.
2. In the case where the air velocity is tangential to the grill entry, there is a direct correlation between the magnitude of the tangential velocity and the mass flow rate sucked into the engine. In general, for a given constant pressure drop, the higher the tangential speed, the less mass flow into the engine. The lowest mass flow rate was found at 25m/s of tangential velocity due to high turbulence at the grill entry.

## **CHAPTER 5**

### **ONE DIMENSIONAL MODELLING OF A V6 DIESEL ENGINE AND VALIDATION**

#### **5.1 Introduction**

The Ricardo WAVE v7.2 is used in this research to investigate the effect of various parameters of the air induction system to the performance of a V6 diesel engine. The model is created in three distinct steps as recommended from the Ricardo WAVE manual guide; gathering the data, preparing the data and constructing the model in WaveBuild (Ricardo 2006). In this model, the engine and all the manifolds are modelled using one dimensional wave action codes by linking together the geometrical complex devices such as turbocharger, valves, junction and ducts.

#### **5.2 Engine Model Setup**

In general, a one dimensional (1D) simulation of an engine model consists of intake system, exhaust system, compressor and variable geometry turbocharger system (VGT), common rail fuel injection systems, exhaust gas recirculation systems, engine cylinders and valve train. The details of the all engine cylinder, ducts,

junction, turbocharger and fuel injection system for the simulation model were given in the Ricardo WAVE template. All the parameters required for simulations are provided as a pre-loaded option in the software package. Therefore, the actual parameter of the V6 diesel engine is just used to replace the pre-loaded parameter. Figure 5.1 shows the V6 diesel engine model in the Ricardo WAVE graphic user interface (GUI) panel. The list of elements in the left hand side of the image shows all of the features available in the simulation device library such as type of engine cylinder, duct, orifice, charging devices, valves and pipe junctions.

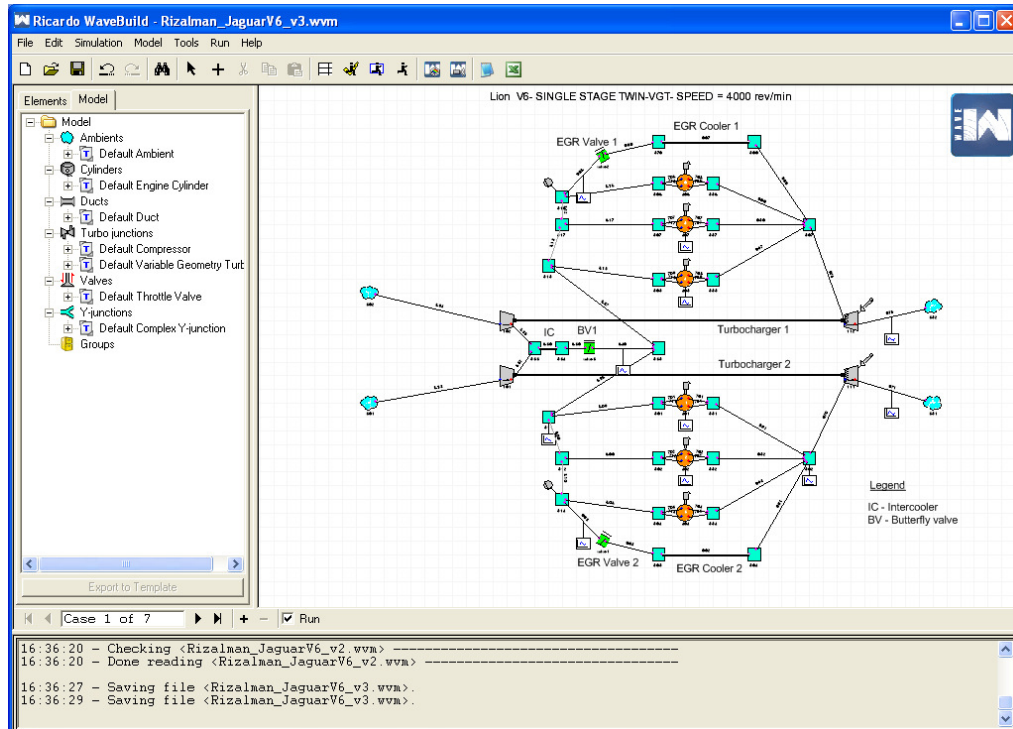


Figure 5.1. Ricardo WAVE software graphic user interface

### 5.2.1 General Parameter of Diesel Engine

There are many mandatory input parameters in the model that need to be inserted into the input panel in Ricardo WAVE software. Most of the data is provided by Jaguar such as compressor and turbine map, valve event, fuel injection strategies, injector type and dimension, EGR ratio and details of engine dimension. Some of the parameters are physically measured on the engine such as diameter and length of duct and manifold. The details of the engine parameters used in this model are described in Table 5.1.

Table 5.1 Detail parameter of a Lion V6 diesel engine

No	Description	Value
1	Fuel	Diesel
2	Engine Type	V6
3	Displacement	2721 cm <sup>3</sup>
4	Injection System	Common-rail
5	Induction System	Twin-Turbo (VGT)
6	Valves/Cylinder	4
7	Bore x stroke	81 mm x 88 mm
8	Connecting Rod Length	160 mm
9	Compression Ratio	17.3
10	Intake Valve Max. Lift	8.00 mm
11	Exhaust Valve Max. Lift	8.10 mm
12	Intake Valve Diameter	25.9 mm
13	Exhaust Valve Diameter	23 mm
14	Intake Duration	252 CAD
15	Exhaust Duration	291 CAD
16	RPM Range	1000 – 4000 rpm
17	Peak Power	150 kW @4000rpm
18	Peak Torque	435Nm @1900rpm

In general, the Ricardo WAVE works with various boundary conditions such as orifice, open intake pipe, restriction valve and more. The flow in all of these futures is treated as one dimensional. Therefore the pressure, temperatures and flow velocities obtained from the numerical solutions of gas dynamic equations represents the mean values of the cross section of the pipes. Moreover, the flow losses due to three dimensional effects at any specific locations in the model are considered by appropriate flow coefficients. Therefore the arrangement of the pipes and duct is crucial in the one-dimensional model due to wave propagation action. In order to model the engine, the arrangement diagram of the cylinder, duct, turbocharger, and intercooler need to be planned. There are a number of elements especially the duct and junction that need to be simplified to reduce simulation time and complexity. Figure 5.2 shows the schematic overview of the V6 diesel engine air flow system.

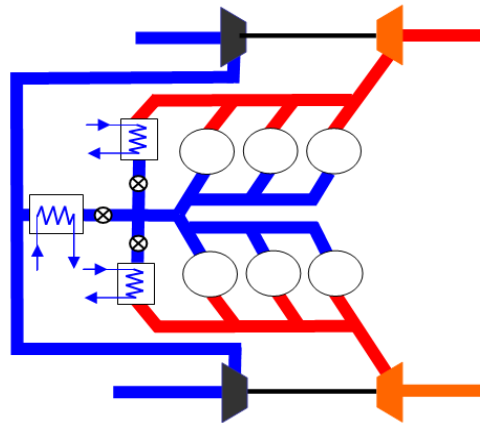


Figure 5.2 Schematic diagram of the engine model.

The construction of a V6 diesel engine model begins with the arrangement of the engine cylinder, intake and exhaust valve, intake and exhaust duct, compressor, turbine, intercooler, fuel injector, EGR pipe and EGR cooler. Figure 5.2 is used as a guide to construct the engine in the

WAVEBuilt™ panel which simply is called a canvas. The component details of the engine such as cylinder, junction, duct, valves, turbine and compressor are simply click-and-drag from a list of elements panel to the canvas as clearly depicted in Figure 5.3

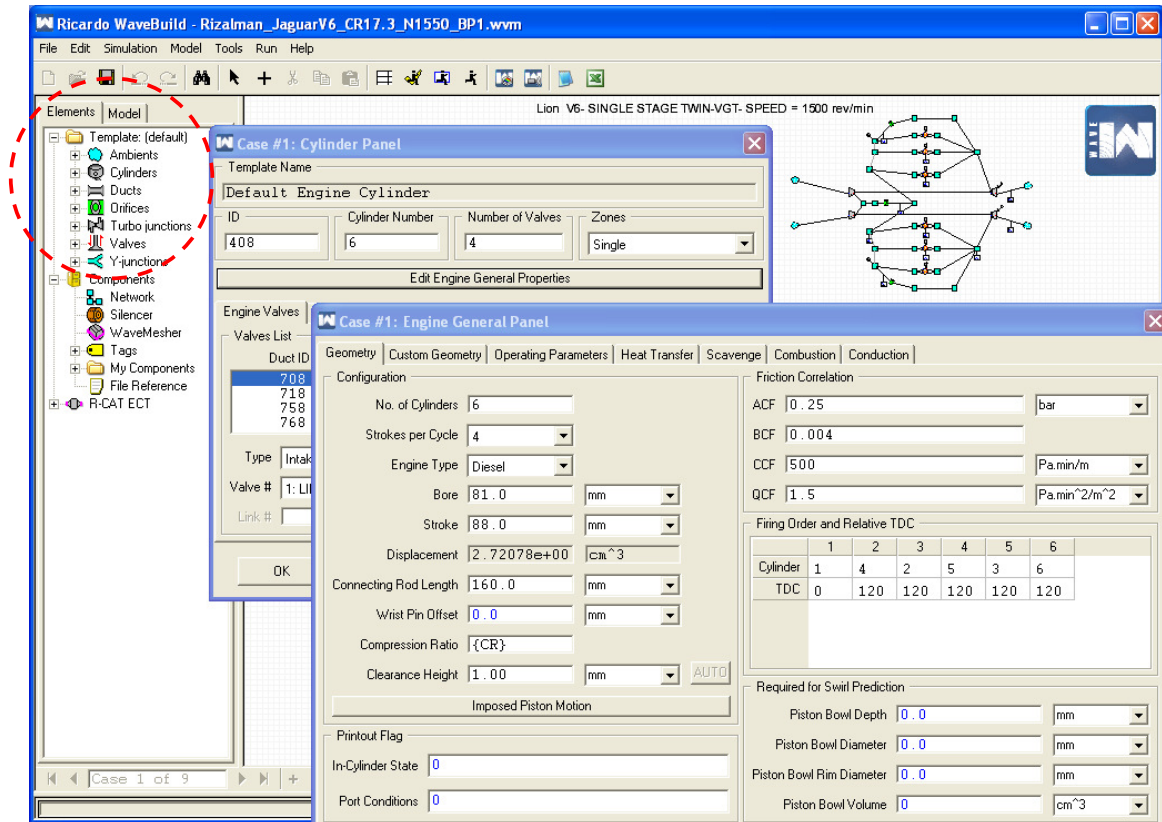


Figure 5.3 The preloaded component of engine component available from elements panel

## 5.2.2 Heat Transfer and Combustion Model

The details of engine general parameters were entered in the cylinder panel on the WAVE model when the arrangement of the engine was completed. The engine

general properties include engine type, number of engine cylinders, stroke per cycle, cylinder geometry, compression ratio, clearance height and firing order and relative to TDC (multiple cylinder). Figure 5.3 clearly shows how the engine parameter was set into the engine model. The friction correlation number was left as the default number. The study did not include the swirl analysis on the engine, therefore the details of swirl parameter on the engine cylinder were set to the default number as zero.

Other parameters such as heat transfer and combustion model also need to be specified on the engine model. The calculation of heat transfer from the gas to the cylinder engine was estimated by Woschni equations (Woschni 1967). The model was successfully used by many researchers to model heat transfer in SI engines (Quintero et al. 2007; Lejsek et al. 2009) and CI engines (Jajoo et al. 2005; Kubicki et al. 2007). However, the original Woschni model need to be modified for the HCCI engines to access higher accuracy as can be found detail in the literature (Jia et al. 2008; Manente et al. 2008). The Woschni correlation which expresses the convective heat transfer coefficient ( $h_g$ ) is given as (Ricardo 2009)

$$h_g = 0.0128D^{-0.2}P^{0.8}T^{-0.53}v_c^{0.8}C_{enht} \quad (5.1)$$

where D is the engine cylinder bore; P is the cylinder pressure and T is the cylinder wall temperature. The calculations of the heat transfer in Woschni model include an additional scaling multiplier  $C_{enht}$  for many applications in the diesel engine model. The velocity terms,  $v_c$  in equation 5.1 is denoted as a characteristic velocity, which is the sum of the mean piston speed and an additional combustion-related velocity that

depends on the difference between the cylinder pressure and the pressure that would exist under motoring conditions (Ricardo 2009). The value is given by Woschni as

$$v_c = c_1 v_m + c_2 \frac{V_D T_r}{P_r V_r} (P - P_{mot}) \quad (5.2)$$

Where  $v_m$  = mean piston speed (m/s)

$V_r$  = reference volume (m<sup>3</sup>)

$P_r$  = reference pressure (Pa)

$T_r$  = reference temperature (K)

$V_D$  = volume displacement (m<sup>3</sup>)

$C_1$  is a dimensionless number and given by the equation according to the specific stroke as shown by equation 5.3 and 5.4 (Ricardo 2009).

$$\text{During scavenging} \quad C_1 = 6.18 + 0.417 \left( \frac{v_s}{v_m} \right) \quad (5.3)$$

$$\text{When the valves are closed} \quad C_1 = 2.28 + 0.308 \left( \frac{v_s}{v_m} \right) \quad (5.4)$$

$C_2$  is a dimensionless number and given by the equation according to the specific stroke as shown bellows (Ricardo 2009).

$$\text{During combustion} \quad C_2 = 3.24 \times 10^{-3}$$

$$\text{During scavenging} \quad C_2 = 0.0$$

The swirl velocity,  $v_s$  is calculated based on user input on the engine cylinder panel.

The swirl velocity also can be calculated from the equation below

$$v_s = \pi R_{swirl} D \frac{N}{60} \quad (5.5)$$

Where  $R_{swirl}$  is the swirl ration,  $N$  is engine crankcase speed in rpm.

The diesel engine combustion process in WAVE simulation software used Diesel Wiebe model to incorporate an ignition delay sub-model with a Wiebe function (Ricardo 2009). The ignition delay is calculated based on the in-cylinder pressure and temperature during the combustion stroke. The ignition delay is calculated as follows:

$$\Delta\theta_{delay} = 323 \exp^{\min(2100C/T_{sum}, 80)/P_{sum}} \quad (5.6)$$

Where  $C = \frac{67}{25 + cn}$  (5.7)

$$T_{sum} = \sum_n \frac{T_c^n + T_c^0}{2} \frac{\Delta\theta_n}{\theta_{n+1} - \theta_0} \quad (5.8)$$

$$P_{sum} = \sum_n \frac{P_c^n + P_c^0}{2} \frac{\Delta\theta_n}{\theta_{n+1} - \theta_0} \quad (5.9)$$

Where  $T_c^n$  and  $P_c^n$  are the local cylinder temperature and pressure respectively while  $T_c^0$  and  $P_c^0$  are the cylinder temperature and pressure at the beginning of the ignition delay period.  $\Delta\theta_n$  is the time step size in degrees and  $\theta_0$  is the beginning of the ignition delay interval in angle degrees. This correlation also includes the dependency on the fuel cetane number as an addition to the in-cylinder temperature

and pressure profile. The correlation above clearly shows that the fuel cetane number has inverse correlation with ignition delay. This is in agreement with the result from many researchers as discussed detail in the literature (Heywood 1988). As an alternative to the ignition delay input, the delay period calculated from the experiment can be inserted into the model if required.

The WAVE model used Wiebe combustion model which is explained in detail in the literature (Watson et al. 1980; Mahallawy et al. 2002; Stiech 2003). The model predicted the correlations for premixed and diffusion burn regimes which are widely used to study the combustion progress in engine cylinder (Hajireza et al. 2000; Stenl  as et al. 2002; Caton 2003). The Wiebe combustion model provides a good representation for typical mass fraction burn relationships and character of the burn (Caton 2003). Experimental evidence from the literature has shown that about 70% of fuel burns during the premixed and diffusion phase (Heywood 1988). Therefore, the analyses of heat release from these regions are crucial. Moreover, an additional function to the original Wiebe model has been added in WAVE to characterize the slow late burning at the end of the diffusion burning phase (Ricardo 2006). This phase is also known as tail burning in some literature. The mass fraction burn (MFB) calculated in the simulation is given as (Ricardo 2006):

$$MFB = p_f \left( 1 - [1 - (0.75\tau)^2]^{5000} \right) + d_f \left( 1 - [1 - (cd_3\tau)^{1.75}]^{5000} \right) + t_f \left( 1 - [1 - (ct_3\tau)^{2.5}]^{5000} \right) \quad (5.10)$$

The premixed fuel fraction,  $p_f$  is obtained from either the model calculation or from the experimental value. The value of diffusive fuel fraction,  $d_f$  and tail fuel fraction,  $t_f$  is calculated from the equation below (Ricardo 2006).

$$d_f = (1 - p_f)(1 - \alpha) \quad (5.11)$$

$$t_f = (1 - p_f)\alpha \quad (5.12)$$

Where  $\alpha = 0.6[\min(\Phi, 0.85)]^2$   
 (5.13)

$$\tau = \frac{\theta - \theta_b}{125 \left( \frac{N}{N_B} \right)^{0.3}} \quad (5.14)$$

$$cd_3 = \frac{0.055}{1 + 0.5 \min(\Phi, 0.85)} \quad (5.15)$$

$$ct_3 = \frac{3.7cd_3}{1.12 \min(\Phi, 0.85) + 1} \quad (5.16)$$

Where  $N_B$  is brake engine speed,  $\Phi$  is the equivalence ratio and  $\theta_b$  is the start of combustion. The duration of fuel burning varies inversely with  $N_B$  where at higher values of  $N_B$  result in shorter burn duration and lower values of  $N_B$  result in a longer burn duration as explain detail in the Ricardo WAVE manual (Ricardo 2006).

### 5.2.3 Engine Valves, Injection Timing and Turbocharger Set-up

The detailed properties of valve event, injection timing, turbine and compressor mapping are provided by the engine manufacturer. The physical dimensions of the intake valve and exhaust valve are accurately measured and inserted into the simulation model. The valve lift profile for both intake and exhaust valve together with flow coefficient profile is provided by the manufacturer. Figure 5.4 shows the valve lift profile for the V6 engine. The data is put into the simulation panel with the anchor placed at the specific crank angle degree based on the cam profile. Figure 5.5 (a) and (b) shows the valve lift profile for the intake and exhaust respectively in the Ricardo WAVE software.

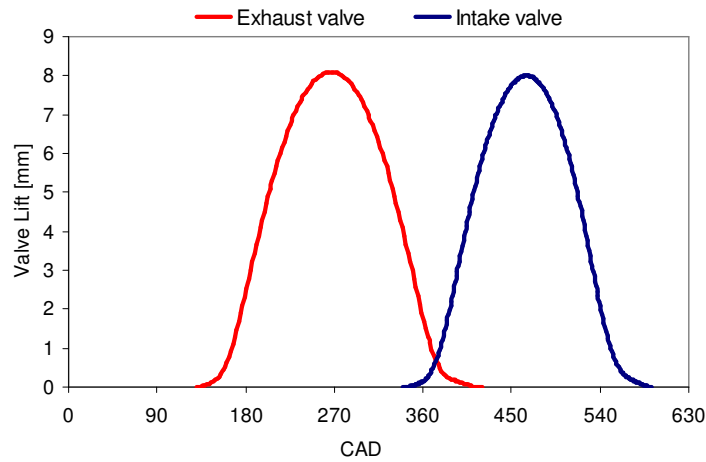
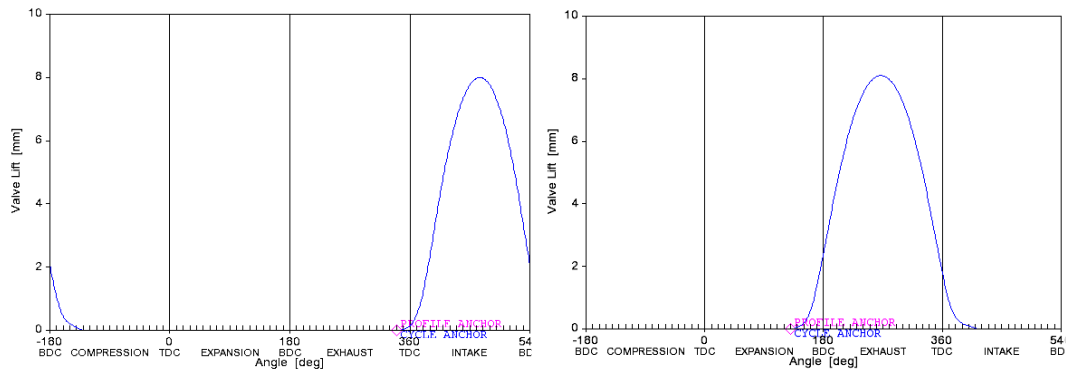


Figure 5.4 Valve lift profile for the V6 engine



(a) Intake valve lift profile

(b) Exhaust valve lift profile

Figure 5.5 Valve lift profile in Ricardo WAVE software (a) intake valve lift profile,

(b) exhaust valve lift profile

The actual physical features of the injector such as sac volume, number of injector nozzles, nozzle diameter and spray spread angle are also revised in the simulation model. The injection strategy mapping is retracted from the EMS by INCA Software. The data of injection pressure and injection rate is inserted in the injector editor over a wide range of engine speeds. Figure 5.6 shows the injection strategy of the engine over a broad range of engine speed and load.

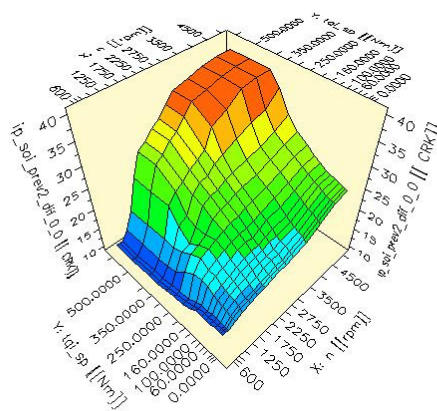


Figure 5.6 Injection strategies for the V6 engine

The compressor map and turbine map are simply loaded into the simulation model as the file is completely provided by the manufacturers. The turbine maps are consist of six stages as the variable geometry turbine is used. Figure 5.7 shows the example of compressor map as provided by the manufacturer (Garrett 2004). Appendix E shows the turbine performance measures as provided by Jaguar Cars.

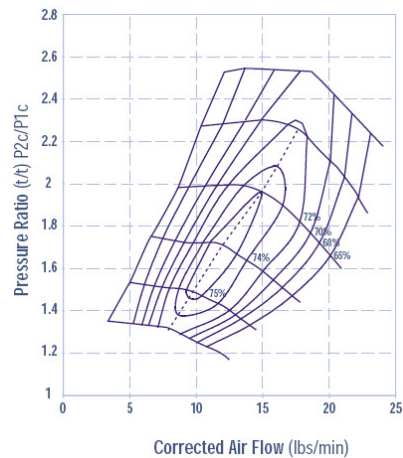


Figure 5.7 Compressor map of a VGT turbocharger (GT15), (Garrett 2004)

## 5.3 Simulation Results and Data Validation

### 5.3.1 Simulation Result and Validation at Full Load Curve

The experimental tests at full load have been conducted by the engine manufacturer. The engine is used to operate with ULSD under standard test procedure. The results include engine power and torque, mass flow rate and brake specific fuel consumption. The test result is used to calibrate with the simulation model. For the purpose of engine calibration, the model is used to simulate the diesel engine which operated with standard diesel in the fuel library of Ricardo WAVE

software. The model is simulated at seven engine speeds which are 1000, 1500, 2000, 2500, 3000, 3500, and 4000rpm. The results from the simulation model were compared against the test data. Figure 5.8 shows the power and torque curve from the test data and numerical results.

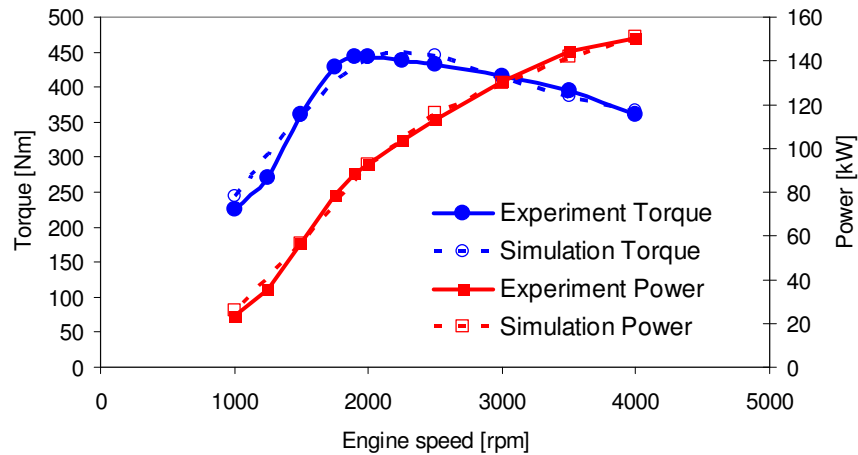


Figure 5.8 Power and torque curve

It is clearly seen that the simulation result for both engine power and brake torque are in good agreements with experimental data provided by Jaguar Land Rover. Figure 5.8 shows that the maximum power of the engine is increased as engine speed increase from 1000rpm to 4000rpm. The maximum engine power is achieved at maximum engine speed of 4000rpm. While the maximum torque for experiment and simulation is achieved at the engine speeds of 1900rpm and 2000rpm respectively. The difference is expected as the simulation inputs spread from 1500rpm to 2000rpm.

Table 5.2 Comparison of the test and simulation result

Engine speed, (rpm)	Power			Torque		
	Experiment (kW)	Simulation (kW)	Relative different (%)	Experiment (N.m)	Simulation (N.m)	Relative different (%)
1000	23.60	25.63	8.59	225	244.72	8.77
1500	56.60	56.47	-0.23	360	359.50	-0.14
2000	92.80	92.34	-0.49	443	441.62	-0.31
2500	113.00	115.93	2.59	432	445.59	3.14
3000	130.70	129.75	-0.72	416	412.70	-0.79
3500	144.60	141.66	-2.03	395	386.47	-2.16
4000	150.60	151.23	0.42	360	366.00	1.67

The final results of the simulations made for both power and torque over broad engine speeds are summarized in Table 5.2. It is found that the power and torque curves are in agreement between experiment and simulation within the range of 1500rpm and 4000rpm with relative error stretch from 0.23 to 2.5% and 0.14 to 3.14% for power and torque respectively. Meanwhile at the low engine speed of 1000rpm, the power and torque are different at about 8.59% and 8.77% respectively.

Figure 5.9 clearly shows that the bsfc for bit experimental and simulation results. The results are in good agreement between simulation and experimental data. The bsfc for simulation produced a slightly lower result as compared to the experimental data. The details of the data both from simulation and experiment are shown in Table 5.3.

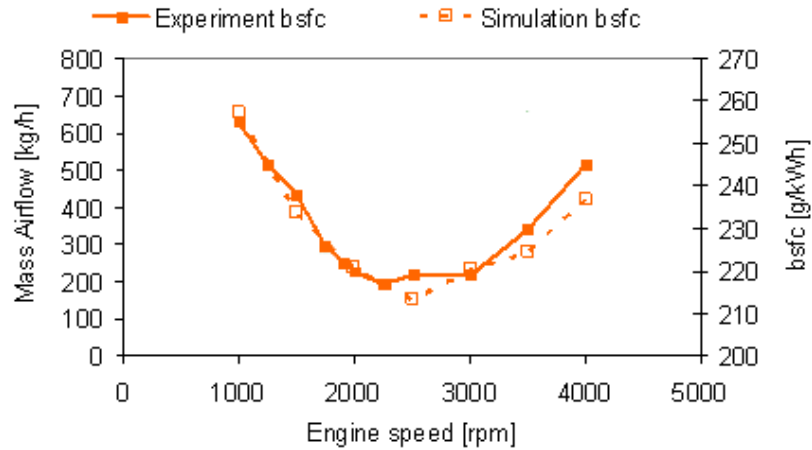


Figure 5.9 Calibration of mass air flow and bsfc.

Table 5.3 Mass air flow and bsfc of a V6 diesel engine

Engine speed, [rpm]	Mass air flow			bsfc		
	Experiment [kg/h]	Simulation [kg/h]	Relative different (%)	Experiment [g/kWh]	Simulation [g/kWh]	Relative different (%)
1000	90.00	95.55	6.17	255	257.54	1.00
1500	200.00	201.33	0.67	238	233.75	-1.79
2000	345.00	375.21	8.76	220	220.92	0.42
2500	425.00	441.23	3.82	219	213.50	-2.51
3000	515.00	521.13	1.19	219	220.58	0.72
3500	610.00	645.32	5.79	230	224.49	-2.40
4000	690.00	712.32	3.23	245	236.79	-3.35

Table 5.3 shows that the results from the simulation agreed well with the experimental data for all engine speeds. In general, the relative difference of mass air flow and bsfc is lower than 9% and 4% respectively. The mass air flow is well converged with the experimental data, which the relative error ranges from 1.19% to

8.76%. For bsfc, the difference is between 0.42% to 3.35%. The data has proved that the model is well validated with the experiment.

Therefore, in general the simulation is fairly accurate and can be used to study the effect of various parameters on the engine intake manifold to the engine performance. Engine torque and power depends on, among other factors, the amount of fuel injected and the fuel properties.

### **5.3.2 Simulation Results with Variable Boost Pressure**

The Ricardo WAVE diesel engine model was used to study the effect of intake port static pressure on the performance of the engine. The three inch butterfly valve (BV) was installed just after the intercooler to vary the pressure in the intake duct. Figure 5.1 shows the location of BV on the V6 diesel engine model. Under full load conditions, the valve plate angle (VPA) was varying as tabulated in Table 5.4. All cases were easily represented by the testing mode marked as M1 towards M6 as listed in Table 5.4. The baseline model was running at VPA 90 degree (M1). In this case, the effect of the valve positions is assumed to be negligible. Pressure drop ( $P_{drop}$ ) represents the relative difference of intake port static pressure (IPSP) between the baseline case (VPA 90 degree) and the referred mode. The data from Table 5.4 shows that the pressure drop is slightly increased as the VPA is reduced from 90 to 20 degrees.

Table 5.4 Valve plate angle and intake port static pressure

Engine Speed (rpm)	VPA = 90 M1		VPA = 70 M2		VPA = 50 M3		VPA = 30 M4		VPA = 25 M5		VPA = 20 M6	
	IPSP (bar)	P <sub>drop</sub> (%)										
4000	2.19264	0	2.19262	0.0009	2.19068	0.0894	2.16779	1.1333	2.14041	2.3821	2.06141	5.9850
3500	2.05872	0	2.05867	0.0024	2.05677	0.0947	2.03371	1.2148	2.00493	2.6128	1.93228	6.1417
3000	1.91247	0	1.91243	0.0021	1.91015	0.1213	1.88777	1.2915	1.85949	2.7702	1.78662	6.5805
2500	1.82372	0	1.82369	0.0016	1.82175	0.1080	1.80218	1.1811	1.77627	2.6018	1.70831	6.3283
2000	1.61449	0	1.61442	0.0043	1.61105	0.2131	1.57941	2.1728	1.54596	4.2447	1.46872	9.0289
1500	1.22521	0	1.2252	0.0008	1.22456	0.0531	1.21776	0.6081	1.20913	1.3124	1.18572	3.2231
1000	1.07294	0	1.0729	0.0000	1.07271	0.0214	1.07054	0.2237	1.068	0.4604	1.06103	1.1100

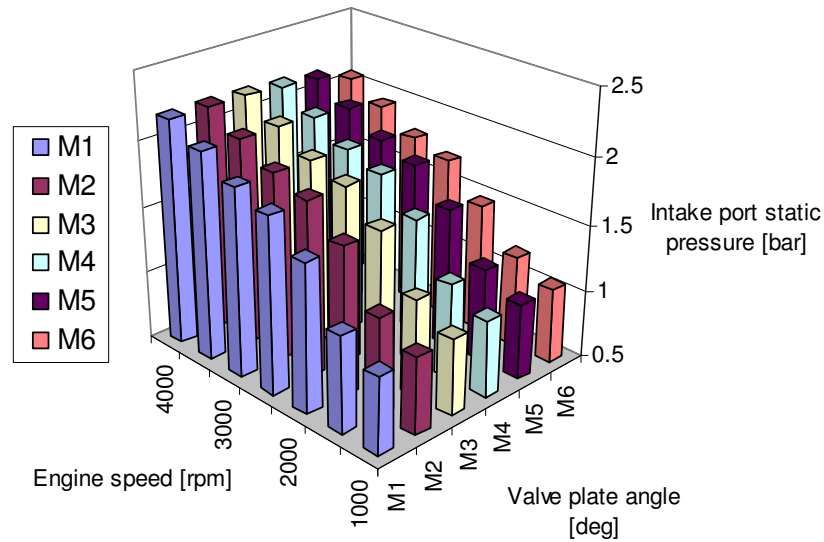


Figure 5.10 Intake port static pressure responses as VPA altered.

Figure 5.10 presents the simulations result and it shows that the intake port static pressure varies according to the valve plate angle of the butterfly valve. The pressure in the intake port is decreased as VPA decreases at all engine speeds except at 1000rpm. For the baseline model, the intake port static pressure increase from about 1 bar to 2.3 bar when the engine speed increase from 1000rpm to 4000rpm. It was found that at the engine speed of 1000rpm, the variation of VPA from 90 to 20

did not alter the intake port static pressure. This was due to the low boost effect by the compressor when the engine speed is low.

Engine air flow is one of the many parameters that have direct association with pressure drop in the intake manifold. The air flow is generally proportional to the engine speed due to the compressor speed in a turbocharger system. At low engine speed, the turbine speed is low due to lack of energy available in the exhaust manifold. While at high speed, the performance of the turbocharger is limited by the compressor width and efficiency. However, this setback is improved by using the VGT turbochargers.

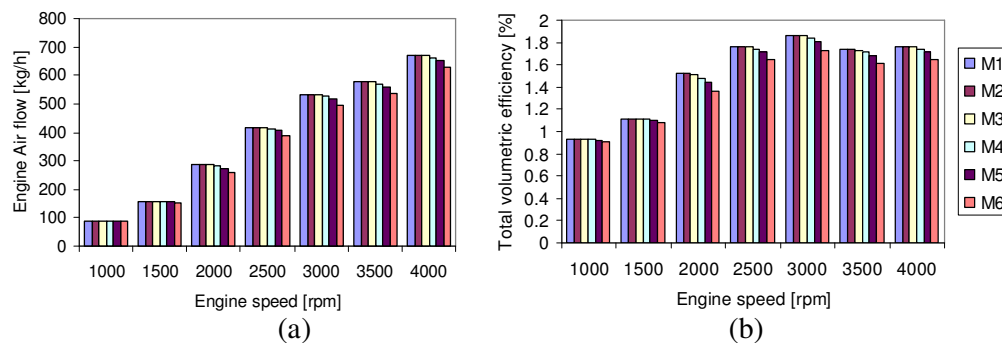


Figure 5.11 Breathing performance (a) Engine air flow; (b) Total volumetric of the engine under varies intake pressure

Throttling the air flow in the air intake manifold increases the pressure drop. Figure 5.11(a) shows the intake port static pressure decreased when the air flow is throttled which reduces the air flow at all engine speeds. The pressure drop is increased as the engine speed is increases. However, at low engine speed between 1500rpm to 1000 rpm, the engine air flow did not change as the VPA changes. This is due to the low pressure drop when the volume flow rate is low.

Figure 5.11(b) shows the correlation between intake port static pressure and volumetric efficiency. The figure shows that the total volumetric efficiency reduces as intake port static pressure reduces in all engine speeds. Total volumetric efficiency is increased as the engine speed increases from 1000 rpm to 3000 rpm and slowly reduces towards 4000 rpm. The volumetric efficiency is a measure of the effectiveness of the air intake system. Total volumetric efficiency is defined as the volume flow rate of air into the intake system divided by the rate at which the volume is being displaced by the piston. The typical value of volumetric efficiency for natural aspirated engines is between 70% and 85% (Heywood 1988). Meanwhile for the turbocharged engines, the volumetric efficiency is more than 100%.

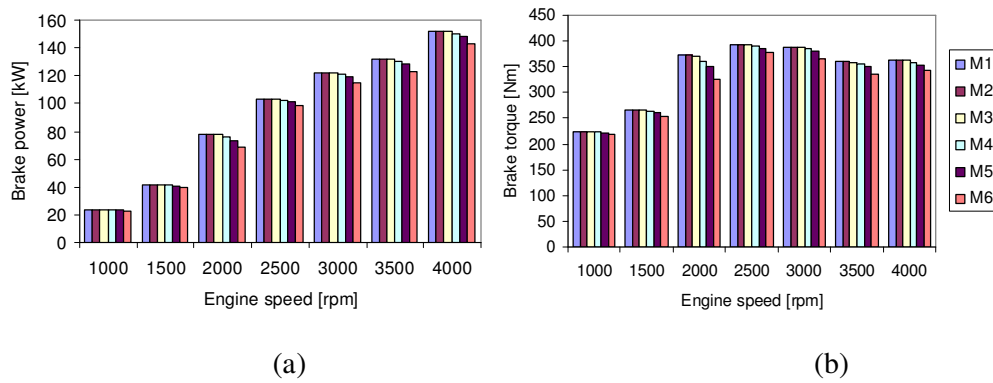


Figure 5.12 Engine performances as a function of engine speed, (a) engine brake power, (b) engine brake torque

The brake power is directly linked to the intake pressure. Figure 5.12(a) shows that the brake power reduces as the intake pressure reduces. Again, at 1000 rpm, the brake power remains at the same level even though the intake pressure reduces. Figure 5.12(b) shows engine brake torque at full load with variable intake pressure. The engine brake torque reduces as the intake pressure reduces at all engine

speeds. The maximum of brake torque is achieved at engine speed of 2500 for all engine test modes. The brake torque is found to drop significantly at 2000rpm. The drop of intake pressure from 1.6145 bar to 1.4687 bar reduces the brake torque from 372.2 Nm to 326.9 Nm.

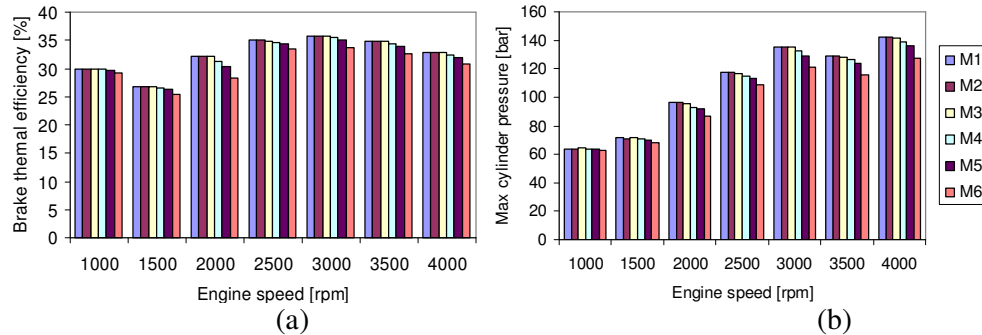


Figure 5.13 Engine performances as a function of engine speed. (a) Brake thermal efficiency and (b) maximum of in-cylinder pressure

Figure 5.13(a) presents the brake thermal efficiency for all test conditions. The brake thermal efficiency clearly increases as intake pressure increases at all engine speeds. At engine speed of 2000rpm, the thermal efficiency drop significantly when the intake pressure decreases. The intake pressure dropped by 9.0289% from 1.6145 to 1.4687 bar resulted in the drop of brake thermal efficiency from 32.14% to 28.23%. The peak of brake thermal efficiency occurred at an engine speed of 3000 rpm and the lowest at 1500 rpm. Figure 5.13(b) shows the maximum of in-cylinder pressure occurred in the engine cylinder at all test conditions. The maximum in-cylinder pressure peak occurred at the highest engine speed of 4000 rpm. In general, the maximum of in-cylinder pressure reduced as intake pressure reduces except for the engine speed of 1500 rpm and 1000 rpm. This is perhaps due to the effect of turbocharger where at low engine speed the compressor speed is low and therefore the

boost pressure is lower. As a result, less fuel is injected into the engine cylinder which produces lower of in-cylinder pressure. The maximum in-cylinder peak pressure occurred at mode 3 (M3) where the intake pressure was recorded as 71.36 bar and 64.09 bar at 1500 rpm and 1000 rpm respectively.

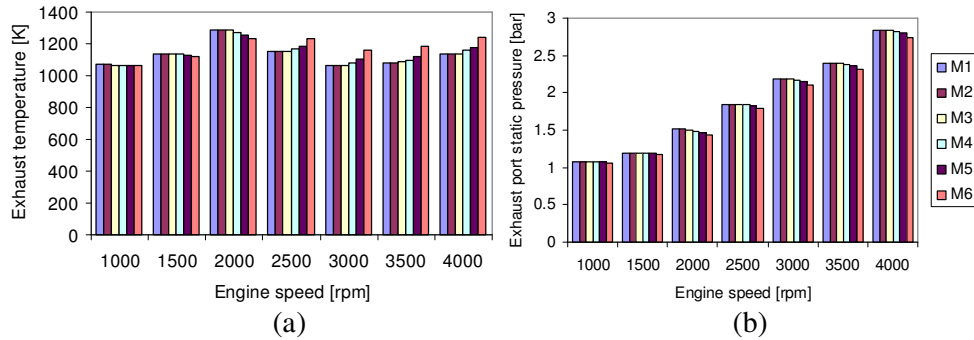


Figure 5.14 Exhaust properties (a) Exhaust gas temperature and (b) exhaust port static pressure

Figure 5.14(a) shows that at high engine speed, the exhaust gas temperature is higher when the intake pressure is reduced. While at low engine speed (less than 2000 rpm), the exhaust gas temperature reduces or remains level when the intake pressure reduces. Figure 5.14(b) shows the reaction of exhaust port static pressure (EPSP) resulting from the change of intake pressure and engine speed at full load conditions. In general, it shows that the EPSP is reduced as the intake pressure reduces. The exhaust pressure clearly reduces when the engine speed reduces, as can be expected.

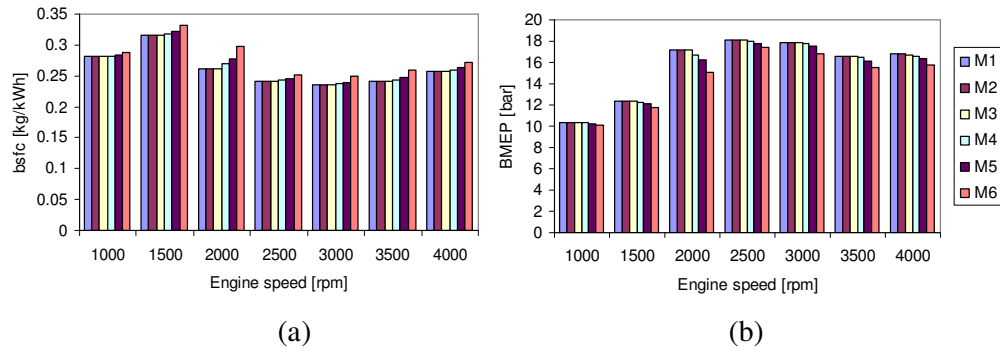


Figure 5.15 Engine fueling and pumping performance (a) bsfc (b) brake mean effective pressure

Figure 5.15(a) presents the brake specific fuel consumption at all test conditions. The graph shows that the intake pressure is proportional to the bsfc. The worst case is recorded at an engine speed of 1500 rpm when the valve plate angle was 20 degrees. The intake port pressure drops 3.22% from 1.2252 bar to 1.1857 bar when the valve plate angle reduces from 90 degrees to 20 degrees. Figure 5.15(b) shows the BMEP of the engine, which is affected by the intake port shown by the graph. The BMEP reduces as the intake pressure reduces. The patterns of the graph are also similar to the engine brake torque as can be expected.

## 5.4 Summary

The one dimensional simulation is used to investigate the wave action on the intake manifold of a V6 diesel engine. It is proved that the one dimensional simulation is one a good example to understand the dynamic action on the intake manifold. The simulation results agreed well with all experimental data at full load conditions. The simulation also provides excellent results on the effect of the intake manifold variable such as intake boost pressure. The simulation results were validated with experimental data. It is found that the pressure drop caused by the throttle resulted in lower engine performance and engine efficiency. The simulation results showed that at full load conditions, the brake power and brake torque reduces 7.3% and 12.2% respectively. The relative error of engine power and torque between experiment and simulation results are varies from 0.23 to 2.5% and 0.14 to 3.14% respectively. The air mass flow rate and bsfc also gives good agreement between experimental data and simulation results.

## **CHAPTER 6**

# **PERFORMANCE AND EMISSIONS OF A V6 DIESEL ENGINE OPERATING WITH BIODIESEL**

### **6.1 Introduction**

This chapter presents the engine performance and emissions of a diesel engine operating with RME and ULSD. The experimental studies were used the 2.7L V6 engine. Section 6.2 and 6.3 discussed the details of the effect of fuel, brake torque and fuel temperature on the engines performance and emissions level. In both sections 6.2 and 6.3, the results are with respect to the engine operated without EGR and fuelled by 100% RME and ULSD for comparison. The experiments have been conducted on two different brake torques conditions. The effect of the EGR mode on all of the above conditions has been discussed in detail in section 6.4

## 6.2 Engine Test Conditions

The objective of the study is to investigate the performance of a V6 diesel engine operating with RME. The experiments have been conducted at two different engine loads named low load and part load. The comparisons have been made with the case of operation with ULSD. The engine is used to operate with and without the EGR system. The engine operating conditions are summarised in Table 6.1.

Table 6.1 Engine operating conditions

Test mode	Fuel type	Engine speed (rpm)	Load (Nm)	BMEP (bar)	EGR mode
6.1	RME	1550	67	3.1	0
6.2	RME	1550	102	4.7	0
6.3	RME	1550	67	3.1	1
6.4	RME	1550	102	4.7	1
6.5	ULSD	1550	67	3.1	0
6.6	ULSD	1550	67	3.1	1

These two engine conditions (low load and part load) are chosen from the 16 test points which are extracted from the NEDC (New European Driving Cycle). All of these 16 test conditions were previously used to determine the official fuel economy (CO<sub>2</sub>) figures and to ensure that the emission's regulations are met for the engine (Chuepeng 2008). Figure 6.1 shows the details of the operating conditions as recommended by the NEDC. Mode 8 and 9 from the tabulated map is used to carefully study the performance and emissions of a V6 diesel engine operating with biodiesel. Furthermore, similar conditions are used to study the effect of air intake parameters on the performance of the engine operating with RME as discussed in detail in Chapter 7.

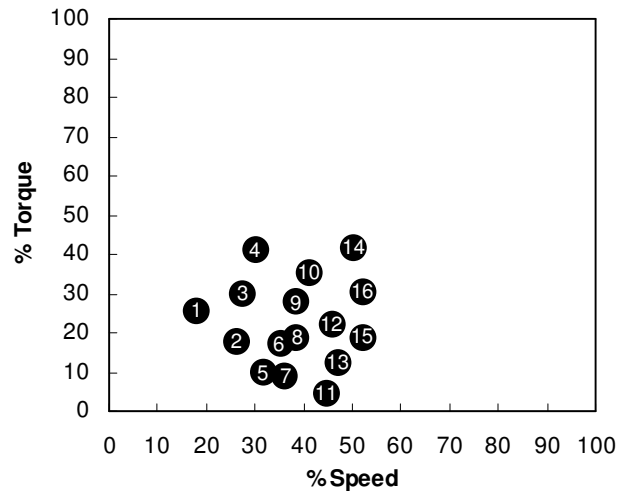


Figure 6.1 The 16 test operating conditions from NEDC (Chuepeng 2008).

The engine calibration is fully controlled by the EMS. No modifications made on the engine. Both ULSD and RME are loaded into two different fuel tanks where the valve is used to switch between the fuels. However, the fuel contains in the fuel line was blown away before the new fuel was replaced. The EGR ratio is fully controlled by the EMS. However, the EGR operation is easily turn ON and OFF by INCA software. There are some parameters are externally controlled such as fuel temperature, boost temperature and engine oil temperature.

### 6.3 Engine Testing at Low Load and Part Load

The engine is used to operate under standard conditions without any modification on the engine mapping. Therefore, the use of RME is definitely giving a different response on all test conditions. The observation on engine response is crucial to have a better understanding on the engine behaviour. Figure 6.2 shows the excess air ratio and fuel injection pressure as a consequence of EGR and engine load.

The results clearly show the engine strategy plays an important role in order to gain required power. Figure 6.2 (a) shows that the lambda is 56% lower at part load as compared to lower load. Apparently EGR has lowered the lambda for both part load and low load.

At any specific engine speed, the diesel engine was operated with constant air flow rate. Therefore the lambda is changed by changing the amount of fuel injected into the engine cylinder. The effect is observed by the fuel injection pressure as demand parameter. Figure 6.2 (b) shows the injection pressure in a common rail system. It clearly shows that mode 6.2 and 6.4 demand higher injection pressure to provide more fuel into the engine cylinder. The higher injection pressures are also observed when the engine is operating with EGR. More fuel is injected when the engine is operating with EGR to gain equal brake torque and engine speed. As reported by many researchers on the EGR system where the engine power is slightly dropped when the same amount of fuel is injected on a diesel engine operating with the EGR system (Husberg et al. 2004; Zheng et al. 2004).

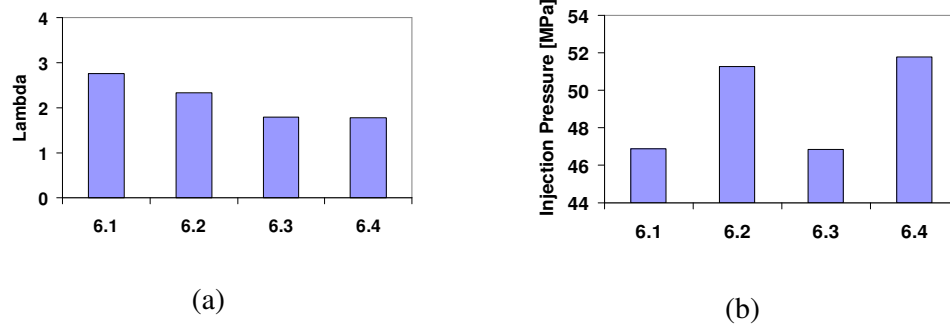


Figure 6.2 Characteristic of fueling against test mode (a) Air excess ratio, (b) fuel injection pressure

The injection strategy plays a vital role in modern diesel engines. The pilot and main injections vary according to engine speed and engine load. Figure 6.3 clearly shows the injection strategies for all the test conditions. At low load (mode 6.1 and 6.3), the pilot injection took place at -17.5 CAD BTDC and the start of main injection at 2.06 CAD ATDC. At part load (Mode 6.2 and 6.4), with the demand of higher brake torque, more fuel and advanced injection are needed. It is clear that the injection timing for pilot and main injection advanced by 1.5 CAD and 1.0 CAD as compared to the low load. The EGR operation also gives an effect to the injection strategy especially at part load. The injection timing is advanced by 0.3 CAD at part load but is almost not change at low load, where the EGR is used.

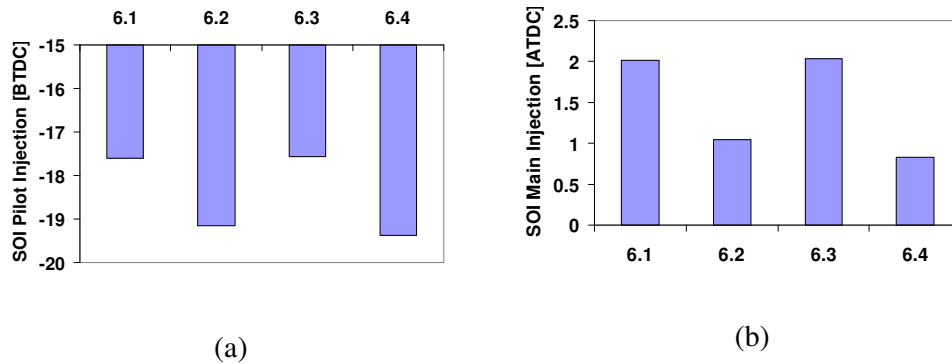


Figure 6.3 Characteristic of injection (a) Start of injection for pilot, (b) main injection

Figure 6.4 (a) shows the brake specific fuel consumption of the engine operating with RME. The bsfc is lower at part load (mode 6.2) regardless of EGR operation than at low load (mode 6.1). In general, the bsfc is slightly higher when the engine is operating with EGR. Figure 6.4 (b) shows the engine efficiency for all four operating modes. The engine efficiency is higher at part load (mode 6.2 and 6.4). It also shows that the EGR has slightly lowered the engine efficiency for mode 6.3 and

#### 6.4.

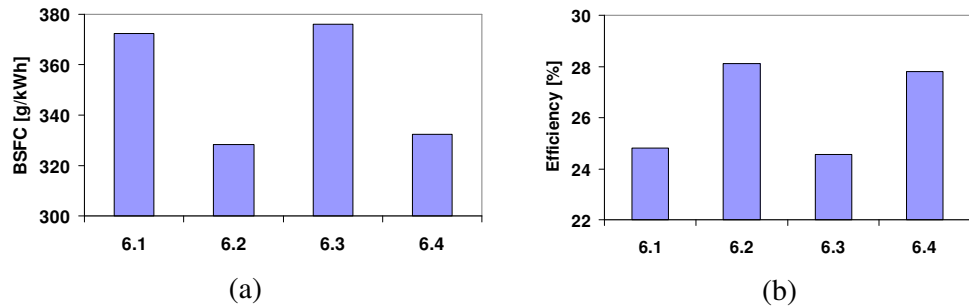


Figure 6.4 Engine performance (a) brake specific fuel consumption, (b) engine thermal efficiency against test mode

The engine was equipped with common rail fuel injection which has two fuel injection events for each combustion stroke. Therefore, double peak of in-cylinder pressure are prominent the in-cylinder pressure history. It clearly shows that the progress of in-cylinder pressure between low load and part load is different especially on the second fuel injection. At part load, the advanced of fuel injection as well as the amount of fuel injected gives different progress as clearly observed. Figure 6.6 shows that the peak pressure is decreased as the EGR is used. Figure 6.5 also shows that the EGR has retarded the start of combustion and thus resulted in an increase in the ignition delay. This led to a drop in the peak pressure. The EGR is once again influenced the start of combustion for the main injection where the start of the second combustion was clearly retarded. This resulted in an increase in the peak pressure as compared to the case of without EGR. It is well documented by a previous study that the circulation of exhaust gas resulted to increase the ignition delay which is shown by the late progress of the in-cylinder pressure rise (Zheng et al. 2004).

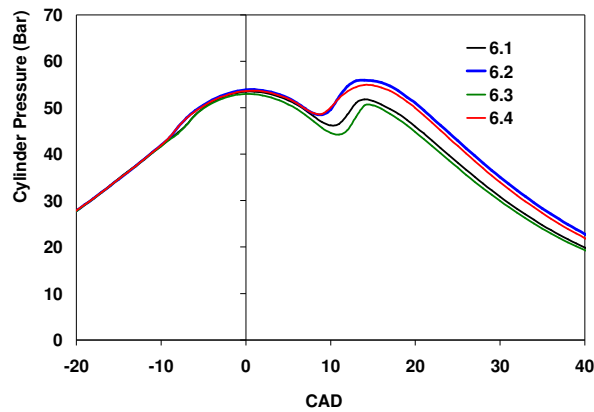


Figure 6.5 In-cylinder pressure profiles against crank angle degree

Figure 6.6 shows the emissions of NO<sub>x</sub> as a function of engine load and EGR operations. As expected, that the NO<sub>x</sub> formation is higher when the engine operated at part load as compared to low load. The formation of NO<sub>x</sub> is clearly a function of peak pressure. This is a consequence of higher combustion temperature when the higher peak pressure occurred. Figure 6.6 shows that the EGR has lowered the exhaust NO<sub>x</sub> by more than half at both low load and high load. This suggested that the formation of NO<sub>x</sub> is highly influenced by combustion pressure and temperature as discussed in detail by many others. The thermal NO formations are strongly depending on the combustion gas temperature and oxygen concentration as explained in detail by Zeldovich mechanism (Williams 1985; Glassman 1987). Thus, the application of the EGR system has successfully diluted the intake air and at the same time reduces the combustion temperature.

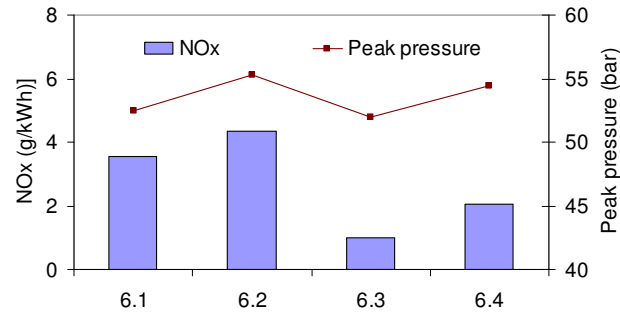


Figure 6.6 Emission of NOx and a comparison with peak pressure as a functions of test mode.

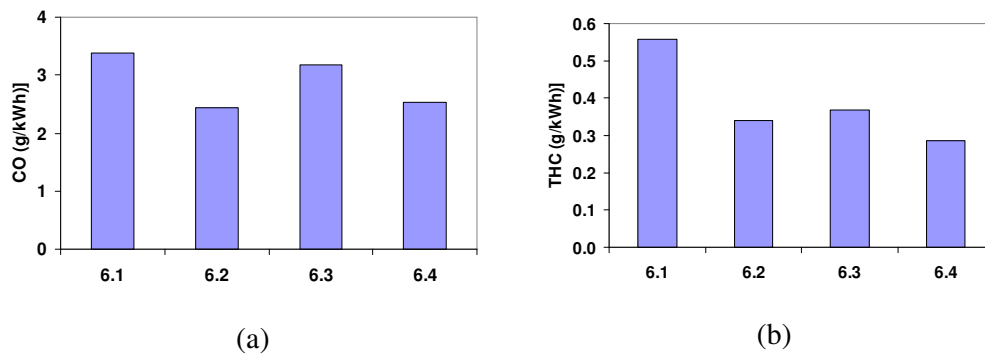


Figure 6.7 Exhaust emission (a) carbon monoxide, (b) total hydrocarbons

Figure 6.7 (a) and (b) illustrate the exhaust emissions of carbon monoxide (CO) and total hydrocarbon (THC) respectively. The formation of CO is highly influenced by engine load but less sensitive to EGR. At part load, the formation of CO is 41.7% lower as compared with the low load. It is found that in these particular test conditions, no significant relation between the formation of CO and EGR operations occurred. Meanwhile, the THC is reduced when the engine operated at part load as compared with low load. It is found that the formation of THC is significantly reduced when the EGR is used.

#### **6.4 Diesel Engine Operating with RME and ULSD**

The diesel engine operating with biodiesel advanced the injection timing especially in a pump-nozzle fuel injection system as reported by many others (Szybist et al. 2003; Labeckas et al. 2006; Tsolakis et al. 2007). This is due to rapid transferred of the pressure wave traveling from the fuel injection pump to the fuel injection nozzle resulted in early opening of the fuel injector (Szybist et al. 2007). The pressure wave travel speed is higher for RME is due to a higher bulk modulus of compressibility, and consequently a higher speed of sound in the biodiesel relative to diesel fuel (Szybist et al. 2007). This result in the increase of in-cylinder peak pressure and therefore increases the NO<sub>x</sub> emission.

However, recent research on a common-rail diesel engine which operating with biodiesel also reported that the advanced of injection timing occurred (Tat 2003; Chuepeng 2008). The electronic control unit in a common-rail fuel injection also contributes to the advanced injection when using biodiesel. This is due to the accelerator overpressing which is required to compensate the lower of the biodiesel's low heating value (Tat 2003). The objective of this experiment is to study the difference between RME and ULSD in terms of engine performance and exhaust emissions.

The in-cylinder pressure for two different fuels was investigated in the diesel engine operating with and without EGR. The engine was operated at a constant engine speed of 1500rpm and with a load of 3.1bar BMEP. The fuel temperature for both ULSD and RME was kept constant at 40°C. Figure 6.8 shows cylinder pressure and the rate of heat release for ULSD and RME. The results show that the peak

pressure for RME is higher than that obtained with ULSD. The data recovered from the engine ECU showed that the pilot injection of RME was advanced by 0.4 crank angle degrees compared with injection of ULSD. Early injection for RME resulted in an early start of combustion which produced higher cylinder pressure as clearly depicted in Figure 6.8.

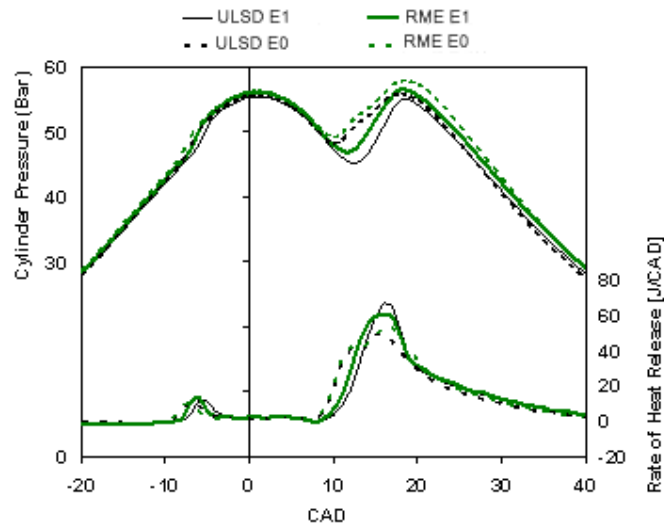


Figure 6.8 Cylinder pressure and rate of heat release for ULSD and RME at engine speed of 1550rpm, 67 Nm brake torque.

The combustion pattern is strongly influenced by the EGR operation. The cylinder pressure decreases as the EGR system is engaged for both ULSD and RME. In addition, the start of combustion is retarded by 3.5 and 3.6 crank angle degrees for ULSD and RME respectively when the engine is operating with EGR. Both of these effects contribute to lower peak pressures and temperatures in the combustion chamber. As a consequence, the rate of heat release starts to increase faster and tends to decrease earlier compared with the case without EGR. This trend is similar for both the pilot as well as main injections.

Figure 6.9 shows the ignition delay and in-cylinder peak pressure for ULSD and RME fuelling. It shows that the ignition delay is slightly decreased when the engine is fuelled by RME. Previous research on a single cylinder pump-line-nozzle diesel engine has shown that the higher bulk modulus of RME causes an early injection event (Tsolakis et al. 2007). However, research conducted by Chuepeng and Tat also concluded that the advanced injections occurred on a common-rail diesel engine operating with biodiesel (Tat 2003; Chuepeng 2008). This is due to the accelerator overpressing which is required to compensate the lower of the biodiesel's low heating value (Tat 2003). These events result in the increase of in-cylinder pressure and the heat release rate in the initial pre-combustion phase. Figure 6.12 also reveals that when the engine operating with EGR, the ignition delay increases for both fuels. This is a consequence of the increase of fuel and air mixing time in the combustion chamber, which is necessary before the auto-ignition begins. The in-cylinder peak pressure is reduced for both RME and ULSD when the EGR is introduced into the intake manifold.

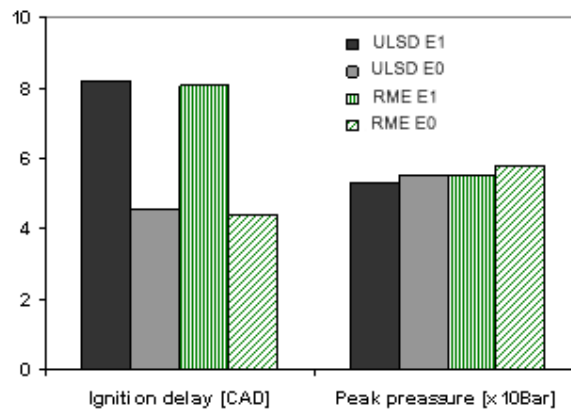


Figure 6.9 Ignition delay and peak pressure for ULSD and RME at engine speed of 1550rpm.

Further analysis of emissions shows that the NO<sub>x</sub> emissions are slightly higher for RME as compared with ULSD. This is attributed partly to the effect of advanced injection due to accelerator overpressing in a common-rail injection system (Tat 2003). The same result was also reported by Senatore where the measurement of both instantaneous injection pressure and injector needle lift showed a greater advance in the fuel injection process when biodiesel was used (Senatore et al. 2000).

Figure 6.10 shows that the EGR is a very effective tool to reduce NO<sub>x</sub> emissions. It can be seen that these emissions are up to 3 times lower when EGR is engaged, for both RME and ULSD. Figure 6.10 also reveals that the combustion of RME produces nearly three times lower emissions of unburned hydrocarbons as compared with ULSD. However, when EGR is switch off, the total emissions of unburned hydrocarbons are reduced for ULSD but greatly increased by 52% for RME. The emission of CO is highly reduced by 198.8% for the engine operating with ULSD as compared with RME where the CO is slightly increased by 6%.

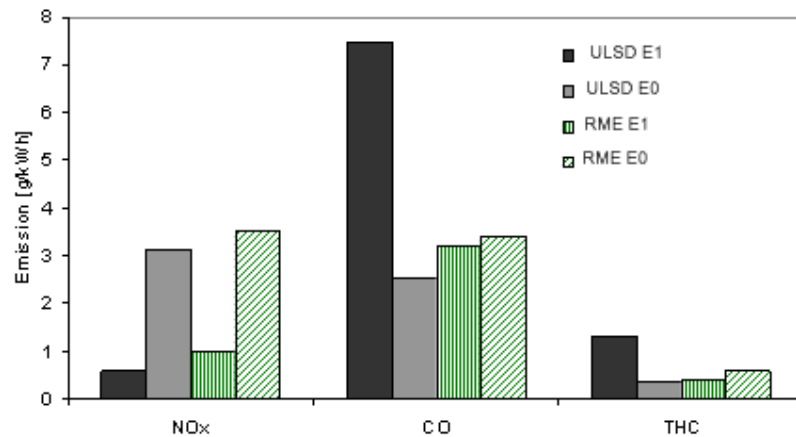


Figure 6.10 Emissions of NO<sub>x</sub> and THC for ULSD and RME fuelling at engine speed of 1550rpm

Figure 6.11 shows NO<sub>x</sub>-PM trade-off when the engine was fuelled with ULSD and RME. The particulate emissions were measured with a Bosch smoke meter. It was demonstrated that with the engine running at 1550 rpm and 67Nm brake torque (3.1 bar BMEP), with EGR engaged, fuelling with RME reduced the smoke by 36.5% compared with ULSD. However, when the engine was operating without EGR the PM was reduced by 40% on replacement of ULSD by RME. The engine operating with RME produces low PM as compared with ULSD due to the oxidation of the PM where the sufficient local oxygen was present to oxidize the PM before it left the cylinder (Husberg et al. 2004; Labeckas et al. 2006).

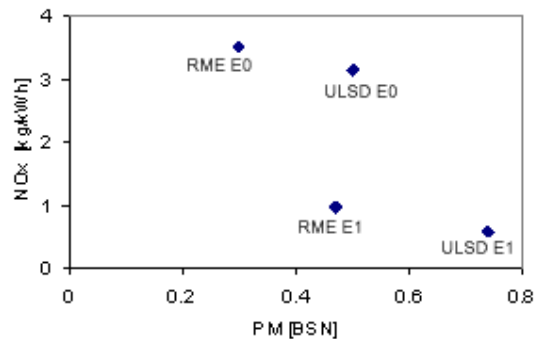


Figure 6.11 NO<sub>x</sub> – PM trade-off, the engine running at 1550 rpm, 3.1 bar BMEP

## 6.5 Effect of Fuel Temperatures

The modification of fuel properties, such as density, by changing the fuel temperature is relatively easy to perform on a diesel engine. Much research has been conducted on the effect of fuel temperature on diesel engines (Nwafor 2003; Nwafor 2004). Bialkowski has conducted research on the effect of rapeseed oil temperature

on common rail fuel injector spray behaviour. He concluded that the higher the fuel temperature, the faster spray penetration and smaller Sauter and arithmetic mean diameter (Bialkowski et al. 2004). Therefore by changing the fuel physical conditions, it could possibly reduce the gap between the performance of biodiesel and mineral diesel fuels.

The objective of the present work is to study the effect of biodiesel fuel temperature on the combustion and emissions of a diesel engine. The standard engine calibration and operation is not altered during the experiment. However, the operation of EGR is switched ON and OFF to study the effect of EGR on engine performance and emissions level. The temperature of RME is varied and tested at 30, 35 and 40°C. The fuel temperature is changed by the heat exchanger which is installed 500mm from the fuel pump. The fuel line between the heat exchanger and fuel pump is insulated to prevent heat losses. The fuel temperature is carefully controlled by a solenoid valve which controls the volume flow rate of cooling water.

The engine operations parameter and responses triggered from the ECU were recorded and analysed in order to obtain a better understanding of the engine reaction on the effect of fuel temperature and EGR operations. Figure 6.12 shows the responses of injection pressure in the engine as a consequence of changes in EGR mode and fuel temperature. It is found that the higher fuel temperatures tend to produce higher injection pressure. When the fuel temperature is increased, the fuel density decreases. Therefore, a higher injection pressure is required to gain an equal fuel mass in order to produce the same required brake torque.

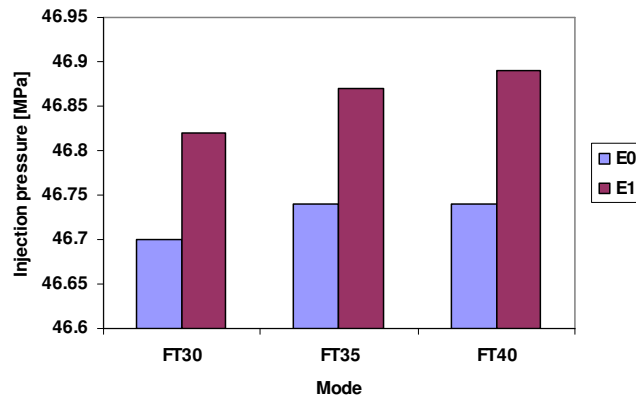


Figure 6.12 Response of injection pressure in the engine as a consequence of EGR mode and fuel temperature. E1 and E0 represent the EGR mode ON and OFF respectively.

The fuel mass flow rate was slightly decreased when the fuel temperature changed from 30°C to 40°C. This occurred due to lower fuel density as the fuel temperature increased. The engine consumed 1.5% more RME when it was operating with EGR as compared to the engine operating without EGR. This is due to the test condition which is conducted at identical brake mean effective pressure (BMEP). Furthermore, a delay of start of combustion occurred when the engine was operating with EGR. Therefore, more fuel is injected to achieve the required brake torque. Previous studies (Husberg et al. 2004; Zheng et al. 2004) show that the engine power is slightly decreased for the same amount of fuel injected when engine is operating with the EGR.

The data recorded by the ECU shows that with the EGR of 32%, the air excess ratio used for producing the same load is 55% lower than in the case of without EGR. When the fuel temperature increases from 30 to 40°C, the air access ratio is not changed regardless of EGR operation.

The engine was using the common rail fuel injection system and operated with two fuel injection events in every combustion cycle. The double peak of in-cylinder pressure is clearly observed on the in-cylinder pressure history plot. It is found that the first injection (pilot injection) took place at 17.5 CAD BTDC and the start of main injection was timed at 2.06 CAD ATDC. The maximum peak pressure occurred after the first injection due to premixed combustion.

Figure 6.13 shows that the EGR retarded the start of combustion thus resulted in a longer ignition delay and resulted in lowering the peak pressure. It will be shown later in Figure 6.15 that the pressure of combustion in the engine cylinder is affected by the fuel temperature.

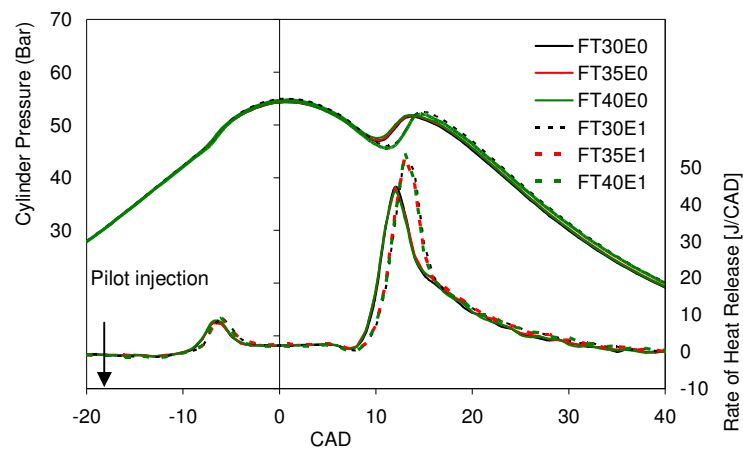


Figure 6.13 In-cylinder pressure and rate of heat release for three different fuel temperatures.

The ignition delay is increased when the fuel temperature increases for both engine test conditions with and without the EGR. This is due to the lower viscosity and density of RME at higher temperature. Therefore, the RME evaporates soon after

the ignition takes place. The immediate vaporisation of RME causes the reduction in the fuel penetration. This is due to lower kinetic energy for the gaseous fuel as compared with the fuel droplet. The results show a good agreement with results of Kubota et al (Kubota et al. 2002) obtained on a single cylinder diesel engine fuelled with mineral diesel. He also observed that the ignition delay is extended as the fuel temperature increases. In addition, the increase of fuel temperature results in a decrease of the arithmetic mean diameter of the fuel droplets. This is due to the effect of surface tension and viscosity changes with temperature as explained in detail in the literature (Bialkowski et al. 2004).

Figure 6.14 shows that the maximum in-cylinder pressure decreases when the fuel temperature increases. This phenomenon is clearly observed in the case of the engine operating without the EGR. This is a consequence of longer ignition delay when the fuel temperature is increased. The data recovered from the ECU has confirmed, as expected, that without EGR, even when the pilot injection is started at same time, the start of combustion occurs earlier than in the case with EGR. The increase of fuel temperature seems to have led to a similar effect in terms of maximum in-cylinder pressure

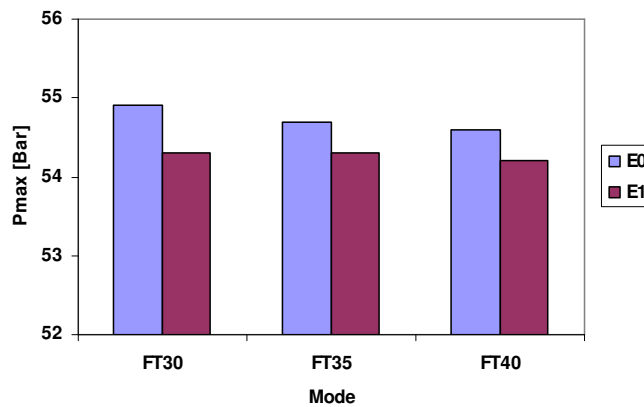


Figure 6.14 Maximum of in-cylinder pressure with three different fuel temperatures

Figure 6.15 shows the close-up view of the in-cylinder pressure history for the main injection event. It shows that the second peak pressure is also decreased as the fuel temperature increases. The EGR once again influenced the start of combustion for the main injection where the start of second combustion was clearly retarded. This resulted in an increase of the peak pressure as compared with the case of zero EGR. It is well documented in the literature that the recirculation of exhaust gas results in an increase of the ignition delay and shows in the late progress of in-cylinder pressure rise (Zheng et al. 2004).

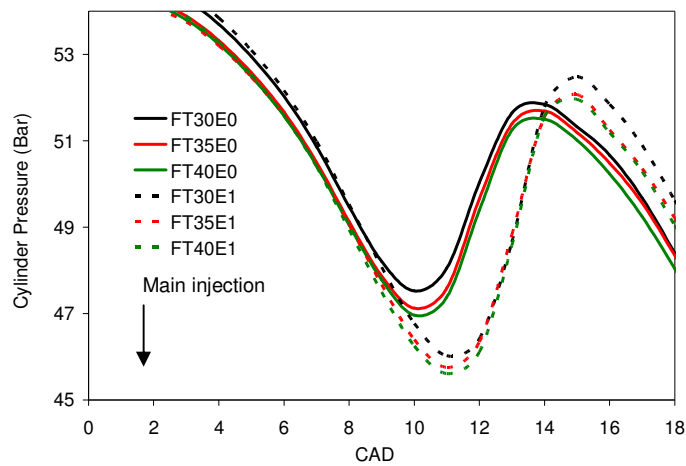


Figure 6.15 Close-up view of in-cylinder pressure during the main injection period.

Figure 6.16 shows that the EGR retards the start of combustion, thus directly increases the ignition delay. The heat release is retarded at every crank angle degree where the peak of heat release rate is at 7.0 CAD BTDC and 6.0 CAD BTDC for the cases of without EGR and with EGR respectively.

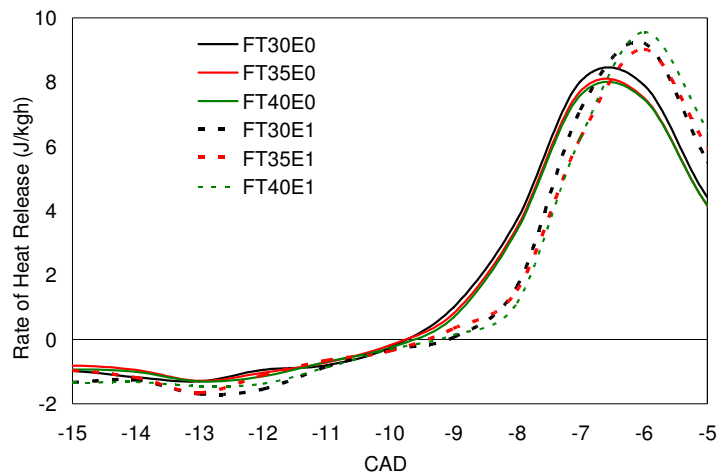


Figure 6.16 Close-up view of rate of heat release during premixed combustion.

It clearly shows that the combustion event is slightly retarded when the EGR is used. In these test conditions, the start of combustion occurred 2 degrees later when the engine was operated with 32% of EGR. When the fuel temperature was increased, the combustion progresses were retarded. This is a consequence of the delayed start of combustion as mention earlier. The higher fuel temperature also results in an increase of fuel evaporation and reduced Sauter Mean Diameter (SMD) of fuel droplets. This phenomenon is well documented and can be found in many research reports (Araneo et al. 2000; Bialkowski et al. 2004).

Figure 6.17 shows the brake specific fuel consumption of the engine operated with RME. In general, the bsfc is higher when the engine operates with EGR. The difference of bsfc between both cases (EGR ON-OFF) is even higher when the fuel temperature increases. The bsfc is clearly improved as the fuel temperature increases when the engine is running without an EGR system. It can be reasoned that the bsfc is improved due to a better evaporation process resulting in a complete combustion.

However, when the engine was operated with EGR, the bsfc is not affected by the increases of fuel temperature.

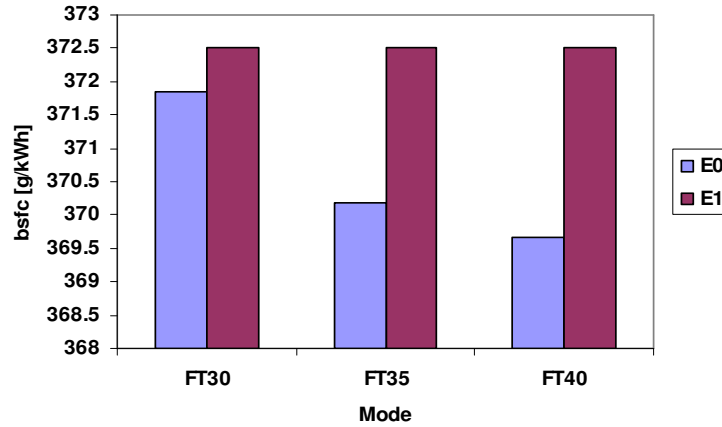


Figure 6.17 Brake specific fuel consumption

Figure 6.18 shows the engine efficiency for all tested operating modes. It clearly shows that the EGR has lowered the engine efficiency at all fuel temperature conditions. The efficiency is improved when the fuel temperature increases. However, when the engine was operated with EGR, the engine efficiency is not affected by the 10°C difference of fuel temperature.

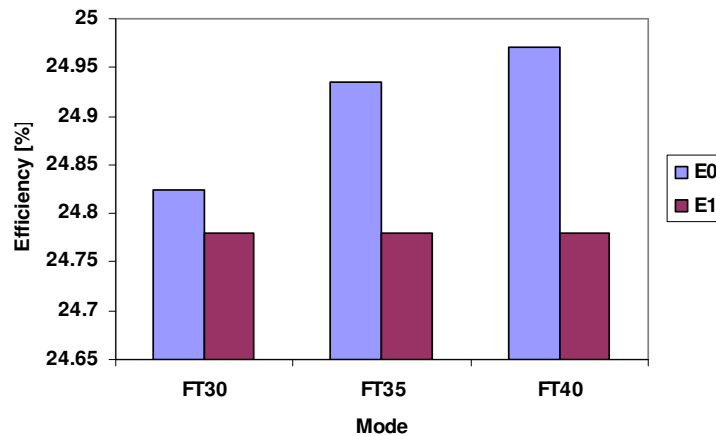


Figure 6.18 Engine efficiency

When the exhaust gas is used to replace a certain amount of fresh air charge into the cylinder, the local oxygen concentration in the engine cylinder is reduced. Therefore, the injected fuel will have to diffuse over a wider area before sufficient local oxygen is encountered for a combustible mixture to be formed. The charge mixture does not only contain the mixture of air and fuel, but also an additional quantity of exhaust gases which contain large quantities of CO<sub>2</sub>. The additional amount of these gases absorbs energy released during the combustion, leading to poor thermal efficiency (Abd-Alla 2002).

Figure 6.19 shows the exhaust emissions of oxides of nitrogen (NO<sub>x</sub>) as a function of fuel temperature and EGR operations. It is found that the EGR has lowered the exhaust NO<sub>x</sub> by more than half at any fuel temperatures. When the engine is running without EGR, emissions of NO<sub>x</sub> are reduced as the fuel temperature increases. However, Figure 6.19 also shows that when the engine was operated with 32% of EGR, the increase of fuel temperature from 30°C to 35°C resulted in an increase of the emissions of NO<sub>x</sub>. The emissions of NO<sub>x</sub> is reduced when the fuel temperature is increased to 40°C due to slightly lower peak pressure in the engine cylinder as depicted in Figure 6.14. The trend of NO<sub>x</sub> formation is closely related to maximum pressure in the combustion chamber. This suggests that the formation of NO<sub>x</sub> is highly influenced by combustion pressure and temperature as discussed in detail by many other investigators. The most popular theorem on the formation of NO<sub>x</sub> by the Zeldovich mechanism also suggests that the production of NO<sub>x</sub> is increased when high temperature combustion occurs (Williams 1985; Glassman 1987).

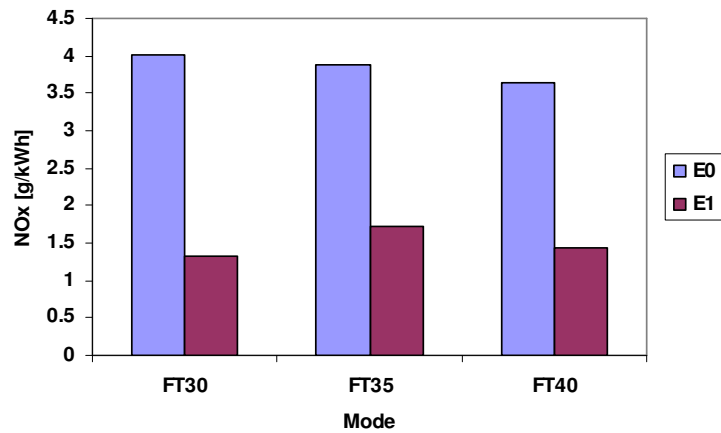


Figure 6.19 Emissions of NOx

Figures 6.20 and 6.21 show the exhaust emissions of carbon monoxide (CO) and total hydrocarbon (THC) respectively. In general, the EGR operation has increased the formation of CO by 28%. It is found that the formation of CO is generally not affected by the fuel temperature in both cases of EGR mode (EGR ON and OFF). Figure 6.21 shows that when the engine is operating without the EGR, THC emissions are almost level regardless of the fuel temperature. However, when the EGR is used, THC emissions increase slightly when the fuel temperature increases.

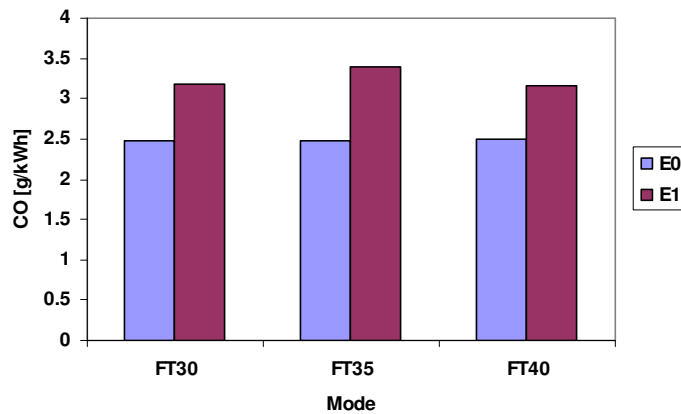


Figure 6.20 Emissions of CO in the exhaust gas as a function of fuel temperature

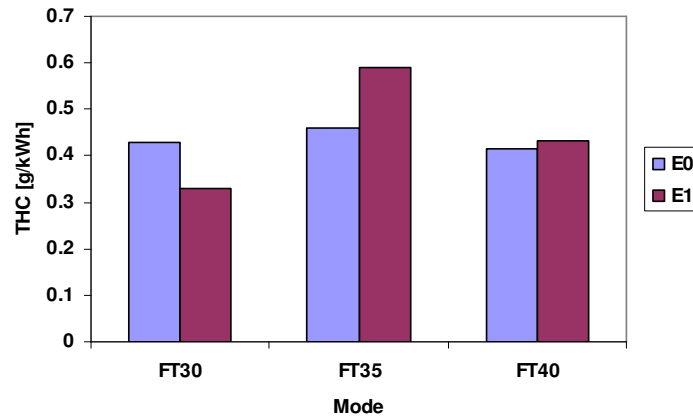


Figure 6.21 Emissions of THC in the exhaust gas as a function of fuel temperature

It has also been found that at fuel temperature of 30°C, THC<sub>s</sub> are lower for the case with EGR as compared to the case without the EGR. However, when the fuel temperature is 35°C or higher, the formation of THC<sub>s</sub> is higher for the case of EGR ON compared to the case with the EGR OFF. Local reaction temperatures decrease when the EGR is used due to the lack of locally available oxygen. Thus, oxidation of combustion residuals during diffusive combustion at high EGR levels is poor and results into the increased of CO and THC emissions (Horn et al. 2007).

## 6.6 Effect of Multiple Injections

Most of the latest diesel engines are equipped with a common-rail fuel injection system capable of multiple injections and with an EGR system. Considering all the variables together with the use of various blends of fuels, it is more complicated than ever to predict the behaviour of combustion in diesel engines. The

interest of the present study is to determine the potential of combining the use of biodiesel with high pressure multiple injections and EGR for an even larger reduction of emissions. The hypothesis is that the exhaust gas introduced to the combustion chamber could possibly influence the intake temperature and oxygen concentration around the fuel spray following both the pilot and main injections, which may be different with the diesel and biodiesel fuels. In the present study, such a comparison has been made for ULSD and biodiesel in order to investigate how this phenomenon affects the combustion quality as well as emission level.

Table 5. Parameters of injection in different modes

<b>Mode</b>	<b>Intake Manifold Pressure [kPa]</b>	<b>Fuel Injection Pressure [MPa]</b>	<b>Mode of EGR</b>	<b>Fuel Injected [mg/stk]</b>
P0E1	107.7	49.26	ON	14.33
P1E1	105.5	46.43	ON	13.35
P0E0	116.2	48.88	OFF	13.85
P1E0	116.2	46.29	OFF	12.91

The engine is tested on a standard operation where there is no change in terms of the EMS setting and mechanical parts. The EGR system is easily turned ON and OFF from the INCA software. The EMS automatically calculates the required amount of EGR based on the EGR set-point. The details of the fuel injection and intake conditions for all modes are illustrated in Table 5.

The manifold absolute pressure sensor (MAP) provides instantaneous manifold pressure information to the EMS. This measurement is used to calculate the air density in the intake manifold and determine the air mass flow rate, which in turn is used to calculate the appropriate quantity of fuel injection (Chuepeng 2008).

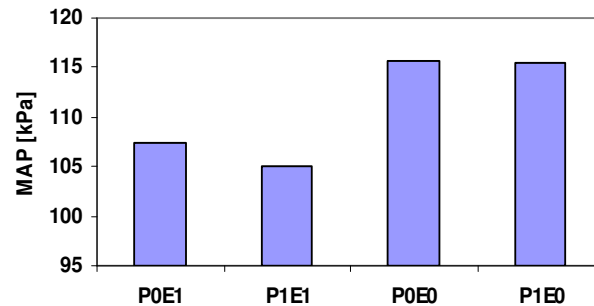


Figure 6.22 Manifold absolute pressures

It is obvious that the EGR has lowered the MAP as depicted in Figure 6.22, whereas the MAP is independent of injection strategy when EGR is not used. However, when the pilot injection is used together with EGR, the MAP is slightly dropped and this leads to an increase of EGR. Figure 6.23 shows the response of EGR when the MAP varies. In this experiment, the brake torque is kept constant at the engine speed of 1550rpm, then all the other parameters are controlled by the EMS including the EGR which is set as 37% and 46% for single injection and double injection respectively in this engine.

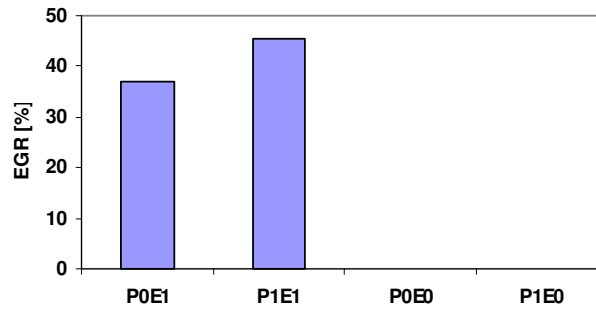


Figure 6.23 EGR controlled by the EMS

Figure 6.24 shows that the highest peak in-cylinder pressure is achieved in mode P0E0 with peak pressure of 60 bar. The other modes show similar levels with the peak pressure ranging from 54.45 bar to 55.06 bar. Meanwhile the thermal efficiency data shows that when the engine is operating with dual injection, the thermal efficiency is slightly higher regardless of EGR operations.

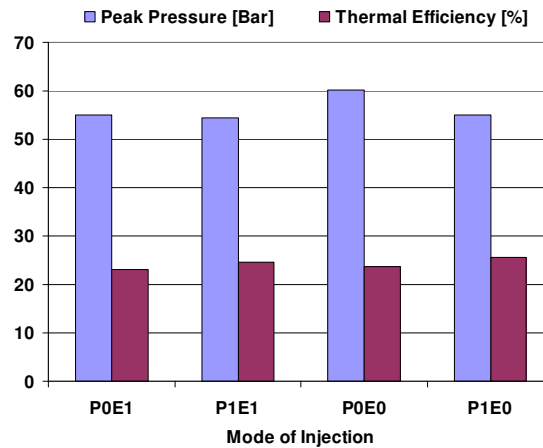


Figure 6.24 Peak pressure and thermal efficiency at different modes of injection and EGR operation

Figure 6.25 shows that the BSFC is higher for the engine operating without pilot injection. The BSFC is also higher for the engine running with EGR systems engaged. The reason for the increase in fuel consumption with EGR is probably due

to intensification of radiative losses during the expansion stroke (Egnell 2000). It is also noted that of all four modes tested, the engine operating with pilot injection but without EGR system consumes least fuel. This is consistent with the result of Yang where a 1.2-litre 4-cylinder diesel engine operated with pilot injections and low EGR consumed least fuel (Yang et al. 2002).

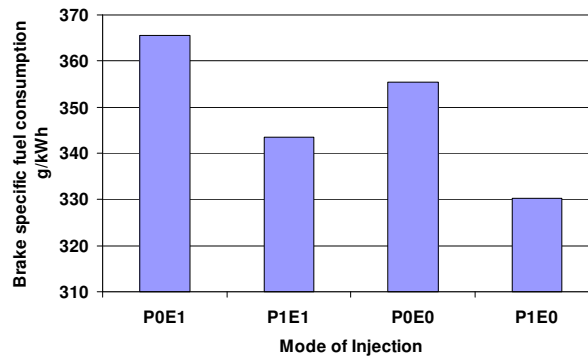


Figure 6.25 Brake specific fuel consumption at 1550 rpm, brake torque 67 Nm

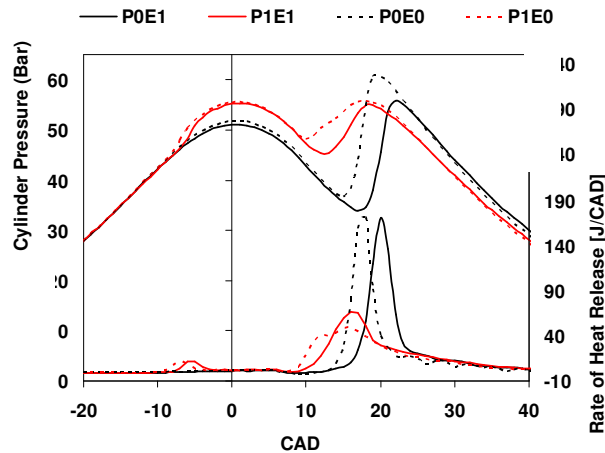


Figure 6.26 Cylinder pressure and rate of heat release at 1550 rpm, brake torque 67 Nm

Traces in Figure 6.26 demonstrate the history of in-cylinder pressure and rate of heat release for four different test conditions as shown in Table 3. The red and

black color lines correspond to the experimental tests with and without pilot injection respectively. The solid lines correspond to the tests with EGR in operation and the dotted lines correspond to the tests without EGR.

Multiple injections have a significant effect on the combustion process compared with a single injection. Pressure traces in Figure 6.26 show that the premixed combustion is nearly identical for the same injection strategy regardless of EGR operation. Heat release during the diffusion burn for single injection with EGR is retarded and rises to a sharp peak only at 20 CAD ATDC. The trend is closely associated to the combustion process where without a pilot injection, the principal combustion is mainly in the premixed mode (Maiboom et al. 2008). It can be seen that the use of dual injection strategy yields a double peak of maximum pressure of about 55 bar at near top dead centre (TDC) and 18 CAD after TDC respectively. However, the in-cylinder pressure drops early just after TDC as compared to the case without dual injections. It shows that the combustion process has slowed down early (Pierpont et al. 1995). The heat release of the double injection starts with the premix burn, and then there is a diffusion burn that starts to slow down until the second injection starts. Then, a larger diffusion burn starts and the heat release rises to a second peak and then tapers off again. The observed trend of the cylinder pressure and rate of heat release for single and dual injection are in agreement with a recent report by Maiboom et al. (Maiboom et al. 2008).

The in-cylinder pressure is slightly lower for the case of EGR especially after the main injection. This is due to the increase of ignition delay when the EGR is in operation, so that the premixed part of combustion is higher and the rate of heat release peak is lower (Ladommatos et al. 1998; Maiboom et al. 2007). It is found that

the highest peak pressure is achieved for the case without pilot injection and EGR as depicted in Figure 6.26. The graph line of pressure rise and drop suggests that the shorter ignition delay occurs and is thus responsible for the early start of combustion with the engine operating without EGR. This result is in agreement with conclusions from other researchers and can also be found in literature (Zheng et al. 2004; Maiboom et al. 2008).

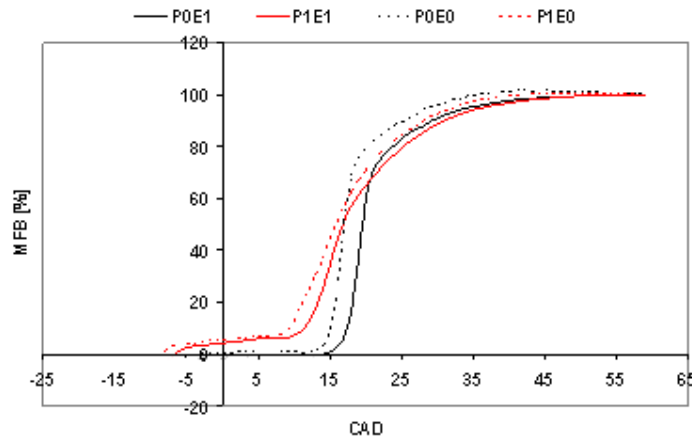


Figure 6.27 Mass fraction burn at 1550 rpm, brake torque 67 Nm

Figure 6.27 shows the MFB relative to CAD for the selected four test conditions. Compared with dual injection (mode P1E1 & P1E0), the test without pilot injection (mode P0E1 & P0E0) exhibits faster combustion in a very short period. It can be clearly seen in Figure 6.27 that the main combustion period (10 to 90% MFB) for the single injection case is very short lasting from 18 to 30 CAD ATDC. This results in a different pattern of heat release for these two cases (with and without pilot injection). Meanwhile the combustion with dual injection progresses slowly with the main combustion taking place between 11 and 31 CAD ATDC. On the other hand, comparing the mass fraction burned for the case with and without EGR, it can be seen

that the EGR affects the early combustion progress in the combustion chamber regardless of injection strategies. This is strongly related to the effect of EGR on ignition delay as discussed earlier.

Emissions of NO<sub>x</sub> formed by the combustion of fuel in an internal combustion engine typically consist of nitric oxide (NO) and nitrogen dioxide (NO<sub>2</sub>) where the nitric oxide is dominant with a small amount of NO<sub>2</sub> also present (Heywood 1988). The formation of NO<sub>x</sub> is mostly from nitrogen in the air but some liquid fuels containing nitrogen in the form of NH<sub>3</sub>, NC and HCN can also contribute to a higher potential in producing more NO<sub>x</sub> (Ganesan 2003). It is understood that this emission is highly depending on the post-combustion gas temperature, duration of gas exposure to this high temperature combustion and the species in post-combustion gases (Keating 2007).

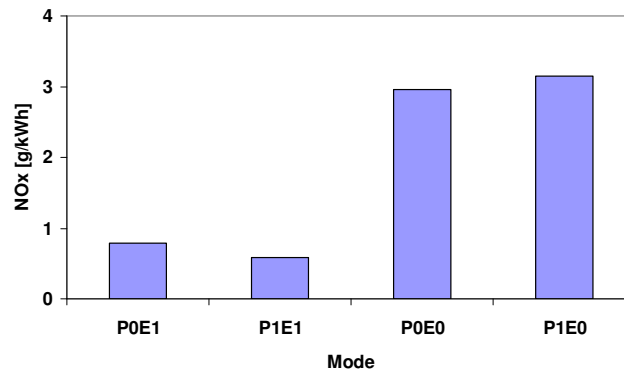


Figure 6.28 Emissions of NO<sub>x</sub> at 1550 rpm, brake torque 67 Nm

It is found that the NO<sub>x</sub> is highly dependent on EGR operations rather than on injection strategies. However, the use of dual injection with EGR contributed to additional reduction of NO<sub>x</sub> by about 15.6% as compared with the engine operation with EGR but without pilot injection. The NO<sub>x</sub> emissions are well known to be

related to the adiabatic flame temperature as discussed in literature (Heywood 1988; Cipolat 2007). The application of EGR means that the quasi-adiabatic compression process with less oxygen available results in increased ignition delay and substantially lower combustion temperature (Zheng et al. 2004). The use of pilot injection resulted in an increase of MAP as discussed earlier. This affected the rate of exhaust gas fed to the intake manifold as depicted in Figure 6.23. Therefore, this condition is clearly operated with 24.3% more EGR than the case with single injection thus contributed to a lower NO<sub>x</sub> level as shown in Figure 6.28.

Figure 6.29 shows the emissions of unburned hydrocarbons for the four different injection and EGR strategies. It is found that the unburned hydrocarbons are higher when the engine is running with EGR and without pilot injection. The use of pilot injection without EGR (mode P1E0) produces very low HC which is nearly 10 times lower than that of the mode P0E1.

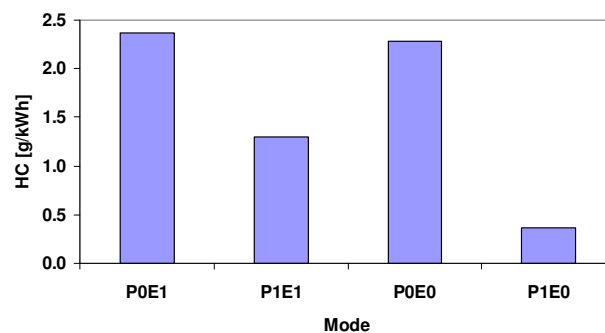


Figure 6.29 Emissions of unburned hydrocarbons at 1550 rpm, brake torque 67 Nm

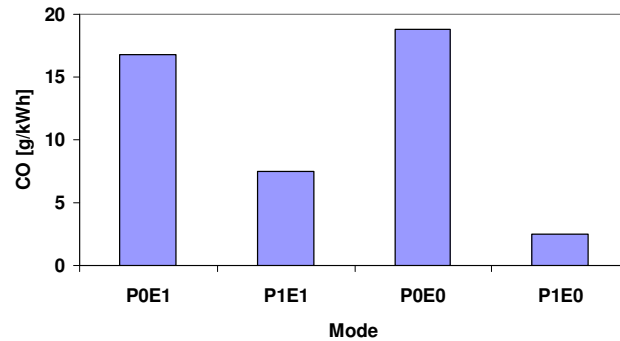


Figure 6.30 Emission of carbon monoxide at 1550 rpm, brake torque 67 Nm

The combustion degradation is clearly reflected in the smoke and CO emissions. Figure 6.30 shows the emissions of CO as a function of injection strategy and EGR operation. It is found that CO is higher when the engine is operating without EGR and pilot injection. The trend is in agreement with the poor thermal efficiency of operation. Figure 6.30 also reveals that the pilot injection strategy is very useful for reduction of the emissions of CO, whether EGR was or was not used.

As a consequence of low oxygen concentration due to EGR operation, the increased ignition delay results in lower in-cylinder peak pressure and temperature. This promotes an increase of particulate emissions as depicted in Figure 6.31. The increase of particulates is also due to retardation of injection timing as discussed in detail by Montgomery (Montgomery et al. 1996). When the pilot injection is used, PM decreases significantly regardless of EGR operation. This decrease is consistent with results obtained in other studies (Pierpont et al. 1995; Montgomery et al. 1996).

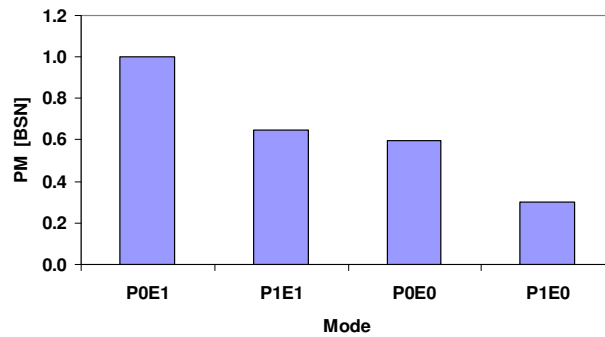


Figure 6.31 Emission of particulate matter at 1550 rpm, brake torque 67 Nm

## 6.7 Summary

The effect of EGR together with multiple injection strategy on the engine performance and emissions of a V6 diesel engine has been investigated and the conclusions can be summarized as follows.

1. The small increase of fuel temperature has reduced the viscosity as well as density of fuel. This resulted in an increase in the mixing rate of fuel during premix time, thus improving the fuel consumptions and engine efficiency.
2. The exhaust emission of NO<sub>x</sub> is slightly improved when the fuel temperature increases. Whereas CO and THC is slightly level.
3. The function of EGR is proved to have lowered the in-cylinder peak pressure and therefore reduces the NO<sub>x</sub> concentration. However, the bsfc and engine efficiency are not affected by the increase of 10°C of fuel temperature in this particular case.

4. The application of dual injection strategy without the EGR shows a significant reduction of hydrocarbon emissions but it has major drawbacks of producing higher NO<sub>x</sub>.
5. The experimental results also reveal that the pilot injection lowered the peak pressure and brake specific fuel consumption regardless of EGR operations.
6. The effect of EGR on reducing NO<sub>x</sub> emissions is more significant compared with the effect of multiple injection strategies.
7. The combination of EGR and dual injection strategies produces even better reductions in emissions, especially of NO<sub>x</sub> and particulate matter.
8. Engine operation on biodiesel produced higher in-cylinder pressures thus promoted production of higher NO<sub>x</sub> emissions but lower emissions of unburned hydrocarbons, carbon monoxide and particulate matter.

## **CHAPTER 7**

### **EFFECT OF AIR INTAKE SYSTEMS TO THE ENGINE PERFORMANCE AND EMISSIONS**

This chapter presents the study of effect of air intake characteristics such as temperature and pressure drop on the engine performance and emissions of a diesel engine. The experimental studies conducted on the 2.7L V6 engine provided by JLR. The engine was operated without EGR and fuelled by 100% RME and ULSD for a comparison, under two different brake torque conditions respectively.

#### **7.1 Effect of Boost Pressure**

The pressure drop across the air intake system is known to have a significant influence on the indicated power of the IC engine. The pressure drop is created due to the suction generated by the descending piston in the case of a naturally aspirated engine. The pressure drop along the intake system is very dependant on engine speed and

load, the flow resistance of different elements in the system, the cross sectional area through which the fresh charge moves, and the charge density (Heywood 1988). This section intends to investigate this phenomenon and the effect on the combustion quality as well as emissions on the Jaguar V6 diesel engine using common-rail injection and variable geometry turbine (VGT) technology. The pressure drop in intake manifold was varying by the use of butterfly valve which is installed between the intercooler and plenum chamber as shown in Figure 3.21. The pressure drop is defined as the different between local static pressure in intake manifold and initial boost pressure divided by initial boost pressure. The engine was fuelled with biodiesel (RME) and ULSD. Table 7 shows the details of the test conditions.

Table 7.1. Test conditions at engine speed of 1550rpm

<b>Mode</b>	<b>Legend</b>	<b>BMEP (bar)</b>	<b>Pressure drop (%)</b>
7.1	LP1	3.1	0
7.2	LP2	3.1	0.5
7.3	LP3	3.1	1.5
7.4	LP4	3.1	3.5
7.5	PP1	4.7	0
7.5	PP2	4.7	0.5
7.6	PP3	4.7	1.5
7.7	PP4	4.7	3.5

The engine is clearly responsive to the characteristics of the intake manifold such as pressure drop. Some of the parameters are closely related to the pressure drop

in the intake manifold while the others such as injection strategy is controlled by the EMS.

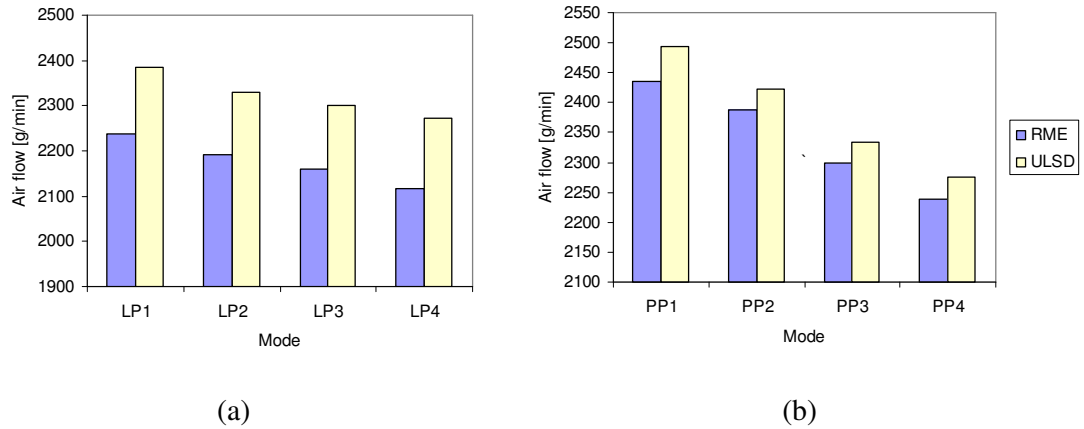


Figure 7.1 Air flow rate at engine speed of 1550rpm (a) low load, BMEP 3.1bar , (b) part load, BMEP 4.7bar

Figure 7.1 shows the air flow rate of the intake manifold as a consequence of pressure drop when RME and ULSD are used as fuel respectively. It can be seen that the air flow is decreased as pressure drop increases. This is predicted as a direct effect from the flow restriction in the AIS. Figure 7.1 also shows that the engine operating with RME inducted less air as compared with ULSD at both low load (BMEP 3.1bar) and part load (BMEP 4.7). Note that the engine was running at equal brake torque for both ULSD and RME. The stoichiometric air-fuel ratio (AFR) for RME is 15.6% lower than ULSD. Therefore, the engine operating with RME inducted less air as compared to ULSD to gain equal brake torque.

Figure 7.2 shows that the fuel flow rate is higher at part load as compared to low load. It is found that the fuel flow is slightly increased as pressure drop increases. At part load, the increase of fuel flow is clearly a response to pressure drop, where the

fuel flow rate is rapidly increased as pressure drop increases. At low load, the injection of RME is more than ULSD by 11.5% (mass). Figure 7.2 also revealed that at part load, the injection of RME is more than ULSD by 12.5%. This is the consequence of low calorific value of RME which is slightly lower so more fuel is required to gain similar brake torque as for ULSD.

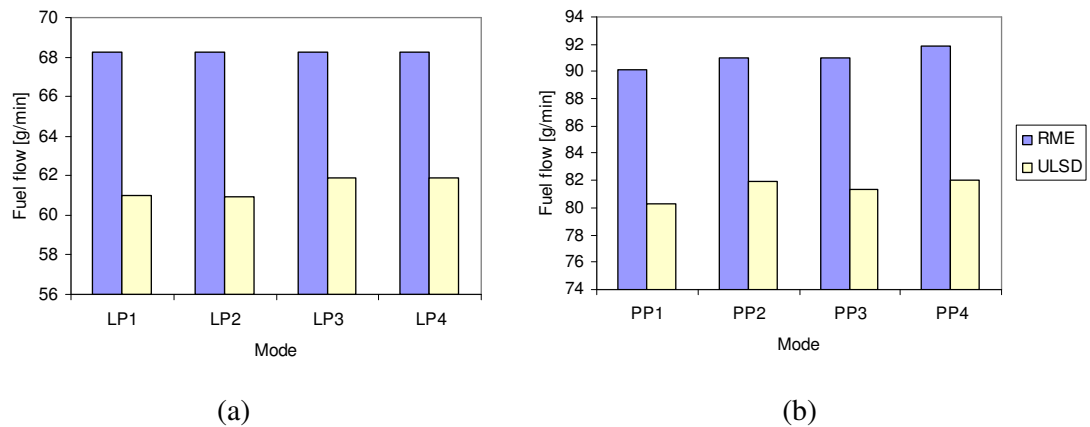


Figure 7.2 Fuel flow rate at engine speed of 1550rpm, (a) low load, BMEP 3.1bar (b) part load, BMEP 4.7bar

### 7.1.1 Engine Performance

Figure 7.3 presents the in-cylinder pressure for the combustion of ULSD and RME with the increase of the pressure drop. The dotted lines represent the in-cylinder pressure for RME while the straight lines represent ULSD. The in-cylinder pressure data was retracted from cylinder number 5 of the engine operating at 4.7 Bar BMEP and 1550 rpm. It is found that the in-cylinder pressure for the case of RME is higher at all pressure drops. The pressure difference is clearly seen on RME and ULSD at main fuel injections.

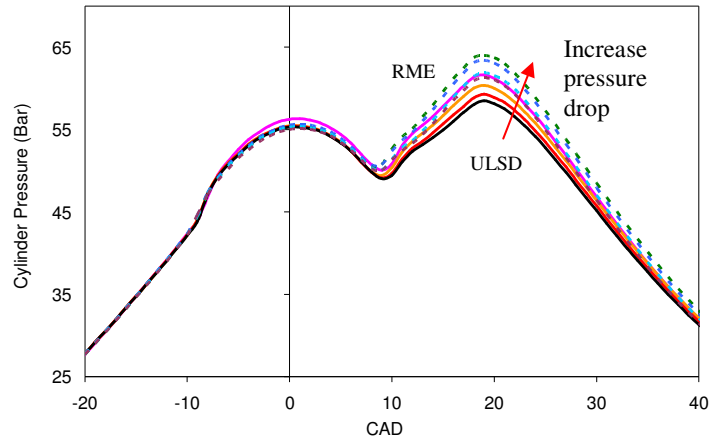


Figure 7.3 Cylinder pressure for ULSD and RME at different pressure drops at engine speed of 1550rpm (BMEP 4.7bar)

It is very interesting to see that even when the pressure drop declines, the peak pressure decreases. Research conducted by Spaddacini and quoted by reference (Heywood 1988) on auto-ignition characteristics under controlled conditions, revealed that when the boost pressure increases (or pressure drop decreases), the ignition delay decreases, resulting in the higher peak pressure in the engine cylinder. The reduced of ignition delays is associated with the reduction in premixing time when the boost pressure increases.

Figure 7.4 shows the ignition delay as a function of pressure drop and fuel type. The ignition delay is clearly higher at part load as compared with low load. Figure 7.4 also shows that at low load, the ignition delay is slightly increased as pressure drop increases. While, at part load, ignition delay is quickly increased as pressure drop increases from case LP1 to case LP4. The intake air pressure and temperature are two of the parameters associated with the air which have been proved to affect the ignition delay. The change of pressure and temperature in air intake

systems will vary the charge conditions during the delay period, thus resulting in a decrease in the ignition delay as intake pressure increases (Heywood 1988). Figure 7.4 shows that the ignition delay for RME is shorter as compared with ULSD. The most important reason is that the RME has a higher cetane number by 1.5% as compared with ULSD. As reported by Szybist et al, the ignition delay decrease as the cetane number in biodiesel fuel increase (Szybist et al. 2007). This is in agreement with many others who study the effect of cetane number of diesel fuel on ignition delay (Kidoguchi et al. 2000; Kitano et al. 2003; Nishiumi et al. 2004). Senatore et al has suggested that the biodiesel fuel has a slightly higher cetane number due to the long linear chain of the fatty acid part of the ester (Senatore et al. 2000).

The shorter of ignition delay when the biodiesel is used in a diesel engine was also compensated with the reason that the injections start earlier as compared with ULSD. The results also agree with the other study when the diesel engine especially with the pump-line-nozzle injection operating with RME (Desantes et al. 1999; Szybist et al. 2007; Tsolakis et al. 2007). The advanced of injection timing for biodiesel is perhaps due to rapid transferred of the pressure wave travels from the fuel injection pump to the fuel injection nozzle (pump-line-nozzle) resulted to early open of the fuel injector. The pressure wave travel speed is higher for RME is consequence of a higher bulk modulus of compressibility, and consequently a higher speed of sound, in the biodiesel relative to diesel fuel as explained in detail by Tat et al (Tat et al. 2006). In his research report, he concluded that the speed of sound and bulk modulus of the monoesters of soybean oil is higher than those for diesel fuel. This resulted to change the injection timing of diesel engines (Tat et al. 2006). However,

the earlier of injection timing also reported in a common-rail diesel engine as discussed in detail by Tat (Tat 2003). This is due to the accelerator overpressing which is required to compensate the lower of the biodiesel's low heating value (Tat 2003). Moreover, previous research on a similar engine on biodiesel blend with ULSD also recorded that the injection timing is advanced when the proportion of biodiesel is increased (Chuepeng et al. 2007).

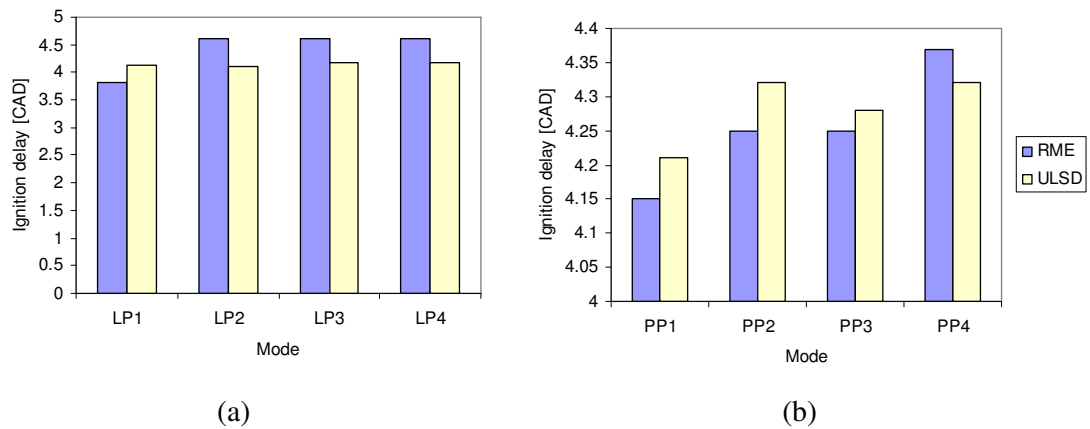


Figure 7.4 Ignition delay as consequences of pressure drop and engine load at engine speed of 1550rpm; (a) low load, BMEP 3.1bar (b) part load, BMEP 4.7bar

Figure 7.5 shows the bsfc of the engine operating with RME and ULSD at low load and part load. It can be seen that the bsfc is higher at low load as compared to high load and bsfc for RME is higher as compared to ULSD. The higher bsfc value in the case of RME is due to lower energy content as compared to ULSD and the engine has to inject more fuel to gain a equal brake torque as mention earlier. Figure 7.5 also revealed that the bsfc is slightly increased as pressure drop increases for both fuels and both engine load conditions. The bsfc is clearly a function of AFR as discussed in detail by Heywood (Heywood 1988). The discharge air decreases when the pressure

drop increases in the intake manifold, as depicted in Figure 7.1. This led to lower the AFR and slightly increased the bsfc of the engine.

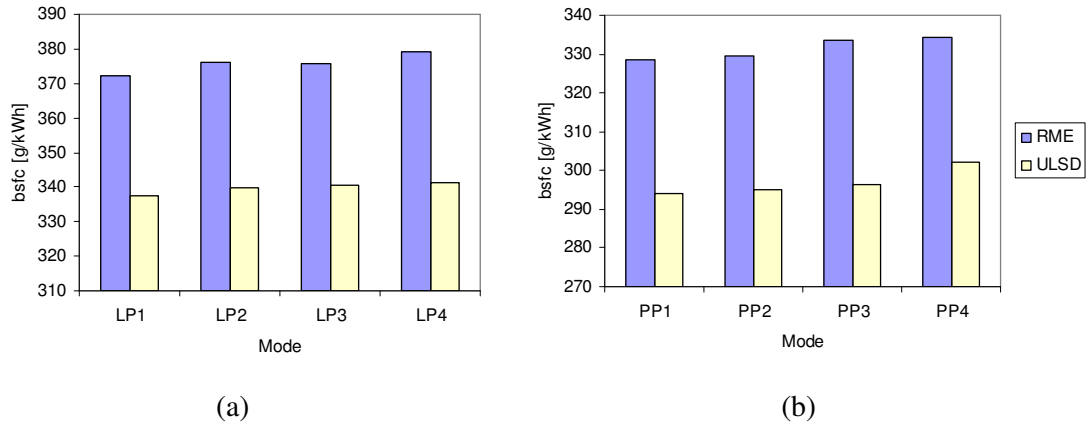


Figure 7.5 Brake specific fuel consumption at engine speed of 1550rpm; (a) low load, BMEP 3.1bar (b) part load, BMEP 4.7bar

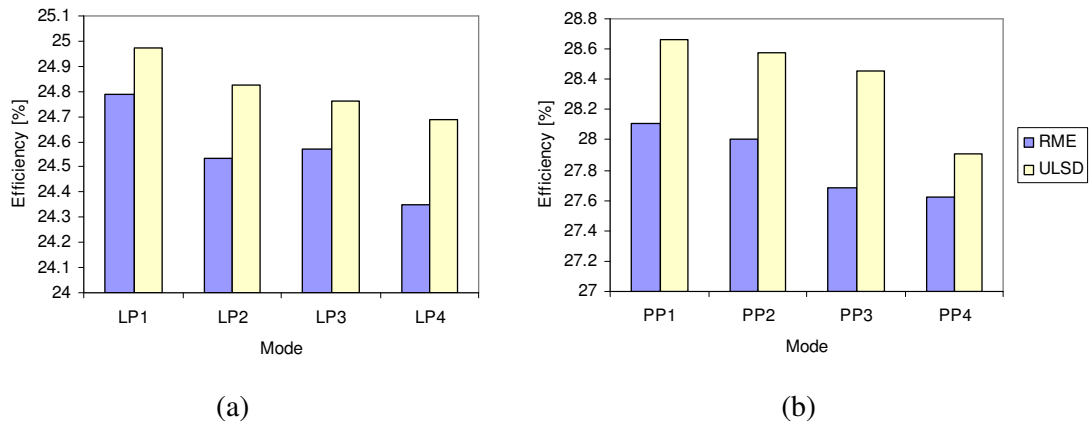


Figure 7.6 Efficiency of the engine at engine speed of 1550rpm; (a) low load, BMEP 3.1bar (b) part load, BMEP 4.7bar

Figure 7.6 shows the efficiency of the engine as a consequence of fuel and pressure drops. It shows that the engine efficiency is lower for RME as compared with ULSD and it is higher at part load as compared with low load. Figure 7.6 also

reveals that the efficiency is slightly decreased as pressure drop increases for both fuels.

### **7.1.2 Exhaust Emissions**

The NO<sub>x</sub> formed by the combustion of fuel in an internal combustion engine typically consists of nitric oxide (NO) and nitrogen dioxide (NO<sub>2</sub>) where the nitric oxide is dominant with a small amount of NO<sub>2</sub> (Heywood 1988). The formation of NO<sub>x</sub> is mostly from nitrogen in the air but some liquid fuels contain nitrogen such as NH<sub>3</sub>, NC and HCN and thus contribute to higher potential on producing more NO<sub>x</sub> (Ganesan 2003). It is known that this emission was highly dependent on post-combustion gas temperature, duration of gas exposure to this high temperature combustion and the species in post-combustion gases which is highly related to equivalent ratio,  $\phi$  (Keating 2007).

Figure 7.7 shows the NO<sub>x</sub> emission as a consequence of fuel and pressure drop. It can be seen that RME produces higher NO<sub>x</sub> as compared with ULSD at all load and pressure drop conditions. The result generally agreed with the reports by other studies on RME (Nwafor 2004; Labeckas et al. 2006). It has been understood that the premixed combustion is promoted when RME is injected by the common rail fuel injection system. This leads to the advanced of injection timing thus, increased peak in-cylinder pressure and temperature (Chuepeng et al. 2007). The combustion of RME promotes very low unburned hydrocarbon as compared with ULSD due to the high burning rate estimated by heat release as reported by many researchers on biodiesels (Agarwal 2007).

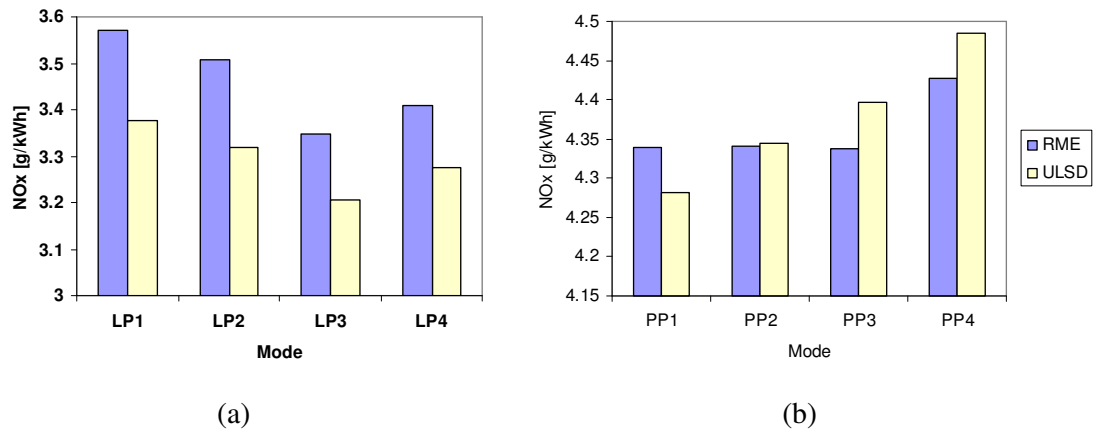


Figure 7.7 Exhaust emissions of NOx at engine speed of 1550rpm (a) low load, BMEP 3.1bar (b) part load, BMEP 4.7bar

The trend of NOx formation in Figure 7.7 is almost comparable to in-cylinder maximum pressure (Pmax) and this confirms that NOx formation is strongly depending on maximum pressure and temperature as indicated by the Zeldovich mechanism. At low load, the formation of NOx is slightly decreased as the pressure drop increases while at part load however NOx is slightly increased as the pressure drop increases. The formation of NOx is clearly related to the combustion behavior in the combustion chamber. Figure 7.4 shows that the ignition delay varies when the pressure drop increases. At low load, the ignition delay slightly increased promoted to increase the premixed combustion thus reduces the exhaust NOx. The combustion of fuel occurred at low pressure in the combustion chamber as compared with the part load case. This condition has led to lower peak flame temperatures as well as post combustion mixing with cooler excess air (Colban et al. 2007). At part load, the function of AFR is significant to the formations of NOx rather than ignition delay. The formation of exhaust emissions is strongly dependent on fuel distribution and the rate of change for fuel distributions due to the mixing process (Heywood 1988). The

NO<sub>x</sub> is increased when the AFR decreases as discussed by many investigators (Heywood 1988; Colban et al. 2007). Many researchers agree that the increase of boost pressure promoted to the lean combustions of the diesel engine and the rate of heat release is resemble to the injection rate, which becomes sharper and the quality of combustion improves (Aoyagi et al. 2006; Colban et al. 2007). Therefore, the increase of pressure drop as the boost pressure decreases is proved to give opposite affects on engine emissions.

Figure 7.8 shows the emissions of carbon monoxide from the combustion of RME and ULSD at low load and part load. It can be seen that the combustion of RME in a diesel engine produces more CO as compared with ULSD. Figure 7.8 also revealed that at low load, the formation of CO is higher as compared to part load.

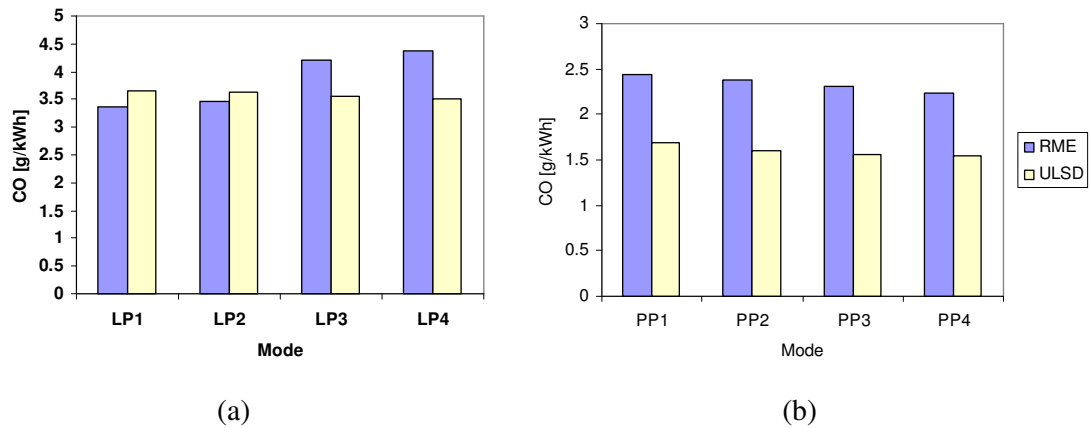


Figure 7.8 Emissions of carbon monoxide at engine speed of 1550rpm (a) low load, BMEP 3.1bar (b) part load, BMEP 4.7bar

Figure 7.9 shows the emissions of total hydrocarbon. It is clear that the combustions of ULSD produces higher THC as compared with RME at all pressure drops and engine load conditions. At low load, the formation of THC is not much

affected by the pressure drop. It is found that at high load, the formation of THC for RME is leveled as the pressure drop increases. Meanwhile at part load, the HC is reduced as the pressure drop increases.

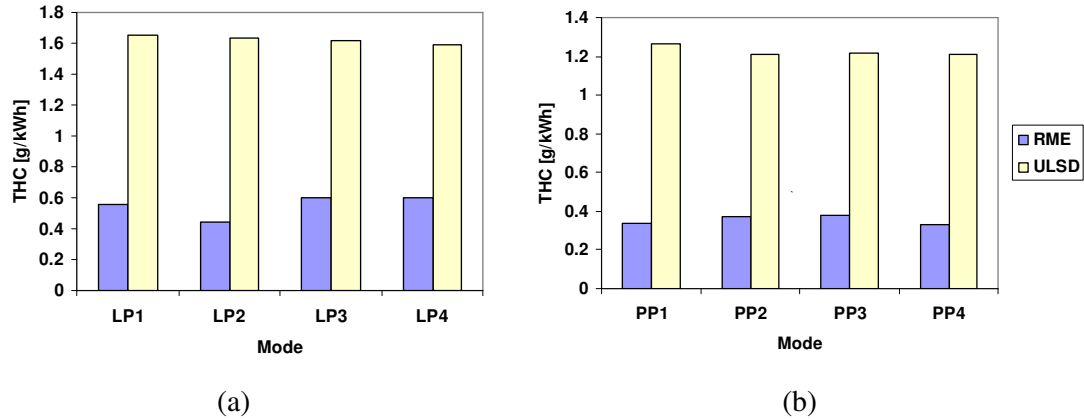


Figure 7.9 Emissions of total hydrocarbon at engine speed of 1550rpm; (a) low load, BMEP 3.1bar (b) part load, BMEP 4.7bar

## 7.2 Effect of Charge Air Temperature

It is apparent that the engine's power decreases as the air intake mass flow rate diminishes. In a diesel engines, a supercharger or turbocharger is widely used to increase the air flow rate, and hence the volumetric efficiency of the engine. Much research has been conducted on the effect of charge temperature to a diesel engine (Torregrosa et al. 2006; Beatrice et al. 2007; Maiboom et al. 2007). Moreover, the effect of charge air intake is extremely important to the recent development of HCCI engines world wide (Iida et al. 2001; Sjöberg et al. 2003; Iverson et al. 2005; Dubreuil et al. 2006; Shibata et al. 2006; Andreae et al. 2007). The properties of air which affect the mass flow rate, among others are the density which is linked to the air

temperature. The volumetric efficiency is increased as the charge air temperature reduces. However, the increase of charge air temperature could also possibly improve the fuel vaporisation in engine cylinders. This is extremely important for the diesel engine operating with biodiesel. Much research has been conducted to explain the effect of fuel vaporisation for biodiesel. Biodiesel is consists of the mono alkyl esters of vegetable oils and animal fats. The difference in chemical structure of biodiesel demonstrates distinctive impact on the chemical reaction pathways during ignition and combustion (Szybist et al. 2007).

The increase of inlet temperature promoted in the reduction of in-cylinder trap mass (thermal throttling effect). Therefore, the capacity of oxygen and heat capacity of the air charge significantly reduced when air temperature increases. The effect of charge air inlet temperature on diesel engines Maiboom et al. He has conducted a series of experiments on an inline-4 diesel engine. The engine was equipped with a cooled EGR system, common-rail injection system and VGT. The engine was operated with mineral diesel fuel at constant engine speed, EGR ratio and inlet boost pressure. The charge inlet temperature was varied from 20°C to 38°C. He concluded that the increase of inlet temperature at constant boost pressure results in a slight decrease of the ROHR. He suggests that at constant boost pressure, the fuel jet entrains less air with reduced in-cylinder gas density, resulting in a lower oxygen-fuel mixing therefore lower ROHR. Torregrosa et al. constructed a fully controlled diesel engine to study the influence of inlet air charge temperature on the performance and emissions of a diesel engine (Torregrosa et al. 2006). The intake temperature was varied but the coolant temperature was controlled to isolate the cylinder wall's

temperature. The report concluded that the increase of intake temperature leads to increased NOx emissions.

RME has a higher tendency to form fuel rich zones at low load conditions than the other fuels, due to higher viscosity and fuel distillation curves (Horn et al. 2007). In addition, RME has a possibility of poor fuel atomization and vaporization, due to its higher density, kinematic viscosity and distillation temperature than diesel fuel (Kawano et al. 2006). Research conducted by Stovell on a spark ignited natural gas engine also suggested that the small change in air intake temperature changed the engine response and performance as well as exhaust gas emissions (Stovell et al. 2001). He tested the engine with three different intake air temperatures (50°F, 80°F and 130°F) to evaluate their impact upon engine performance and emissions.

In the present study, it is decided to investigate this phenomenon and its effect on the progress of combustion quality as well as on emissions on the V6 diesel engine. The experiment was focused on the details of engine performance and emissions at two different brake torque at 1550rpm of engine speed. The air intake temperature was measured by thermocouple attached to the intake manifold just after the intercooler and the data was compared with the reading from the ECU. The temperature was automatically controlled by the controller to secure the accuracy of the temperature reading. Comparisons between ULSD and RME have been made at one fuel temperature of 35°C.

Table 7.2. Boost temperature in air intake systems

<b>Mode</b>	<b>BMEP (bar)</b>	<b>Boost temperature (°C)</b>
7.8	3.1	35
7.9	3.1	40
7.10	3.1	45
7.11	4.7	35
7.12	4.7	40
7.13	4.7	45

Table 7.2 shows the details of the test conditions. The experiments have been conducted on the Lion V6 engine operated with ULSD and RME. The EGR operation was switch off to isolate the effect of dilution and temperature of exhaust gas to the air intake. The engine was operated at low load (BMEP 3.1 bar) and part load (BMEP 4.7 bar).

Figures 7.10 (a) and (b) show fuel flow rate of a V6 diesel engine operating with RME and ULSD at low load and part load respectively. At low load, the fuel flow rate is increased as the boost air temperature increases. At part load, the fuel flow rate is decreased as the boost air temperature increases. Figure 7.10 clearly shows that the fuel flow rate is slightly higher for RME as compared with ULSD for all of the test conditions. The low heating value for RME is 8.7% lower as compared to ULSD, therefore the ECU commanded the fuel injector to inject more fuel to gain similar brake torque to ULSD.

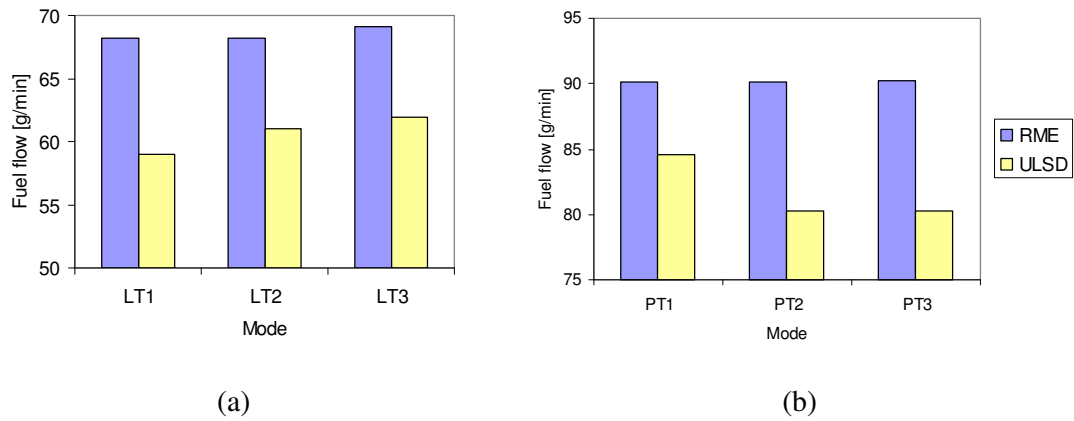


Figure 7.10 Fuel flow rate at engine speed of 1550rpm (a) low load, BMEP 3.1bar (b) part load, BMEP 4.7bar

Figure 7.11 shows that the engine operating with ULSD consumed higher air flow rate at all engine loads and boost air temperature. Both fuels show a similar trend where the air fuel ratio is reduced as boost temperature decreases. However, the air flow rate is reduced significantly as boost temperature increases for the case of ULSD.

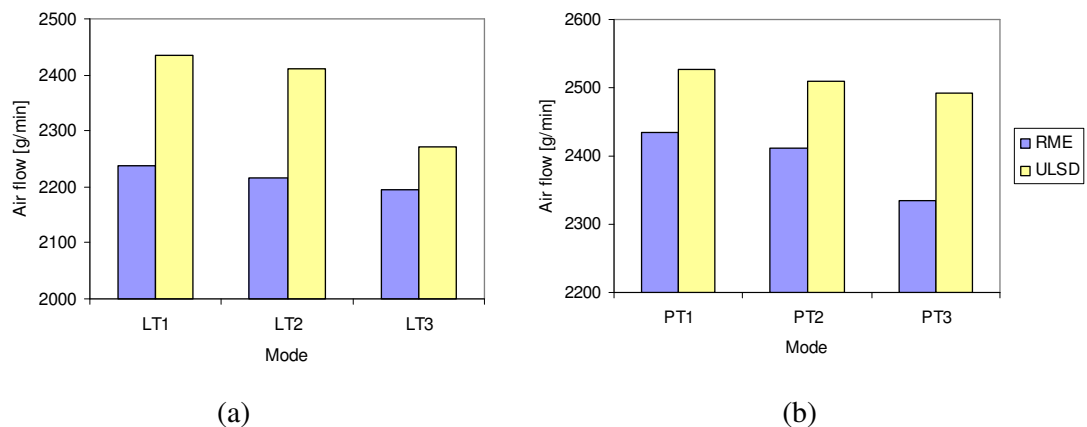


Figure 7.11 Air flow rate at engine speed of 1550rpm (a) low load, BMEP 3.1bar (b) part load, BMEP 4.7bar

Figure 7.12 shows the engine excess air ratio (lambda) as a consequence of changes in the engine load and boost air temperature. It shows that the diesel engine operated with low lambda values when RME is used to fuel the engine. Figure 7.12 also shows that the lambda for RME is almost constant at 2.6 and 2.2 for low load and part load respectively. The lambda is reduced for ULSD at low load, when boost air temperature increased. However when the engine is operating at part load, the lambda is slightly increased as boost air temperature increases from 35°C to 45°C.

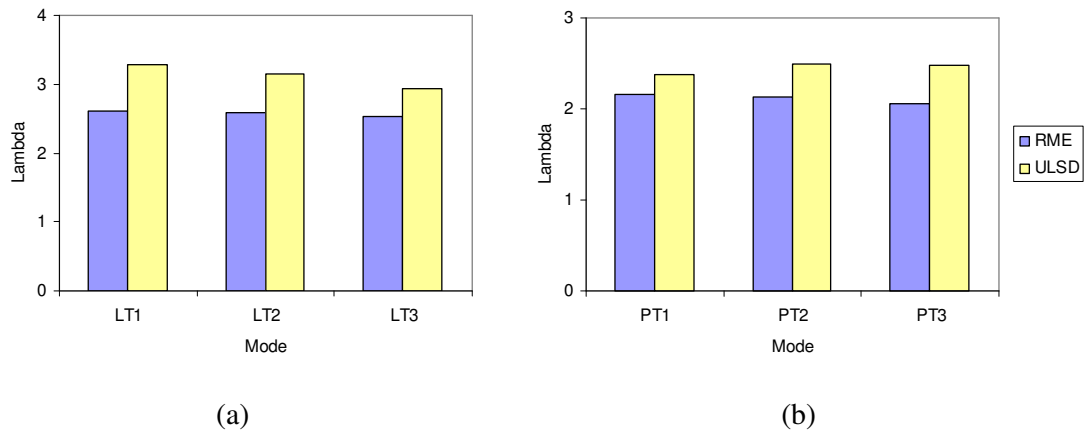


Figure 7.12 Engine excess air ratio at engine speed of 1550rpm (a) low load, BMEP 3.1bar, (b) part load, BMEP 4.7bar

Figure 7.13 shows the common rail fuel injection pressure as a consequence of engine load and boost air temperature. It clearly shows that the fuel injection pressure for RME is higher at all test conditions. At low load, the injection pressure is slightly increased as boost air temperature increases. At part load, the injection pressure slightly decreases as boost air temperature increases. Figure 7.13 also shows that the fuel injection pressure drops significantly for ULSD as compared with RME when the boost air temperature increases.

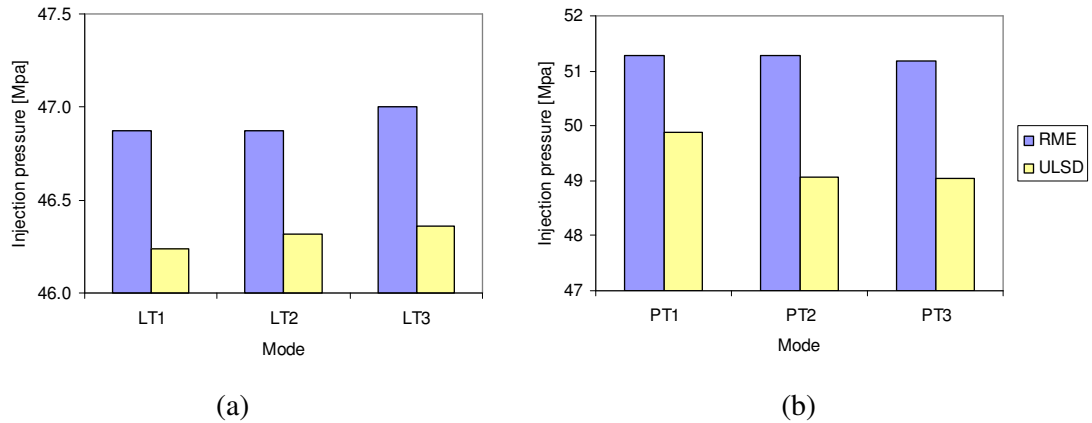
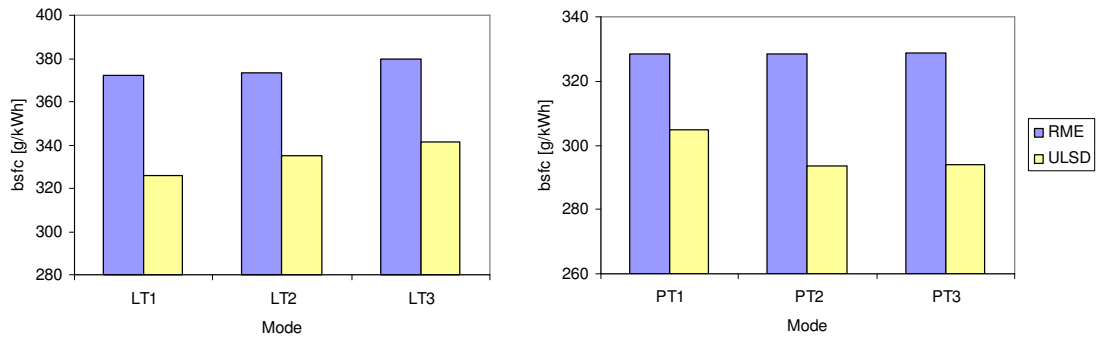


Figure 7.13 Fuel injection pressure at engine speed of 1550rpm (a) low load, BMEP 3.1bar (b) part load, BMEP 4.7bar

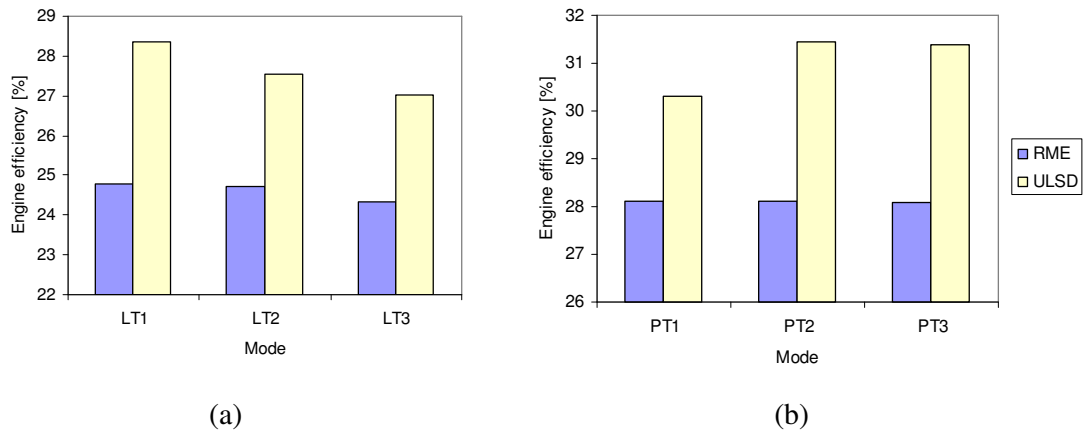
### 7.2.1 Engine Performance

Figure 7.14 shows the bsfc for the engine operating with RME and ULSD as a consequence of change in the boost air temperature. It shows that the bsfc is higher for RME at all test conditions. At low load, bsfc is increased as boost air temperature increases. At part load, the bsfc is decreased as boost air temperature increases. Figure 7.14 also shows that the bsfc is higher at low load as compared with part load for both fuels. The bsfc for ULSD changes significantly when boost air temperature increases as compared with RME.



(a) (b)

Figure 7.14 Brake specific fuel consumption at engine speed of 1550rpm (a) low load, BMEP 3.1bar (b) part load, BMEP 4.7bar



(a) (b)

Figure 7.15 Engine efficiency at engine speed of 1550rpm (a) low load, BMEP 3.1bar (b) part load, BMEP 4.7bar

Figure 7.15 present the engine efficiency as a consequence of engine load and boost air temperature. Figure 7.15 clearly shows that ULSD operated at higher engine efficiency as compared with RME. This is due to the low energy content of RME as compared with mineral diesel. At low load, the engine efficiency is reduced as boost air temperature increased from 35°C to 45°C. At part load, the engine efficiency is

increased as boost air temperature increases. The engine efficiency changed significantly with the boost air temperature for ULSD as compared to RME both at low load, and part load.

### 7.2.3 Exhaust Gas Emissions

Figure 7.16 presents the exhaust gas emissions from the combustion of RME and ULSD at low load and part load. It clearly shows that the RME produces higher emissions of NO<sub>x</sub> as compared with ULSD. This is in agreement with many reports in literature where the engines were operating with biodiesel (Senatore et al. 2000; Lapuerta et al. 2002; Labeckas et al. 2006; Horn et al. 2007; Szybist et al. 2007). The engine produces higher NO<sub>x</sub> at part load as compared with low load for both fuels. The emission of NO<sub>x</sub> is slightly increased as boost air temperature increases for ULSD but is approximately levelled for RME.

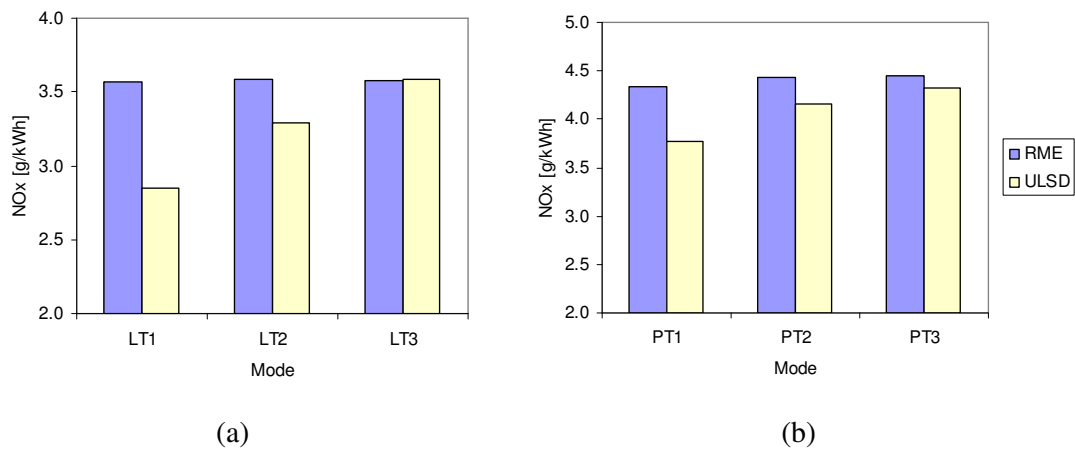


Figure 7.16 Exhaust emission of NO<sub>x</sub> at engine speed of 1550rpm (a) low load, BMEP 3.1bar (b) part load, BMEP 4.7bar

Figure 7.17 shows the exhaust gas emissions of CO at low load and part load when the boost air temperature increases. At low load, the CO is increased as boost air temperature increases, whereas at part load, the CO is decreased as the boost air temperature increases. Generally, the RME produces less CO as compared to ULSD at 35°C but it produces significantly higher CO when the boost air temperature is increased to the level higher than 35°C.

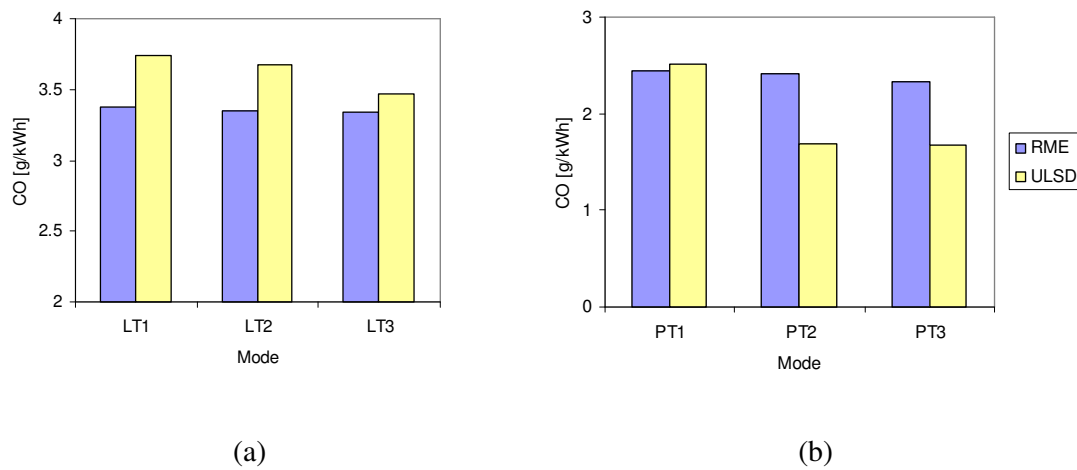


Figure 7.17 Exhaust emission of CO at engine speed of 1550rpm (a) low load, BMEP 3.1bar (b) part load, BMEP 4.7bar

Figure 7.18 presents the emissions of THC at low load and part load when the engine is operating with RME and ULSD. It shows that the engine operating with RME produces less THC as compared with ULSD at both engine loads. The THC is slightly increased when the boost air temperature increases for both fuels.

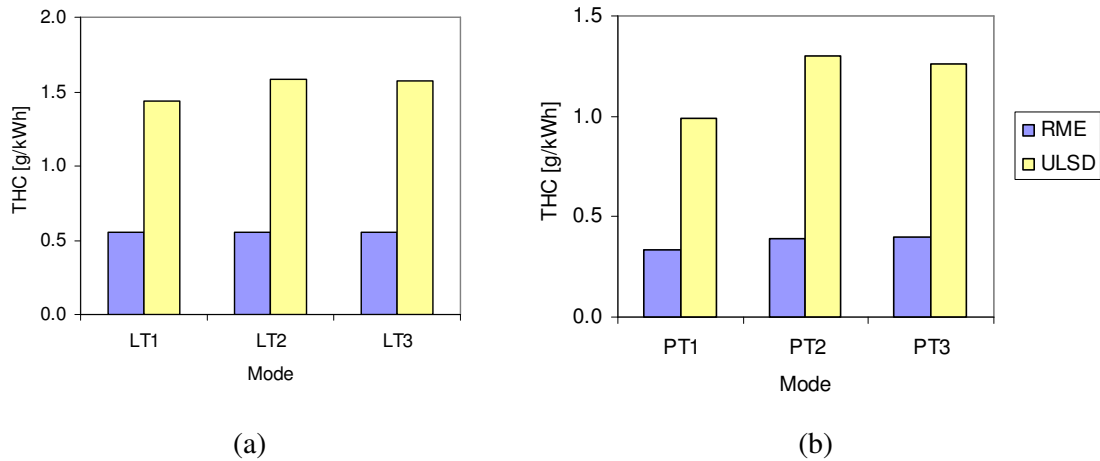


Figure 7.18 Exhaust emission of THC at engine speed of (a) low load, BMEP 3.1bar  
(b) part load, BMEP 4.7bar

### 7.3 Summary

In this chapter, the effect of boost temperature and pressure of the intake air is discussed in detail. It can be concluded that the increase of pressure drop caused by the throttling in the intake manifold led to higher in-cylinder pressure. This is mainly due to the increase of the ignition delay. The effect of boost pressure is more obvious at higher engine load than at low engine load. The increase of pressure drop has also led to a small increase in the bsfc and reduced the engine efficiency for the engine operating with both ULSD and RME. The experimental results have also showed that the emissions of NO<sub>x</sub> are decreased at low load but slightly increased at part load. This is due to the effect of ignition delay and AFR for low load and part load respectively.

The increase of inlet temperature led to the reductions of in-cylinder trap mass and therefore reduced the oxygen and heat capacity of the charged air. This has resulted in an increase of bsfc at low load but slightly lowered the bsfc at part load when the charge air temperature is increased. The exhaust gas emissions are slightly increased for ULSD but remain levelled for RME. The emission of CO is decreased and the emission of THC is increased when the charge air temperature increases.

## **CHAPTER 8**

### **CONCLUSIONS AND RECOMMENDATION**

The research work reported in this thesis consists of two major parts. The first part is the performance of the air induction system of a V6 diesel engine was investigated through 3D simulation and the engine dynamic flow was simulated by 1D simulation whereas the models were validated by experimental data. The 3D simulation was conducted using Fluent version 6.2 while the Ricardo WAVE commercial gas dynamic engine cycle was used for 1D analysis. The experimental data from the V6 diesel engine have been used to validate the simulation results. The diesel engine was operated with ULSD and RME in order to study the performance and emissions of the engine fuelled by biodiesel with the effect of air intake charge conditions. Generally the results have revealed that the effect of a number of important parameters in the diesel engine operations and these include EGR, injection strategy, air intake pressure and temperature. The conclusions are summarised in section 8.1 and some suggestions for future work are given in the end.

## **8.1. Conclusion Remarks**

### **8.1.1 Influence of Negative Pressure on the Induction Grill**

In order to quantify the effect of negative pressure on the induction grill, 3D analysis of real geometry of a Freelander AIS has been investigated with respect to the fluid flow behaviour on the intake system. The results show that the magnitude of fluid flow velocity on the intake grill has a significant impact on the pressure drop in the intake manifold. The flow behaviour in the intake manifold changes significantly as the velocity magnitude is increased. Moreover, the mass flow rate is influenced by the tangential velocity at the grill entry. The results from the steady flow test give a good agreement with simulation results. In general, for a given constant pressure drop, the higher the tangential speed, the lower the mass flow into the engine, which subsequently reduces the volumetric efficiency. Therefore, the grill design of the air induction system is very important to enhance the volumetric efficiency of air induction systems. This is extremely important especially when the induction grill is located at the rear side of vehicle.

### **8.1.2 One-Dimensional Analysis of the Air Induction System of a V6 Diesel Engine.**

The induction system of a V6 diesel engine has been simulated to study the effect its consignment on the performance of a diesel engine. The main objective is to use the wave action strategy to optimise the air induction system of a V6 diesel engine. The study starts with the engine models operating at full load for 7 different

engine speeds from 1000rpm to 4000rpm. The simulation results were compared with the experimental data provided by Jaguar Land Rover, and a good agreement is obtained with a relative error between 1% and 9%. The analysis of the pressure wave on the intake manifold suggests that the pressure drop in the intake manifold gives a considerable effect on the performance of the air induction system.

### **8.1.3 Performance and Emissions of a Diesel Engine Operating with ULSD and RME.**

The experimental work was conducted on a V6 diesel engine operating with ULSD and RME. The engine was tested at low load and part load. The result has showed that the engine was operating with RME produces higher NO<sub>x</sub> as compared with the engine operating with ULSD, but produces significantly lower CO and THC. The effect of EGR on the emissions, especially the reductions of NO<sub>x</sub> is evident for ULSD and RME. However, with standard engine calibration, the EGR level is different between ULSD and RME when the engine is operated at equal brake torque and engine speed. Therefore, in order to have a better engine performance and lower emissions, the engine needs new calibration when biodiesel is used as a fuel. It also found the engine operated with RME produced a 5% higher in-cylinder pressure and therefore higher charge air pressure at an engine speed of 1550rpm with 102Nm brake torque. The experiment result has also concluded that the small change in fuel temperature (10°C) gives an impact to the engine performance and exhaust emissions. It is believe that the small change of pressure drop and temperature in the intake manifold would change the ‘environment’ temperature for the fuel spray and thus

affect the fuel spray droplet size and distribution promoted to amend the engine performance and emissions. The small increase of fuel temperature from 30°C to 40°C has reduced the viscosity and density of the fuel. This led to an increase in the mixing rate of fuel and air in the cylinder, and is useful for improving the fuel consumption and engine performance. When EGR was not introduced, such an effect was evident.

With standard engine calibration, the engine is operated with double injections where each of the injection timing varies according to engine speed and load. It was found that the engine performance and engine emission is highly dependant on injection strategy as was expected. The application of dual injection strategy without the EGR system shows a significant lower of hydrocarbon emissions but it has major drawbacks of producing higher NO<sub>x</sub>. The experimental results also reveal that pilot injection lowered peak pressure and brake specific fuel consumption regardless of EGR operations. The effect of EGR on reducing NO<sub>x</sub> emissions is more significant compared with the effect of multiple injection strategies. The combination of EGR and dual injection strategies produce even further reductions in emissions especially of NO<sub>x</sub> and particulate matter.

#### **8.1.4 The Effect of Intake Charge Pressure Drop and Temperature on Engine Performance**

The experimental results showed that the intake charge pressure and temperature have significant effect on the performance as well as emission levels of a diesel engine. The diesel engine operated at higher pressure drop increases the bsfc,

thus reduces the engine efficiency on both low load and part load. The emission of NO<sub>x</sub> was influenced by the combustion process in the engine cylinder and therefore has a different association with the intake charge pressure. At low load test conditions, the emissions of NO<sub>x</sub> decreased as pressure drop increased while at part load, the exhaust NO<sub>x</sub> increased as the pressure drop increases for both ULSD and RME. It is found that the rates of the decrease and increase of NO<sub>x</sub> emissions are different between ULSD and RME. It is clear that at low load, the emissions of NO<sub>x</sub> decreased significantly for ULSD when the pressure drop increased as compared with RME. At part load, the emissions of NO<sub>x</sub> increased significantly for ULSD when the pressure drop increased as compared to RME.

The charge temperature has a significant effect the performance and emissions of a diesel engine. However the trends dependent on engine load and fuel type. At low load, as the charge air temperature increased, the bsfc increases and engine efficiency decreases for both ULSD and RME. The emissions of NO<sub>x</sub>, CO and THC are generally increased as charge air temperature increases for both ULSD and RME. While at part load, the bsfc and engine efficiency improve significantly as charge temperature increased from 35°C to 45°C. However, the emission of NO<sub>x</sub> is increased when the charge temperature increases, while CO and THC are decreased. The engine performance is altered when the ignition delay changed according to charge air temperature at a given engine load conditions. The formation of NO<sub>x</sub> generally is governed by the combustion process in the cylinder of the engine.

## **8.2. Future Work**

After a series of simulations and experimental work for the diesel engine, the author would like to address several issues concerning the future work as follows.

### **8.2.1 The modifications of Current Design of Freelander Air Intake System**

The 3D analysis of air intake system of a Freelander vehicle is simulated with standard air intake system. There is no modification made to improve the geometry and design of the intake manifold and grill. The simulation results show that the negative pressure in intake grill reduces the volumetric efficiency of the air intake system. Therefore, it is valuable to modify the geometry and design of the grill and manifold to optimise the performance of air intake system. One-dimensional simulation such as Ricardo WAVE also can be used together with 3D geometry to optimised the required length and overall geometry of air intake system.

### **8.2.2 The Effect of EGR Rate and Exhaust Gas Temperature on the Intake Charge.**

The experiment so far has been conducted with the standard operation of EGR. Therefore, the EGR rate is fully controlled by the ECU based on the current engine calibrations. Thus the results are compared between ULSD and RME at a standard operation basis. The engine was operated without any modification on the engine hardware and calibrations. For experimental purposes, it is very useful to compare the result between ULSD and RME for fixed EGR. This is will be heelpfull to improving

understanding the effect of EGR and their impact on the engine performance and emissions when the engine is operating with ULSD and RME respectively.

### **8.2.3 Transient Operation on Diesel Engine Operating with ULSD and RME.**

The V6 diesel engine with the instrumentation used for the present study is capable of running at a steady-state operation. The current dynamometer controller and the fuel pedal control are unable to operate at transient mode. The transient mode test is crucial to simulate the 'real' travel conditions on the road. The transient test can be performed according to European driving test conditions and it will provide paramount data of the engine performance and emissions rate at real time scale, thus provide the real performance and emissions of the engine operating with ULSD and neat RME.

## REFERENCES

- Abd-Alla, G. H. (2002). "Using Exhaust Gas Recirculation in Internal Combustion Engines: a Review." Energy Conversion and Management 43 (2002) 1027-1042.
- Agarwal, A. K. (2007). "Biofuels (Alcohol and Biodiesel) Applications as Fuels for Internal Combustion Engines." Progress in Energy and Combustion Science 33 (2007) 233-271.
- Agnew, D. D. and G. J. Rohrback (2004). "Engineering a Composite Intake Manifold for the Performance Aftermarket." SAE Technical Paper 2004-01-3512.
- Alcini, W. V. and I. West (2006). "GT Model for Passive Flapper Exhaust Valve." SAE Technical Paper 2006-01-1373.
- Altön, R., S. Cetinkaya and H. S. Yucesu (2001). "The potential of using vegetable oil fuels as fuel for diesel engines." Vol. 42: 529±538.
- Araneo, L., A. Coghe, G. Brunello and R. Dondé (2000). "Effects of Fuel Temperature and Ambient Pressure on a GDI Swirled Injector Spray." SAE Technical Paper 2000-01-1901.
- Athavale, S. M. and P. R. Sajanpawar (1999). "Analysis and Development of Inline Helmholtz Resonator through Computer Simulation for Elimination of Low Frequency Intake Noise Character." SAE Technical Paper 1999-01-1662.
- Bai, M., J. Lv and Z. Shao (2008). "A Study of Performance Development and Optimization of 6106 Diesel Engine." SAE Technical Paper 2008-01-1725.
- Balat, M. and H. Balat (2008). "A Critical Review of Bio-diesel as a Vehicular Fuel." Energy Conversion and Management Vol 49: 2727-2741.

- Balusamy, T. and R. Marappan (2007). "Performance evaluation of direct injection diesel engine with blends of Thevetia peruviana seed oil and diesel." Journal of Scientific & Industrial Research Vol. 66: 1035-1040.
- Baukal, C. E. (2001). The John Zink Combustion Handbook. London, CRC Press.
- Bayraktar, I. and T. Bayraktar (2006). "Guidelines for CFD Simulations of Ground Vehicle Aerodynamics." SAE Technical Paper 2006-01-3544.
- Bevan, K. E. and J. B. Ghandhi (2004). "PIV Measurements of In-Cylinder Flow in a Four-Stroke Utility Engine and Correlation with Steady Flow Results." SAE Technical Paper 2004-32-0005.
- Bialkowski, M. T., T. Pekdemir, D. P. Towers, R. Reuben, M. Brautsch and G. Elsbett (2004). "Effect of Fuel Temperature and Ambient Pressure on a Common Rail Rapeseed Oil Spray." Journal of KONES Internal Combustion Engines Vol. 11(1-2).
- Board, E. B. (2006). EBB Publishes Annual Biodiesel Production Statistics. 535/COM/07. Bruxelles, European Biodiesel Board.
- Bohac, S. V. and D. N. Assanis (2001). "Quantification of Local Ozone Production Attributable to Automobile Hydrocarbon Emissions." SAE Technical Paper 2001-01-3760.
- Bozbas, K. (2008). "Biodiesel as an Alternative Motor Fuel: Production and Policies in the European Union." Renewable and Sustainable Energy Reviews 12 (2008) 542-552.
- Bozza, F., A. Gimelli, V. Pianese, S. D. Martino and R. Curion (2004). "An Acoustic Design Procedure for Intake Systems: 1DAnalysis and Experimental Validation." SAE Technical Paper 2004-01-0412.

- BP (1998). BP Gas Oil Safety Data Sheet. Sheet No: SUK2102, BP Oil UK Ltd: 1.
- Caton, J. A. (2003). "Effects of Burn Rate Parameters on Nitric Oxide Emissions for a Spark Ignition Engine: Results from a Three-Zone, Thermodynamic Simulation." SAE Technical Paper 2003-01-0720.
- Chao, P.-K., Y. Goktas, W. Weber and K. Nelson (1999). "A Statistical Investigation of High Frequency Radiated Noise from a Composite Nylon Intake Manifold." 1999-01-1228.
- Chen, C., D. R. Amlee, R. J. R. Johns and Y. Zeng (2004). "Detailed Modeling of Liquid Fuel Sprays in One-Dimensional Gas Flow Simulation." SAE Technical Paper 2004-01-3000.
- Chuepeng, S. (2008). Quantitative Impact on Engine Performance and Emissions of High Proportion Biodiesel Blends and the Required Engine Control Strategies, University of Birmingham. PhD Thesis.
- Chuepeng, S. (2008). Quantitative Impact on Engine Performance and Emissions of High Proportion Biodiesel Blends and the Required Engine Control Strategies. PhD Thesis, The University of Birmingham.
- Chuepeng, S., A. Tsolakis, K. Theinnoi, H. M. Xu, M. L. Wyszynski and J. Qiao (2007). "A Study of Quantitative Impact on Emissions of High Proportion RME-Based Biodiesel Blends." SAE Technical Journal 2007-01-0072.
- Cipolat, D. (2007). "Analysis of energy release and NO<sub>x</sub> emissions of a CI engine fuelled on diesel and DME." Applied Thermal Engineering 27(11-12): 2095.
- Colin, G., P. Giansetti, Y. Chamaillard and P. Higelin (2007). "In-Cylinder Mass Estimation Using Cylinder Pressure." SAE Technical Paper 2007-24-0049.

- Cussons (2008). P7305/SP Impulse Swirl Meter with Port Flow Rig and Display.  
<http://www.cussons.co.uk/pdf/english/enauto/P7305SP.pdf>. Retrieval on  
18/11/08.
- Demirbas, A. (2007). "Importance of biodiesel as transportation fuel." Energy Policy  
35(9): 4661.
- Dennis, A. J., C. P. Garner and D. H. C. Taylor (1999). "The Effect of EGR on Diesel  
Engine Wear." SAE Technical Paper 1999-01-0839.
- Devi, R., P. Saxena, B. Walter, B. Record and V. Rajendran (2004). "Pressure  
Reduction in Intake System of a Turbocharged-Inter  
Cooled DI Diesel Engine Using CFD Methodology." SAE Technical Paper 2004-01-  
1874.
- Douglas, J. F. (1995). Fluid Mechanics. London, Longman Scientific & Technical.
- EBB (2008). European Biodiesel Board Position Paper on the Commission Proposal  
for a New Directive on Renewable Energies Revising Directive 2003/30 on the  
Promotion of Biofuels. 25/COM/08. Bruxelles, European Biodiesel Board.
- EEC (2000). "The approximation of the laws of the Member States relating to  
measures to be taken against the emission of gaseous and particulate pollutants  
from compression ignition engines for use in vehicles, and the emission of  
gaseous pollutants from positive ignition engines fuelled with natural gas or  
liquefied petroleum gas for use in vehicles and amending Council Directive  
88/77/EEC." Official Journal of the European Union Directive 1999/96/EC  
(2000)(L44: 1 - 155).
- Egnell, R. (2000). "The Influence of EGR on Heat Release Rate and NO Formation in  
a DI Diesel Engine." SAE Technical Paper 2000-01-1807.

- EPA (2002). A Comprehensive Analysis of Biodiesel Impacts on Exhaust Emissions. Draft Technical Report, EPA420-P-02-001, United States Environmental Protection Agency.
- Ferguson, C. F. (2001). Internal Combustion Engine. New Jersey, John Wiley & Sons.
- Fluent (2005). FLUENT 6.2 User's Guide. Lebanon, FLUENT Inc.
- Gaikwad, S., K. Arora, V. Korivi and S. K. Cho (2008). "Steady and Transient CFD Approach for Port Optimization." SAE Technical Paper 2008-01-1430.
- Ganesan, V. (2003). Internal Combustion Engines. New Delhi, McGraw Hill.
- Ganesan, V., J. S. Kumar and V. Balasubramanian (2004). "Flow field Analysis of a Multi Cylinder S.I Engine Air Intake System Using Computational Fluid Dynamics." SAE Technical Paper 2004-28-0010.
- Garrett (2004). Garrett Performance Product Catalogue. Los Angeles.
- Gilkes, O. S., R. Mishra, J. Fieldhouse and V. Rao (2008). "Simulation of the Transient Performance of a Turbocharged Diesel Engine Featuring a Two Point Air Injection Transient Assist System." SAE Technical Paper 2008-01-1192.
- Glassman, I. (1987). Combustion. Orlando, Academic Press Inc.
- Goswami, D. Y. and F. Kreith (2007). Energy Conversion. London, CRC Press.
- Hajireza, S., B. Sundén and F. Mauss (2000). "Effect of Inhomogeneities in the End Gas Temperature Field on the Autoignition in SI Engines." 2000-01-0954.
- Hasimoglu, C., M. Ciniviz, I. Ozsert, Y. Icingur, A. Parlak and M. S. Salman (2008). "Performance Characteristics of a Low Heat Rejection Diesel Engine Operating with Biodiesel." Renewable Energy Vol. 33: 1709-1715.

- Hester, R. E. and R. M. Harrison (2004). Transport and the Environment. Cambridge, The Royal Society of Chemistry.
- Heywood, J. B. (1988). Internal Combustion Engine Fundamentals. New York, McGraw Hill.
- Hirose, Y., H. Kino, T. Sawatari, K. Kaminaga and K. Yokohashi (2002). "Acoustic Analysis of Unreflective (Non-Resonant) Duct." SAE Technical Paper 2002-01-0857.
- Horn, U., R. Egnell, B. Johansson and Ö. Andersson (2007). "Detailed Heat Release Analyses with Regard to Combustion of RME and Oxygenated Fuels in an HSDI Diesel Engine." SAE Technical Paper 2007-01-0627.
- Husberg, T., S. Gjirja, I. Denbratt and J. Engstrom (2004). "Visualization of EGR on Diesel Combustion with Long Ignition Delay in a Heavy-duty Engine." SAE Technical Paper 2004-01-2947.
- Inagaki, K., M. Ueda, J. Mizuta, K. Nakakita and S. Nakayama (2008). "Universal Diesel Engine Simulator (UniDES): 1st Report: Phenomenological Multi-Zone PDF Model for Predicting the Transient Behavior of Diesel Engine Combustion." 2008-01-0843.
- Jajoo, B. N., A. N. Pawar and M. R. Nandgaonkar (2005). "Coating for Improving Diesel Engine Performance Using Turbocharger." 15th Asia-Pacific Conference on Combustion, Australia.
- Jia, M., M. Xie and Z. Peng (2008). "A Comparative Study of Multi-zone Combustion Models for HCCI Engines." SAE Technical Paper 2008-01-0064.
- Joshi, S. S., V. Mathews, M. Nandgaonkar, S. Kajale, M. Niranjana, S. Krishnan and S. K. Mahajan (2008). "Application of CFD Methodology to Reduce the Pressure

- Drop and Water Entry in the Air Intake System of Turbocharged Engine." SAE Technical Paper 2008-01-1172.
- Kandasamy, K., S. Jeganathan and R. Ganesan (2008). "Operation and Combustion Characteristics of a Direct Injection Diesel Engine Filled with Esterified Cotton Seed Oil." Modern Applied Science Vol 2: 71-80.
- Kawano, D., H. Ishii, Y. Goto, A. Noda and Y. Aoyagi (2006). "Application of Biodiesel Fuel to Modern Diesel Engine." SAE Technical Paper 2006-01-0233.
- Kawano, D., H. Ishii, Y. Goto, A. Noda and Y. Aoyagi (2007). "Effect of Exhaust Gas Recirculation on Exhaust Emissions from Diesel Engines Fuelled with Biodiesel." SAE Technical Paper 2007-24-0128.
- Kawashima, J.-i., H. Ogawa and Y. Tsuru (1998). "Research on a variable swirl intake port for 4-valve, high-speed DI diesel engines." SAE Technical Paper 982680.
- Keating, E. L. (2007). Applied Combustion. London, CRC Press.
- Kimberley, W. (2004). Diesel-Engine Management, Robert Bosch GmbH.
- Kitahara, S., H. Takao, T. Hashimoto and S. Hatano (2005). "Improvement of Car Interior Noise by Utilizing a Porous Intake Duct: Treatment Effect on an Intake System." SAE Technical Paper 2005-01-2363.
- Kobayashi, T. and K. Arase (1999). "Intake System Optimization by Intake Loss Coefficient Method." SAE Technical Paper 1999-01-3337.
- Kreith, F. and D. Y. Goswami (2007). Handbook of Energy Efficiency and Renewable Energy. London, CRC Press.

- Kubicki, M., H. C. Watson, J. Williams and P. C. Stryker (2007). "Spatial and Temporal Temperature Distributions in a Spark Ignition Engine Piston at WOT." SAE Technical Paper 2007-01-1436.
- Kubota, M., K. Yoshida, H. Shoji and H. Tanaka (2002). "A Study of the Influence of Fuel Temperature on Emission Characteristics and Engine Performance of Compression Ignition Engine." SAE Technical Paper 2002-32-1777.
- Kutz, M. (2006). Mechanical Engineers Handbook - Energy and Power (3rd Edition). New Jersey, John Wiley & Sons.
- Labeckas, G. and S. Slavinskas (2006). "The Effect of Rapeseed Oil Methyl Ester on Direct Injection Diesel Engine Performance and Exhaust Emissions." Energy Conversion and Management 47 (2006) 1954-1967.
- Ladommatos, N., S. M. Abdelhalim, H. Zhao and Z. Hu (1998). "Effects of EGR on Heat Release in Diesel Combustion." SAE Technical Paper 980184.
- Lapuerta, M., O. Armas and R. Ballesteros (2002). "Diesel Particulate Emissions from Biofuels Derived from Spanish Vegetable Oils." SAE Technical Paper 2002-01-1657.
- Lee, K.-H. (1998). "A Study on the Influence of Plastic Intake Manifold on the Performance and NVH of In-line 4 Cylinder Gasoline Engine." SAE Technical Paper 980728.
- Lejsek, D. and A. Kulzer (2009). "Investigations on the Transient Wall Heat Transfer at Start-Up for SI Engines with Gasoline Direct Injection." SAE Technical Paper 2009-01-0613.

- Li, Y., L. Li, J. Xu, X. Gong, S. Liu and S. Xu (2000). "Effects of Combination and Orientation of Intake Ports on Swirl Motion in Four-Valve DI Diesel Engines." SAE Technical Paper 2000-01-1823.
- Lilly, L. C. R. (1984). Diesel Engine Reference Book. London, Butterworths.
- Ling, J. and L. T. Y. Tun (2006). "CFD Analysis of Non-Symmetrical Intake Manifold for Formula SAE Car." SAE Technical Paper 2006-01-1976.
- Liu, I. (1999). Environmental Engineers Handbook. London, CRC Press.
- Mahallawy, F. E. and S. E. Habik (2002). Fundamental and Technology of Combustion. Oxford, Elsevier.
- Mahrous, A.-F. M. (2008). A CFD Study of Fluid Flow Characteristics in an Engine Cylinder with Negative Valve Overlapping. PhD Thesis, The University of Birmingham.
- Maiboom, A., X. Tauzia and J.-F. Hetet (2008). "Experimental study of various effects of exhaust gas recirculation (EGR) on combustion and emissions of an automotive direct injection diesel engine." Energy 33(1): 22.
- Maiboom, A., X. Tauzia, J.-F. Hétet, M. Cormerais, M. Tounsi, T. Jaine and S. Blanchin (2007). "Various Effects of EGR on Combustion and Emissions on an Automotive DI Diesel Engine: Numerical and Experimental Study." 2007-01-1834.
- Manente, V., A. Vressner, P. Tunestal and B. Johansson (2008). "Validation of a Self Tuning Gross Heat Release Algorithm." SAE Technical Paper 2008-01-1672.
- Martyr, A. J. and M. A. Plint (2007). Engine Testing. New York, Butterworth-Heinemann.

- Mathew, B. A. and H. Wiebeck (1999). "Automotive Air Intake Manifold Application using Nylon 6,6 Composite Material." SAE Technical Paper 1999-01-3011.
- Meng, X., J. Yang, X. Xu, L. Zhang, Q. Nie and M. Xian (2008). "Biodiesel production from oleaginous microorganisms." Renewable Energy.
- Montgomery, D. T. and R. D. Reitz (1996). "Six-mode Cycle Evaluation of the Effect of EGR and Multiple Injections on Particulate and NOx Emissions from a D.I. Diesel Engine." SAE Technical Paper 960316.
- Montgomery, D. T. and R. D. Reitz (1996). "Six-Mode Cycle Evaluation of the Effect of EGR and Multiple Injections on Particulate and NOx Emissions from a D.I. Diesel Engine." SAE Technical Paper 960316.
- Motortorque (2008). Land Rover Freelander 2 Automatic Review.  
<http://motortorque.askaprice.com/images/news/inhouse/4539%5B1%5D-03.jpg>. Retrieved on 29/09/08.
- Musculus, M. P. B. (2004). "On the Correlation between NOx Emissions and the Diesel Premixed Burn." SAE Technical Paper 2004-01-1401.
- Nwafor, O. M. I. (2003). "The Effect of Elevated Fuel Inlet Temperature on Performance of Diesel Engine Running on Neat Vegetable Oil at Constant Speed Conditions." Renewable Energy 28 (2003) 171-181.
- Nwafor, O. M. I. (2004). "Emission Characteristics of Diesel Engine Operating on Rapeseed Methyl Ester." Renewable Energy 29 (2004) 119-129.
- Nwafor, O. M. I. (2004). "Emission Characteristics of Diesel Engine Running on Vegetable Oil with Elevated Fuel Inlet Temperature." Biomass and Bioenergy 27 (2004) 507 - 511.

- O'Connor, J. F. and N. R. McKinley (1998). "CFD Simulations of Intake Port Flow Using Automatic Mesh Generation: Comparison With Laser Sheet, Swirl and LDA Measurements for Steady Flow Conditions." SAE Technical Paper 980129.
- Paffrath, H., M. Alex and K.-E. Hummel (1999). "Technology for Future Air Intake Systems." SAE Technical Paper 1999-01-0266.
- Patterson, M. S., S. C. Kong, G. J. Hampson and R. D. Reitz (1994). "Modelling the Effect of Fuel Injection Characteristics on Diesel Engine Soot and NOx Emissions." SAE Technical Paper 940523.
- Pierburg, A. (2008). Intake Manifolds- Smart System with Low Weight and Multiple Functions, Kolbenschmidt Pierburg Group.
- Pierpont, D. A., D. T. Montgomery and R. D. Reitz (1995). "Reducing Particulate and NOx Using Multiple Injections and EGR in a D.I. Diesel." SAE Technical Paper 950217.
- Quintero, H. F., C. A. Romero and L. V. V. Useche (2007). "Thermodynamic and dynamic analysis of an internal combustion engine with a noncircular-gear based modified crank-slider mechanism." 12th IFToMM World Congress, Besançon (France).
- Radavich, P. M., A. Selamet and J. M. Novak (2001). "Flow-Acoustic Coupling in Quarter-Wave Resonators Using Computational Fluid Dynamics." SAE Technical Paper 2001-01-1430.
- Rakopoulos, C. D., K. A. Antonopoulos, D. C. Rakopoulos, D. T. Hountalas and E. G. Giakoumis (2006). "Comparative Performance and Emissions Study of a Direct Injection Diesel Engine Using Blends of Diesel Fuel with Vegetable

- Oils or Bio-diesels of Various Origins." Energy Conversion and Management 47 (2006) 3272-3287.
- Ricardo (2006). "Ricardo WAVE Knowledge Center 7.2."
- Ricardo (2009). Ricardo WAVE Knowledge Center 7.2.
- Safari, M., M. Ghamari and A. Nasiritosi (2003). "Intake Manifold Optimization by Using 3-D CFD Analysis." SAE Technical Paper 2003-32-0073.
- Senatore, A., M. Cardone, V. Rocco and M. V. Prati (2000). "A Comparative Analysis of Combustion Process in D.I. Diesel Engine Fueled with Biodiesel and Diesel Fuel." SAE Technical Journal 2000-01-0691.
- Siavoshani, S., M. Stickler, H. Nehme and B. Krajewski (2001). "Analytical and Experimental Techniques in Solving the Plastic Intake Manifold NVH." SAE Technical Paper 2001-01-1544.
- Siqueira, C. d. L. R., M. P. Kessler, L. A. R. d. Araújo and E. C. Rodrigues (2006). "Three-dimensional Transient Simulation of an Intake Manifold using CFD Techniques." SAE Technical Paper 2006-01-2633.
- Smith, L. A., T. Fickenscher and R. P. Osborne (1999). "Engine Breathing - Steady Speed Volumetric Efficiency and Its Validity Under Transient Engine Operation." SAE Technical Paper 1999-01-0212.
- Smith, P. H. (1971). The Scientific Design of Exhaust and Intake Systems. Oxford, G T Foulis & Co Ltd.
- Song, J.-E., S.-H. Yoon and S. M. Baek (2005). "A Study on the NVH Characteristic for the Improvement of Plastic Intake Manifold." SAE Technical Paper 2005-03-0166.

- Stenlås, O., A. Gogan, R. Egnell, B. Sundén and F. Mauss (2002). "The Influence of Nitric Oxide on the Occurrence of Autoignition in the End Gas of Spark Ignition Engines." 2002-01-2699.
- Stiech, G. (2003). Modeling Engine Spray and Combustion Processes, Springer.
- Superflow (2008). SF1020-SB Super Bench- Automated and Control External Devices. [http://www.superflow.com/flowbenches/index\\_1157.cfm](http://www.superflow.com/flowbenches/index_1157.cfm). Retrieved on 21/11/08.
- Szybist, J. P. and A. L. Boehman (2003). "Behavior of a Diesel Injection System with Biodiesel Fuel." SAE Technical Paper 2003-01-1039.
- Szybist, J. P., J. Song, M. Alam and A. L. Boehman (2007). "Biodiesel Combustion, Emissions and Emission Control." Fuel Processing Technology 88 (2007) 679–691.
- Tanaka, H. and S. Kitagawa (2007). "Development of a Plastic Intake Manifold with CAE." SAE Technical Paper 2007-01-3549.
- Tat, M. E. (2003). Investigation of oxides of nitrogen emissions from biodiesel-fueled engines, Iowa State University. PhD thesis.
- Tompkins, B. T., J. Esquivel and T. J. Jacobs (2009). "Performance Parameter Analysis of a Biodiesel-Fuelled Medium Duty Diesel Engine." SAE Technical Paper 2009-01-0481.
- Transport, D.-G. f. E. a. (2004). "European Commission. Promoting Biofuels in Europe -Securing a Cleaner Future for Transport." Directorate-General for Energy and Transport.
- Tsolakis, A., A. Megaritis, M. L. Wyszynski and K. Theinnoi (2007). "Engine Performance and Emissions of a Diesel Engine Operating on Diesel-RME

- (Rapeseed Methyl Ester) Blends with EGR (Exhaust Gas Recirculation)."  
Energy 32 (2007) 2072-2080.
- Tsubokura, M., T. Kobayashi, T. Nakashima, T. Nouzawa and T. Nakamura (2008).  
"Computational visualization of unsteady flow around vehicles using high  
performance computing." Journal Computers and Fluids.
- Venugopalan, S., M.-C. Lai, F. Wu, W. S. University and F. M. Washko (2005).  
"Experimental and Simulation Analysis of PFI-SI Engine for Fuel Economy  
Improvement." SAE Technical Paper 2005-01-3691.
- Versteeg, H. K. and W. Malalasekera (1995). An Introduction to Computational Fluid  
Dynamics. London, Longman.
- Watson, N., A. D. Pilley and M. Marzouk (1980). "A Combustion Correlation for  
Diesel Engine Simulation." SAE Technical Paper 800029.
- Wendt, J. F. (1992). Computational Fluid Dynamics. Berlin, Springer Verlag.
- Wilcox, D. C. (1994). Turbulence Modeling for CFD. California, DCW Industries,  
Inc.
- Williams, F. A. (1985). Combustion Theory. California, The Benjamin/Cummings  
Publishing Company, Inc.
- Winterbone, D. E. and R. J. Pearson (1999). Design Techniques for Engine  
Manifolds". London, Professional Engineering Publishing.
- Woschni, G. (1967). "Universally Applicable Equation for the Instantaneous Heat  
Transfer Coefficient in the Internal Combustion Engine." SAE Technical  
Paper 670931.
- Xu, H. (2001). "Some Critical Issues on the Steady Flow Testing of Cylinder Heads."  
SAE Technical Papers 2001-01-1308.

- Yang, B., A. M. Mellor and S. K. Chen (2002). "Multiple Injections with EGR Effects on NO<sub>x</sub> Emissions for DI Diesel Engines Analyzed Using an Engineering Model." SAE Technical Paper 2002-01-2774.
- Yoon, S. H., H. K. Suh and C. S. Lee (2009). "Effect of Spray and EGR Rate on the Combustion and Emission Characteristics of Biodiesel Fuel in a Compression Ignition Engine." Energy & Fuels  
Vol 23(3): 1486-1493.
- Zheng, M., M. C. Mulenga, G. T. Reader, M. Wang, D. S. K. Ting and J. Tjong (2008). "Biodiesel Engine Performance and Emissions in Low Temperature Combustion." Fuel 87(6): 714.
- Zheng, M., G. T. Reader and J. G. Hawley (2004). "Diesel Engine Exhaust Gas Recirculation--a Review on Advanced and Novel Concepts." Energy Conversion and Management 45 (2004) 883-900.
- Zhu, H. and Z. Yang (2008). "Simulation of Flow around a Generic Pickup Truck with RSM Model." SAE Technical Paper 2008-01-0324.

**APPENDIX A**

**COMMERCIAL STEADY FLOW BENCH**

**SPECIFICATION**

A.1 Steady flow bench by Superflow Ltd. ([www.superflow.com](http://www.superflow.com))

<b>Details</b>	<b>Specification</b>
Model	SF1020
Flow rate range	0-1000 cfm (0-1699 m <sup>3</sup> /h)
Flow rate accuracy	± 0.5%
Pressure range	0-65 IWG (0-1.519 Pa)
Pressure accuracy	± 0.05 IWG
Weight	218 kg
Dimension	122 x 84 x 110 cm
Power requirement	240 VAC, 75A, Single phase, 50/60Hz

A.2 Steady flow bench by Cussons Ltd ([www.cussons.co.uk](http://www.cussons.co.uk))

<b>Details</b>	<b>Specification</b>
Model	P7305/SP
Flow rate range	0-423 cfm (0-720 m <sup>3</sup> /h)
Pressure range	0-61 IWG (0-165 CWG)
Weight	315 kg
Dimension	123 x 113 x 970 cm
Power requirement	240 VAC

## **APPENDIX B**

### **SPECIFICATION OF TEMPERATURE CONTROLLER**

#### B.1 Specification of Pixsys Temperature controller

---

SIZE: 48x96(frontal) x135 mm

POWER SUPPLY: 12/24Vac (internal switch), 115/230Vac (internal switch)

POWER CONSUMPTION: 4W

DISPLAY: Dual, 4 green Digits, 8 red leds

OPERATING CONDITIONS: 0-45 °C , 39...95rH%

INPUTS: 1 selectable for TC K, J, S, R, PT100, NI100, 0...10V, 0/4..20mA

DIGITAL INPUT: 1

OUTPUTS: 3 relays 8A-resistive + SSR 12v-50mA

CONTROL MODE:ON/OFF or PID-Autotuning

---

## APPENDIX C

### SPECIFICATION OF EXHAUST GAS ANALYSER

C.1 Specification of the AVL DiGAS 440 analyser (S. Chuepeng, 2008)

<b>Gas</b>	<b>Measuring range</b>	<b>Resolution</b>	<b>Accuracy</b>
CO	0-10% vol	0.01% vol	$\pm 0.03\%$ vol. (<0.6% vol.)
CO <sub>2</sub>	0...20% vol.	0.1% vol.	$\pm 0.5\%$ vol. (<10% vol.)
HC	0...20000ppm vol.	1ppm vol. ( $\leq 2000$ )	$\pm 10$ ppm vol. (<200ppm vol.)
O <sub>2</sub>	0...22% vol.	0.01% vol.	$\pm 0.1\%$ vol. (<2% vol.)
NO	0...5000ppm vol.	1ppm vol.	$\pm 50$ ppm vol. (<500ppm vol.)

C.2 Specification of the AVL CEB 200 analyser (S. Chuepeng, 2008)

<b>Gas</b>	<b>Measuring range</b>	<b>Resolution</b>
CO	0-1200ppm vol	1ppm vol.
CO <sub>2</sub>	0...15% vol.	0.1% vol.
HC	0...1950ppm vol.	1ppm vol.
O <sub>2</sub>	0...25% vol.	0.01% vol.
NOx	0...2500ppm vol.	1ppm vol.

## APPENDIX D

### SPECIFICATION OF PRESSURE TRANSDUCER

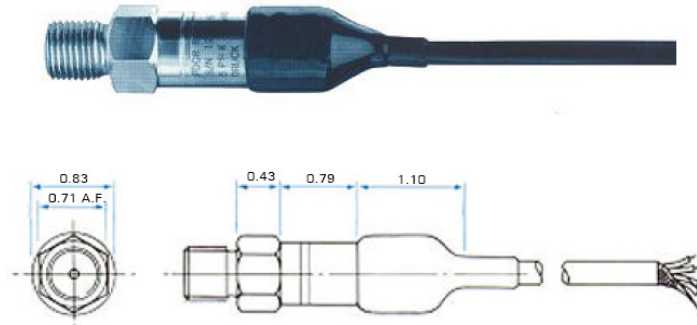


Figure E.1 Photograph and dimensions of pressure transducer (Series PDCR 800)

Table E.2 Specifications of pressure transducer

Transduction principle	Integrated silicon strain gauge bridge
Excitation voltage	10 Volts @ 5mA nominal
Pressure range	0 – 900 psi gauge
Accuracy	±0.1% BSL for ranges to 900 psi
Thermal stability	±1.5% tor band -5°F to +175°F
Burst pressure	In excess of 10x rated pressure
Operating temperature	-20°C to +80°C
Natural frequency	28 kHz for 5 psi increasing to 360 kHz for 500 psi
Weight	3.5 oz nominal

# APPENDIX E

## PERFORMANCE CURVE FOR TURBINE

J.1 Vane height: 4.1 (Fully open)

